D'Hondt, S.L., Jørgensen, B.B., Miller, D.J., et al., 2003
Proceedings of the Ocean Drilling Program, Initial Reports Volume 201

6. SITE 1225[1]

Shipboard Scientific Party[2]

BACKGROUND AND OBJECTIVES

Site 1225 was selected as a drilling target because its microbial activities and cell counts were expected to be far below those in ocean-margin settings but above those in the lowest activity open-ocean environments.

The principal objectives at Site 1225 were

1. To test by comparison with other sites drilled during this expedition whether microbial communities, activity, and survival strategies are different in this deeply buried, organic-poor environment than those in open-ocean sediments with more organic matter or shallower burial and
2. To examine how hydrologic flow in the underlying basement affects microbial communities, microbial activities, and microbial influence on environmental properties in organic-poor sediments with sulfate-rich interstitial waters.

Site 1225 is located in the eastern equatorial Pacific near the present-day boundary between the South Equatorial Current and the North Equatorial Countercurrent at 3760 m water depth. It lies in the sedimentary bulge created by the rain of biogenic debris from the relatively high productivity equatorial ocean. Geochemical studies of Deep Sea Drilling Project and Ocean Drilling Program (ODP) sites throughout this region have shown that seawater flows through the basaltic basement that underlies the sediments throughout this region (Baker et al., 1991; Oyun et al., 1995). Anomalously low conductive heat flow occurs throughout the region (Von Herzen and Uyeda, 1963; Sclater et al., 1976), possibly because the large-scale flow of relatively cool seawater through the basalts depresses conductive heat flow (Oyun et al., 1995).

[1]Examples of how to reference the whole or part of this volume.
[2]Shipboard Scientific Party addresses.

Ms 201IR-106

The lithologies, sediment age, and many geophysical characteristics of the target site were well characterized by earlier studies of nearby Site 851 (Mayer, Pisias, Janecek, et al., 1992; Pisias, Mayer, Janecek, Palmer-Julson, and van Andel, 1995). Those studies indicated that the site is representative of a large portion of the eastern equatorial Pacific region. The sediments of Site 851 have a continuous biostratigraphy with a minimal age of 11 Ma at the basaltic basement. The gross lithologic and physical properties of the carbonate and siliceous oozes and chalk at Site 851 are characteristic of sediments throughout the region (Mayer, Pisias, Janecek, et al., 1992). The interstitial water chemical profiles at Site 851 exhibit clear evidence of seawater flow through the underlying basalts (and perhaps the lower part of the sediment column) (Oyun et al., 1995; Spivack and You, 1997).

Cragg and Kemp (1995) documented the presence of prokaryotic cells and activity throughout the sediment column at Site 851. For the first few tens of meters below seafloor, counts of both total cells and dividing cells were low relative to counts from similar depths at sites from the Peru shelf and the Japan Sea (Cragg and Kemp, 1995). At greater depths, Site 851 cell counts approached the averaged values from all previously counted sites.

Leg 138 shipboard chemistry showed that concentrations of several dissolved chemical species (ammonium, strontium, and silica) and alkalinity peaked midway down the sediment column. In contrast, dissolved sulfate exhibited maximum values near the sediment/water interface and the basement/sediment interface (Mayer, Pisias, Janecek, et al., 1992). These patterns of sedimentary interstitial water concentration are inferred to result from low levels of biological activity throughout the sediment column, coupled with diffusive exchange with the overlying ocean and with water flowing through the underlying basalts (Spivack and You, 1997). Geochemical modeling suggests that net microbial sulfate reduction in the upper half of the Site 851 sediment column corresponds to a respiration rate of 10^{-9} to 10^{-8} mol $CO_2/cm^2/yr$ (D'Hondt et al., 2002). This rate of respiration is only the barest fraction of the rate of carbon dioxide reduction by photosynthesis in the overlying equatorial ocean (10^{-3} mol/cm^2/yr) (D'Hondt et al., 2002). The subsurface distribution of electron acceptors with higher standard free-energy yields (oxygen, nitrate, oxidized manganese, and oxidized iron) in this region was not determined for Site 851.

PRINCIPAL RESULTS

At Site 1225, concentrations of methane, ammonium, dissolved inorganic carbon (DIC), and alkalinity peak in the middle of the sediment column and decline toward both the sediment/ocean interface and the sediment/basement interface. In contrast, sulfate concentration is lowest in the middle and lower part of the sediment column and nitrate and dissolved oxygen are present only at the ocean and basement interfaces. These profiles result from the balance between net subsurface microbial activities and small net fluxes of biologically utilized chemicals across the ocean/sediment and sediment/basement interfaces.

Interstitial water data also document dissolved oxygen penetration into the top 2 m of the sediment column, an interval containing nitrate in the top 1.5 m of the sediment, a peak concentration of dissolved manganese at 3.6 meters below seafloor (mbsf), a broad zone of relatively high dissolved iron centered at ~25 mbsf, and sinks for reduced

manganese and dissolved iron at 100 mbsf. Sulfate concentrations decrease downhole by only ~7% from local bottom-water values; most of this decrease occurs in the upper ~60 m. This vertically extended sequence of successive interstitial water chemical zones closely resembles the centimeter- to decimeter-scale sequence seen in nearshore sediments (with depth-dependent transitions from a zone of oxygen reduction to successive zones of nitrate, manganese oxide, iron oxide, and sulfate reduction). These data are consistent with the hypothesis that subseafloor microbial communities preferentially utilize the available electron acceptor that yields the highest free energy of reaction.

In the lower portion of the sediment column, this vertical sequence of successive reduction zones is reversed as a result of water flow through the underlying basaltic basement. Diffusion of solutes from this basement water to the overlying sediment delivers nitrate to the lowermost 20 m of the sediment column (300 mbsf to basement) and possibly also dissolved oxygen to the lowermost meter of the column (319.3 mbsf to basement). This short interval of dissolved oxygen and nitrate is overlain by a broad zone of dissolved manganese centered near 250 mbsf and a broad peak of dissolved iron centered at ~230 mbsf. These dissolved nitrate and oxygen profiles show that electron acceptors yielding high free energies of reaction are introduced to at least some portions of the deep subseafloor biosphere by hydrologic processes. They also indicate that microbial activity in the underlying basalt is insufficient to strip even the scarcest preferentially utilized electron acceptors from the seawater that flows through the basalt at this site.

Dissolved hydrogen concentrations in incubations of Site 1225 sediments are generally in the range of 1–2 nM. Lovley and Goodwin (1988) and Hoehler et al. (2001) observed similar concentrations in experiments with near-surface aquatic sediments, where sulfate reduction is the primary electron-accepting reaction. On the basis of their observations, Lovley and Goodwin (1988) hypothesized that hydrogen concentration in aquatic environments is controlled by competition between different metabolic pathways. According to this hypothesis, prokaryotes using electron acceptors that yield higher free energies of reaction are able to operate at lower electron donor concentrations and thereby out-compete prokaryotes limited to electron acceptors that yield lower free energies of reaction. Documentation of these concentrations at Site 1225 suggests that even in low-activity subseafloor sediments, hydrogen concentrations may be controlled by the same thermodynamic competition between electron-accepting pathways as in high-activity sediments and can be predicted from the dominant pathway.

Methane is present at trace concentrations of <0.25 µM throughout the sediment column. This finding demonstrates the presence of methane in subseafloor sediments with sulfate concentrations that are very close to seawater values. The generation of methane in these sediments challenges models of microbial competition that are based on standard free energies. There are a number of possible reasons for the occurrence of methanogenesis in sulfate-rich sediments. For example, the methanogens and sulfate reducers may rely on different electron donors (e.g., the methanogens may utilize methylated amines and the sulfate reducers may rely on hydrogen and/or acetate) (Oremland and Polcin, 1982; Oremland et al., 1982; King, 1984).

The steady-state maintenance of methane in the subseafloor sediments of Site 1225 indicates that if anaerobic methanotrophy occurs here, it does not drive methane concentrations below a few hundredths

to tenths of micromolar. Concentrations are lowest near the sediment/ocean and sediment/basement interfaces, where methane may be oxidized by prokaryotes using electron acceptors that yield relatively high energies of reaction (such as nitrate or dissolved oxygen). The highest methane concentration is present in the middle of the sediment column, where sulfate appears to be the principal terminal electron acceptor available. We hypothesize that the peak methane concentration is held at the observed level (~0.15–0.25 µM) because sulfate-reducing methanotrophs cannot oxidize methane at lower concentrations under in situ conditions.

Concentrations of acetate and formate were <1 and <0.5 µM, respectively, throughout the sediment column. These concentrations are an order of magnitude lower than those measured in continental shelf sediments (Sørensen et al., 1981; Wellsbury and Parkes, 1995) and are also lower than those in other deep sediment sites (Wellsbury et al., in press). These very low concentrations may be regulated by limiting energy yields or limited by the kinetics of active uptake by the anaerobic respiring prokaryotes. Since these results are among the first to demonstrate very low concentrations of short-chain fatty acids in cold, low-activity subsurface sediments, there is no database for comparison.

Comparison of Site 1225 physical property, sedimentology, and chemical records suggests that broad-scale patterns of past oceanographic change exert strong influence on present subseafloor metabolic activity. Concentrations of dissolved iron closely follow downhole variations in magnetic susceptibility and split-core reflectance, with peak concentrations of dissolved iron and solid-phase iron compounds (inferred from magnetic susceptibility) in the intervals from ~0 to 70 and 200 to 270 mbsf. The intact magnetic reversal record suggests that the magnetic phases were created during or shortly after sediment deposition. These intervening sediments are low in dissolved iron, are low in magnetic susceptibility, are characterized by the most intensely bioturbated intervals, and were deposited during a late Miocene–early Pliocene "biogenic bloom" that occurred throughout much of the global ocean (van Andel et al., 1975; Farrell et al., 1995; Dickens and Owen, 1999).

Four Adara tool deployments plus two deployments of the Davis-Villinger Temperature Probe (DVTP) defined a sediment/water interface temperature of 1.4°C and an estimated sediment/basement interface temperature of 7.0°C. The downhole temperature gradient curved slightly downward. The slight curvature appears to be best explained by a geologically recent decrease in basement temperature, perhaps a result of an increased rate of seawater flow through the basement. Throughout the sediment column, in situ temperatures were well within the range inhabited by psychrophilic prokaryotes.

Experiments on major microbial processes and experiments for enumeration of viable prokaryotes were initiated at selected depths ranging from near the mudline to near the basement, where samples were obtained within centimeters of the basalt. Subsamples for postcruise biomolecular assays and microbiological experiments were routinely taken from all of the distinct geochemical zones and lithologic subunits. Total cell numbers were enumerated on board. These cell counts are very close to data obtained from nearby Site 851 and consequently demonstrate the high reproducibility of acridine orange direct counts (AODCs) in subseafloor microbial studies.

At this site, novel experiments with core temperatures and contamination tracers were undertaken to determine how handling of cores and

samples for microbiological studies might be improved. Catwalk experiments with an infrared (IR) camera were used to assess the effects of different core handling procedures on transient warming of the core and, consequently, on the survival of temperature-sensitive prokaryotes.

OPERATIONS

Leg 201 began at 0830 hr on 27 January 2002, when the first line was passed ashore at Berth 4 of the 10th Avenue Terminal in San Diego, California. Routine port call activities were accompanied by the loading of several boxes of equipment and supplies dedicated to the microbiological and geochemical objectives of Leg 201. In addition, the new radioisotope facility was brought on board (see **"Rate and Biogeochemical Process Measurements"** p. 38, in "Procedures and Protocols" in "Microbiology" in the "Explanatory Notes" chapter). Site 1225 coring operations are described in Table **T1.**

T1. Coring summary, Site 1225, p. 74.

Transit to Site 1225

After completing port call activities, the last line was cast off at 0800 hr on 1 February. The pilot and three harbor marshals were discharged at 0910 hr just off Point Loma, and the vessel assumed full speed for the voyage to the first site of Leg 201. Because of excellent weather and a favorable current, the 1835-nmi voyage to Site 1225 was accomplished in just 6.6 days at an average speed of 11.7 kt. This led to arrival on site nearly a full day earlier than scheduled.

Site 1225

The vessel arrived on the Global Positioning System coordinates for Site 1225 on 7 February at 2115 hr, and we commenced lowering thrusters and hydrophones. After switching into dynamic positioning mode, a positioning beacon was deployed at 2242 hr.

Hole 1225A

The bottom-hole assembly for Site 1225 consisted of a new Rock Bit Industries 11 7/16-in C-3 extended core barrel (XCB) bit, five 8¼-in drill collars plus the nonmagnetic collar used with the Tensor tool core orientation system, and the seal bore drill collar used with the advanced hydraulic piston corer (APC), XCB, and pressure coring system (PCS).

While tripping the pipe, a precision depth recorder reading was taken using the 3.5-kHz recorder. The site-corrected reading of 3755 m was adjusted for the distance to the rig floor dual elevator stool to 3773.4 meters below rig floor (mbrf). The APC core barrel was deployed on the aft wireline, and the bit was positioned at 3767.0 mbrf. Bottom-water temperature was measured with the APC temperature tool (Adara tool). We initiated Hole 1225A at 0840 hr on 8 February. Upon recovery, Core 1H contained 4.30 m of core, establishing a drill pipe–measured seafloor depth of 3772.2 mbrf. All cores recovered from Hole 1225A were extracted from the drill pipe and transferred as expeditiously as possible to the catwalk to minimize core warming (see **"Core Handling and Sampling,"** p. 15, in "Introduction and Background" in "Microbiology" in the "Explanatory Notes" chapter).

APC coring continued without incident through Core 19H to a depth of 175.3 mbsf. Core 20H gave a positive full stroke indication; however, because of a 70-kilopound (klb) overpull, the barrel had to be freed by drilling down and over the end of the APC shoe (drill over). Cores 21H and 22H continued with a normal full-stroke pressure bleed off and required only 30 klb of overpull for extraction from the formation.

Tensor core orientation was initiated with Core 4H and continued through Core 33H. Adara temperature measurements were recorded before recovery of Cores 5H (42.3 mbsf), 7H (61.3 mbsf), 9H (80.3 mbsf), and 14H (127.8 mbsf). All measurements were successful except the one from 42.3 mbsf. Failure of this run was attributed to a tool software fault. The APC-Methane (APC-M) tool was installed in the coring system prior to Core 5H and was run on each core barrel through Core 14H. The tool worked well initially but stopped collecting data after Core 8H. This failure was thought to be the result of a power interruption that caused the tool to stop logging data.

After Core 22H (203.8 mbsf), we ran the first of three deployments of the DVTP. After recovering the DVTP, we drilled without coring through the disturbed interval (nominally 1.5 m) to a depth of 205.3 mbsf. We followed the successful temperature probe wireline run with deployment of the new Davis-Villinger Temperature-Pressure Probe (DVTP-P). The first deployment with this tool was unsuccessful, apparently as a result of a clogged filter.

APC coring continued through Core 27H to a depth of 243.3 mbsf. All coring runs except 27H achieved full stroke of the piston. Each extraction attempt from Core 23H through 27H required >80 klb overpull, so in each case we employed the drill-over technique to facilitate core barrel recovery. Although the driller indicated we did not achieve a full stroke on Core 27H, we opted to drill ahead to a full-stroke length to keep our sampling strategy consistent. A second DVTP wireline run after Core 27H suffered an electronic failure, due to a broken thermistor bulkhead, and did not record a temperature.

Because of the incomplete stroke on Core 27H, we switched to the XCB coring system. Core 28X returned empty. Core 29P was cut using the newly modified PCS. This tool was being tested for possible use on the Peru margin sites of Leg 201 and also for Leg 204. Core 29P advanced a total of 2.0 m. Upon recovery, the pressurized chamber was 100% full; the tool recovered 1.0 m of core under 1200 psi pressure. Another 41 cm of unpressurized core was recovered in the bit extender below the ball valve.

In deference to the poor recovery with the XCB and in light of the soft sediment recovered in the bottom of the PCS core barrel, we opted to attempt to deepen the hole with the hydraulic piston core system. Cores 30H through 33H all required drill over after 80 klb overpull failed to release the barrels from the formation. In addition, Core 30H indicated only partial stroke but returned full recovery. After Core 33H, we ran a second deployment of the DVTP-P. The pressure measurement again failed, and a postdeployment inspection located an internal leak in the pressure transducer line. After drilling down 1.5 m to remove the sediment disturbed by the pressure probe, this was followed by a third DVTP temperature measurement, which was successful.

With basaltic basement projected at a depth of ~318 mbsf, a final APC core (Core 34H) was recovered after drilling over the shoe because of excessive overpull. Subsequently, we deployed an XCB core barrel hoping to obtain ~1.0 m of basement rock. After contacting basement at ~318.6 mbsf, the driller advanced another 1.0 m in 15 min. Basement

was readily identifiable because of an abrupt increase in drilling torque and a significantly reduced rate of penetration. Upon recovery, the XCB core barrel contained 7.25 m of sediment, with two cobbles of basalt embedded in sediment packed in the core catcher. Rather than deploy another barrel (since we had already drilled >1 m into basement without recovering the sediment/basalt interface), we chose to conclude coring operations for this hole at 1930 hr on 10 February.

A wiper trip to 80 mbsf followed, sweeping the hole with a 20-bbl sepiolite mud pill. We displaced the hole with 130 bbl of sepiolite in preparation for logging and encountered only 2 m of fill in the bottom of the hole. A single wireline run with the triple combination (triple combo) tool string was completed by 1045 hr on 11 February, and the bit cleared the seafloor at 1110 hr on 11 February, ending Hole 1225A.

In support of the microbiological contamination testing protocol, Whirl-Pak bags containing full-concentration fluorescent microspheres (see **"Fluorescent Microparticle Tracer"** p. 27, in "Procedures and Protocols" in "Microbiology" in the "Explanatory Notes" chapter) were deployed with Cores 2H, 12H, 17H, 22H, and, possibly, 34H. In addition, perfluorocarbon tracer (PFT) was pumped continuously during coring operations. The rate and quantity of tracer was automatically controlled using an input signal from the Tru-Vu rig instrumentation system (see **House et al.,** this volume).

Hole 1225B

We offset 10 m north of Hole 1225A and spudded Hole 1225B at 1240 hr on 11 February. Subsequent recovery of APC Core 1H was 8.96 m, establishing a seafloor depth of 3771.0 mbrf. Hole 1225B consisted of a single APC core to provide samples for high-resolution physical property measurements. Hole 1225B ended with the recovery of Core 1H at 1315 hr on 11 February.

Hole 1225C

After offsetting another 10 m north, Hole 1225C was spudded at 1355 hr on 11 February. Recovery of Core 1H was 8.83 m, establishing a seafloor depth of 3771.2 mbrf.

APC coring continued without incident through Core 15H (141.8 mbsf). Core 16H required 10 min to drill over after 80 klb of overpull failed to extract the barrel from the formation. Coring continued using the drill-over technique with all barrels stroking fully through Core 25H. Drill-over time ranged from 20 to 30 min.

APC coring resumed with Core 26H and continued through Core 31H (293.8 mbsf). Cores 26H, 27H, 29H, and 30H indicated partial stroke but returned full recovery. Cores 28H and 31H were recovered after indicating that a full stroke had been achieved. Tensor core orientation was initiated with Core 3H and continued through Core 31H.

Core 32P was cut using the PCS and an auger-style bit. As with the first test conducted in Hole 1225A, coring advanced a total of 2.0 m (to a depth of 295.8 mbsf), even though the pressure core chamber was only designed to hold 1.0 m of core. Upon recovery, the pressurized chamber was once again 100% full. This time the tool recovered 1.0 m of core under 4800 psi pressure. There was no core recovered in the bit extender below the ball valve on this deployment.

After completing the second PCS test, Core 33H indicated a full stroke, but our attempts to drill over the bit were thwarted by a bent

core barrel. This resulted in a pipe trip, terminating Hole 1225C at a total depth of 305.3 mbsf, 13.3 m short of the basement objective. Microspheres were deployed with Core 1H, and PFT was pumped continuously during coring operations. By 1930 hr on 13 February, all thrusters and hydrophones had been raised and the ship was secured for transit. Weather and sea state during the occupation of Site 1225 ranged from good to excellent. We experienced no operational difficulties that could be attributed to the environment.

LITHOSTRATIGRAPHY

The sedimentary sequence at Site 1225 consists mainly of nannofossil ooze with varying amounts of diatoms, radiolarians, and foraminifers, except one interval that was dominated by diatom ooze. One lithostratigraphic unit was recognized in all holes at Site 1225 (Fig. F1). Site 1225 had previously been drilled during Leg 138 as Site 851 (Shipboard Scientific Party, 1992). The age framework presented in this chapter was obtained by using the timescale of Berggren et al. (1995a, 1995b) to update the age model of Site 851 (Shipboard Scientific Party, 1992). This age model was based on magnetostratigraphy and planktonic foraminifer biostratigraphy for the uppermost 90 m and on nannofossil, radiolarian, and diatom biostratigraphy for the rest of the section.

The lithologic description is based on the visual description of sediment color and sedimentary structures as well as on other parameters such as smear slide analyses and color reflectance. Calcium carbonate content, expressed as weight percent $CaCO_3$, and organic carbon analyses (see "Biogeochemistry," p. 14), X-ray diffractometry (XRD) (Fig. F2), and laboratory measurements of magnetic susceptibility (Fig. F3), density, and water content (see "Physical Properties," p. 23) were also used to characterize lithologic changes.

Description of Lithostratigraphic Units

Unit I

Interval: 201-1225A-1H-1, through 35X-CC; 201-1225B-1H-1 through 1H-CC; and 201-1225C-1H-1 through 33H-3
Depth: 0–319.6 mbsf (Hole 1225A), 0–9.0 mbsf (Hole 1225B), and 0–305.3 mbsf (Hole 1225C)
Age: Pleistocene to middle Miocene

The sediments at Site 1225 consist of middle Miocene to Pleistocene nannofossil ooze with varying amounts of both calcareous (foraminifers) and siliceous (diatoms, radiolarians, and sponge spicules) microfossils. These variations become apparent in the measurements of percentage of $CaCO_3$ (see "Biogeochemistry," p. 14) and color reflectance (Fig. F1). Calcium carbonate content is relatively high throughout the unit, ranging between 58 and 85 wt% (average = 74 wt%), except for a low value of 42 wt% $CaCO_3$ measured near the top of Subunit ID (see "Biogeochemistry," p. 14). Smear slide estimates of carbonate content are generally in good agreement with the pattern indicated by the $CaCO_3$ analyses.

F1. Lithostratigraphic summary, p. 38.

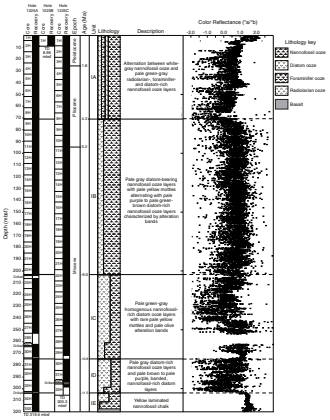

F2. Examples of XRD analyses, p. 39.

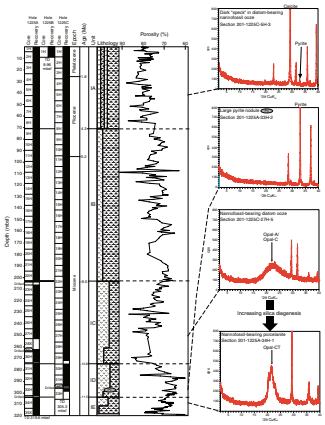

F3. Bioturbation and magnetic susceptibility, p. 40.

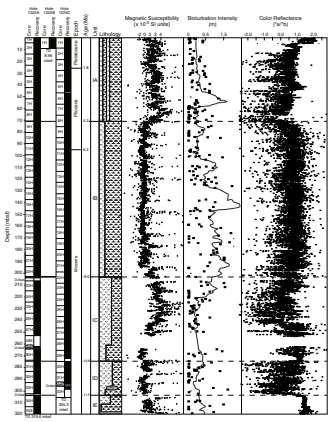

The sediments of Unit I are either massive or bioturbated and exhibit no other notable primary sedimentary structures. The color of sediments varies from gray and pale green to pale gray and white. Secondary alteration features such as centimeter-scale greenish, purple, and pale gray banding as well as dark layers and spherical concentrations of pyrite are common. Based on these variations in sediment composition, degree of bioturbation, color reflectance data, and changes in the degree of postdepositional alteration, five subunits were distinguished.

Subunit IA

Interval: 201-1225A-1H-1 through 8H-CC and 201-1225C-1H-1 through 8H-4, 110 cm
Depth: 0–70.8 mbsf (Hole 1225A) and 0–71.4 mbsf (Hole 1225C)

Subunit IA consists of foraminifer-, diatom-, and radiolarian-rich nannofossil ooze of Pleistocene to late Pliocene age. The first 2.5 m of the sedimentary section in all holes contains two ~50-cm-thick layers of brown to brownish gray sediment containing iron and manganese oxides. Below the redox boundary between 2.5 and 2.6 mbsf, the sediment is characterized by a rhythmic alternation between darker-colored, 40- to 50-cm-thick foraminifer-, radiolarian-, and diatom-rich intervals and 70- to 80-cm-thick lighter-colored intervals characterized by higher nannofossil contents. The darker intervals commonly show centimeter-scale, pale green and gray alteration bands, whereas the lighter-colored layers are dominated by yellowish gray mottled zones, which are most likely the result of more intensive bioturbation. The bases of the darker intervals are commonly sharp, and burrows in the underlying lighter sections are filled with darker material from above. Dark sulfide-rich spots and thin bands of dark gray material (presumably pyrite) are common (Fig. **F4F**). The sediments contain 50%–90% nannofossils, 5%–25% foraminifers, 5%–30% radiolarians, and 5%–30% diatoms. This lithologic variability is also reflected in the color reflectance and $CaCO_3$ data. The carbonate content of this subunit ranges from 64 to 85 wt% $CaCO_3$, with the lower values presumably corresponding to intervals richer in siliceous microfossils. Water content is generally high and highly variable (see **"Physical Properties,"** p. 23).

F4. Site 1225 features, p. 41.

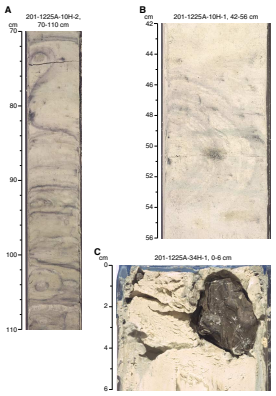

Subunit IB

Interval: 201-1225A-9H-1 through 22H-CC and 201-1225C-8H-4, 110 cm, through 22H-CC
Depth: 70.8–203.8 mbsf (Hole 1225A) and 71.4–208.3 mbsf (Hole 1225C)

Subunit IB consists of ~135 m of early Pliocene to late Miocene pale greenish gray to light gray diatom-bearing and diatom-rich nannofossil ooze (5%–20% diatoms) with minor amounts of radiolarians (>10%, decreasing toward the base of the subunit). In contrast to Subunit IA, foraminifers are present only in trace amounts. The sediments are characterized by a decimeter-scale interbedding of pale greenish gray to gray banded intervals with pale greenish gray mottled and bioturbated zones. Alteration bands usually show pale purple, greenish gray, and yellow colors (Fig. **F4A**). They are either oriented subparallel to the weakly developed depositional layering, are present as curvilinear features, or form ellipsoidal reaction fronts around burrows (Fig. **F4B**). The mottled zones are characterized by pale greenish gray nannofossil ooze with burrows filled with light yellowish gray sediment. Gray pyrite-rich spots, nod-

ules, and streaks are common throughout the interval (e.g., Fig. F4G). These sulfide-rich zones are often accompanied by pale purple-gray halos around dark gray spots and thin layers. Diagenetic banding and the presence of pyrite-rich layers and spots is much more predominant in Subunit IB than in the overlying and underlying sedimentary subunits. Bioturbation is generally strong in this subunit (Fig. F3). Color reflectance data, magnetic susceptibility, water content, and many other physical properties of the sediment are significantly different from the properties in the overlying Subunit IA (Fig. F1). In particular, the water content of the sediments in Subunit IB is much lower and appears to vary systematically with depth. Magnetic susceptibility values are low throughout the section (see Fig. F3; "Physical Properties," p. 23).

Subunit IC

Interval: 201-1225A-23H-1 through 30H-4 and 201-1225C-23H-1 through 29H-3, 110 cm
Depth: 203.8–270.1 mbsf (Hole 1225A) and 208.3–269.4 mbsf (Hole 1225C)

Subunit IC is a 60- to 65-m-thick section of pale greenish gray to gray diatom-bearing and diatom-rich nannofossil ooze (5%–40%) of Miocene age. Radiolarians are present in minor amounts (1%–10%). The main distinguishing feature of Subunit IC is the more homogeneous overall appearance of its sediments. Alteration bands and intensively bioturbated zones are far less common in the upper part of the subunit than in the lower part of the subunit. Pyrite-rich spots and pyritized burrows are common. Carbonate contents tend to be lower and show a higher degree of variability than in the other subunits (see "Biogeochemistry," p. 14). Color reflectance data are more variable than in Subunit IB, and magnetic susceptibility values are both higher and more variable compared to the 70- to 200-mbsf interval. Water content and porosity increase toward the base of Subunit IC (see "Physical Properties," p. 23). These increases might be related to the increase of biosilica (diatoms and radiolarians).

Subunit ID

Interval: 201-1225A-30H-5 through 33H-CC and 201-1225C-29H-3, 110 cm, through 33H-CC
Depth: 270.1–302.2 mbsf (Hole 1225A) and 269.4–305.3 mbsf (Hole 1225C)

The lower ~2.5 m of Cores 201-1225A-30H and 201-1225C-29H consist of dark olive-green nannofossil-rich laminated diatom ooze. This section defines the top of Subunit ID, a ~30-m-thick sedimentary section of late Miocene age. Below the diatom ooze are sediments dominated by nannofossils (80%–90%) with subordinate amounts of diatoms and radiolarians (generally <10%). With the exception of the homogeneously dark green diatom layer, the sediments appear similar to the nannofossil oozes of Subunit IB. Pale greenish gray to gray and purple alteration bands are common and alternate with pale greenish gray and pale yellow bioturbated intervals. High concentrations of pyrite are common as dark gray nodules (Fig. F4G) and pyritized burrows, as well as in dark gray bands and spots throughout the section. Magnetic susceptibility data show a sharp decrease to values comparable to the susceptibility pattern in Subunit IB (Fig. F3). The first 5 cm of Section 201-1225C-30H-1 (274.8 mbsf) contains several pieces of gray laminated porcelanite, in-

dicating the onset of silica diagenesis and the transformation of biogenic opal-A to more crystalline opal-CT in the lower part of Site 1225. This trend was confirmed by XRD analysis as well as by a sudden drop in porosity (Fig. F3).

Subunit IE

Interval: 201-1225A-34H-1 through 35X-CC
Depth: 302.2–319.6 mbsf

Subunit IE near the base of Hole 1225A represents sediments directly overlying the oceanic basement. This interval consists of pale yellow diatom-rich nannofossil ooze, which grades with depth into a laminated nannofossil chalk between Sections 201-1225A-35X-2 and 35X-3 (Fig. F4E). These semi-indurated sediments contain several darker diatom-rich layers. In Core 201-1225A-35X, brown volcanic glass is disseminated in the sediment as well as concentrated in thin layers (Fig. F4D). The top of Section 201-1225A-34H-1 (~300 mbsf) contains pieces of gray opal-CT porcelanite (Fig. F4C).

Color Reflectance Spectrophotometry

The combination of spectrophotometric analysis with visual observations and other lithostratigraphic methods greatly improved the stratigraphic and lithologic framework of Site 1225. In particular, the main inflection points of the a*/b* time series show a good match with the boundaries of the five lithostratigraphic subunits (Fig. F1), as well as with the relative variations of the main biogenic components observed in smear slide analysis. In general, higher values of the a*/b* ratio are present in the white to pale gray nannofossil ooze layers (e.g., Subunit IB), whereas the a*/b* ratio is lower where darker diatom-rich layers predominate (e.g., Subunit ID). Figure F3 also shows that the average variations of the a*/b* ratio and magnetic susceptibility are in opposition of phase and suggests that darker layers (less reflectance) are probably richer in magnetic oxides.

Mineralogy

XRD analyses were performed on 37 specimens from both Holes 1225A and 1225C. Overall, the mineralogic composition of Site 1225 samples reflects the dominant lithology, which is nannofossil ooze for most of the sedimentary section. The mineralogic assemblage is thus dominated by calcite, as also confirmed by calcium carbonate content (see "Biogeochemistry," p. 14). Even though the biogenic silica component (diatoms and radiolarians) is present in both Subunits IA and IB, silica minerals (Fig. F2) were detected only in the lower part of the section (Subunits IC and ID). In fact, the primary composition of diatom frustules and radiolarian tests is opal-A, an amorphous admixture of water and silica tetrahedrons undetectable by XRD. However, with increasing burial and temperature, opal-A tends to crystallize into crystobalite (opal-C) and trydimite, which together form the more stable opal-CT silica phase. As shown in Figure F2, such a silica phase change is detected by XRD analyses, which first show a progressive bulging between 15° and 28°2θ and then a sharpening of the crystobalite peak in deeper samples. At Site 1225, the opal-A to opal-CT phase change occurs between ~250 and 300 mbsf.

In general, the opal-A to opal-CT phase change has important consequences for the physical and chemical properties of the sediment. Whereas an increase of the opal-A component has a positive effect on sediment porosity, the onset of the opal-A to opal-CT phase change and the resultant silica reprecipitation causes a porosity reduction and a release of water, as shown in Figure F2, where silica diagenesis and porosity variations are compared.

As reported in "Unit I," p. 8, in "Description of Lithostratigraphic Units," millimeter-sized pyrite specks and streaks were observed in most of the subunits of Site 1225 (see the XRD results for Section 201-1225C-5H-3 in Fig. F2). However, larger pyrite nodules were observed only in the lowermost subunits (IC and ID) (Figs. F4F, F2: Section 201-1225A-33H-2).

Bioturbation

Most of the sediments recovered at Site 1225 show burrows and mottled structures of probable biogenic origin. The most common type of bioturbation is ellipsoidal to irregularly shaped mottles of varying sizes (between 1 and 5 cm), which can generally be attributed to either *Chondrites* or *Planolites*. The mottled structures of Subunit IB are often surrounded by purple or green alteration halos.

Bioturbation is concentrated in the central part of Subunit IB, where it usually occurs at the boundary between the alternating white and darker banded layers.

Based on visual description of the cores, the density of bioturbation was estimated. In Figure F3, the thickness of bioturbated layers is plotted vs. depth and compared to magnetic susceptibility. Overall, variations in density of bioturbation and variations in magnetic susceptibility (see "Physical Properties," p. 23) show a negative correlation. In particular, opposite variations are evident in Subunits IB, IC, and ID (Fig. F3). Thus, bioturbation may have been one of the factors that contributed to the degradation of magnetic minerals in the low magnetic susceptibility parts of the section. Alternatively, the density of bioturbating fauna may have been higher and the magnetic minerals may have been chemically reduced during early diagenesis, both due to a higher deposition rate of organic matter.

The variation in intensity of bioturbation reflects changes in the amount of biogenic activity that occurred at the water/sediment interface during or soon after deposition. Higher intensity of bioturbation may have resulted from either higher concentration of free oxygen in bottom waters or higher availability of food sources on the sea bottom (e.g., higher input of organic carbon). The latter hypothesis seems to be supported by the geochemical data presented in the Leg 138 *Initial Reports* volume for Site 851 (Shipboard Scientific Party, 1992, fig. 35, p. 941), which show that the highly bioturbated Subunit IB is characterized by relatively higher organic carbon accumulation rates (from 0.1% on top of Subunit IA to up to 0.4% in Subunit IB).

Thin Section

Light gray, pervasively altered basalt was recovered in the lowermost section of Core 201-1225A-35X. Most of this material was consumed by microbiological sampling, but a few small pieces were archived. During transport to the ODP repository, these pieces disaggregated and were unsuitable for thin section preparation or bulk geochemical analysis.

Summary

At Site 1225 a nearly complete Pleistocene to middle Miocene section of mainly pale gray nannofossil ooze with varying amounts of diatoms, radiolarians, and foraminifers was recovered. The maximum thickness of this section is 319.6 m. Site 1225 is within 100 m of Site 851, which was drilled during Leg 138 (Shipboard Scientific Party, 1992).

Because of the overall homogeneity of the observed lithologies, only one stratigraphic unit was recognized. However, minor changes in sedimentologic features, biogenic components, color, and other physical and mineralogic parameters allowed the subdivision of Unit I into five subunits.

Subunit IA (0–~71 mbsf) consists of a foraminifer-, diatom-, and radiolarian-rich nannofossil ooze of Pleistocene to Pliocene age characterized by rhythmic alternation of pale gray nannofossil-dominated layers and darker, often banded and/or bioturbated foraminifer-, radiolarian-, and diatom-rich nannofossil ooze layers.

Subunit IB (~71–205 mbsf) is an early Pliocene to late Miocene age pale greenish gray to light gray radiolarian- and diatom-bearing and diatom-rich nannofossil ooze section. Decimeter-scale interbedding of pale greenish gray to gray banded intervals with pale greenish gray mottled and bioturbated zones is common, as well as pale purple alteration bands that are present either in subhorizontal layers or as curvilinear features.

Subunit IC (~205–270 mbsf) is a pale greenish gray diatom-bearing and diatom-rich nannofossil ooze of Miocene age. This subunit is characterized by less-pronounced alteration bands and bioturbation.

The upper part of Subunit ID (~270–305 mbsf) consists of dark olive-green nannofossil-rich laminated diatom ooze and a few opal-CT–laminated porcelanite nodules. The lower part is dominated by nannofossils with subordinate amounts of diatoms and radiolarians. Pale greenish gray to purple alteration bands and pale yellow bioturbated intervals are common. High concentrations of pyrite are common in the form of dark gray nodules and pyritized burrows.

Subunit IE (~270–320 mbsf) includes the sediments that directly overlie the oceanic basement. The interval consists of pale yellow diatom-rich nannofossil ooze, which grades into a laminated nannofossil chalk.

The boundaries between the lithostratigraphic subunits match well with major inflection points of magnetic susceptibility and color reflectance curves. Moreover, the latter two curves show a negative correlation through most of the sedimentary section, suggesting that the darker layers (less reflectant) are probably richer in magnetic oxides (higher magnetic intensity).

XRD analyses allowed us to determine that the silica phase transition from amorphous opal-A to the mineral opal-CT occurs between ~250 and 300 mbsf. Such a silica phase change is probably the cause of a decrease in porosity, release of water, and important changes in other physical properties of the sediment. In Subunits IB and ID, the variations of the intensity of bioturbation (plotted as bioturbation index in Fig. F3) are mostly in opposition of phase with the variations of magnetic intensity, thus suggesting either attenuation of the primary magnetic signal by biogenic activity at the sediment/water interface or enhanced bioturbation and chemical alteration of magnetic minerals during early diagenesis of organic-rich sediments.

BIOGEOCHEMISTRY

Site 1225 is characterized by low organic carbon content in sediment and active fluid flow in the underlying basement (Baker et al., 1991). The interstitial water (IW) sampling strategy at this site was designed to clearly define biogeochemical zones and to allow for modeling biogeochemical reaction rates and associated chemical fluxes. Accordingly, IW samples were collected to coincide with samples for microbiological analysis and to concentrate on intervals where higher microbial activity was expected. The chemical data set includes shipboard analyses not routinely employed during ODP cruises (hydrogen, acetate, formate, nitrate, dissolved oxygen, DIC, and high-resolution manganese and iron) as well as quantitative analyses of methane at trace levels.

A total of 29 interstitial water samples were taken from Hole 1225A, one from each of the upper three cores, one from every other core starting with Core 201-1225A-4H (except for Core 18H), and seven additional samples at various intervals (Table T2). The upper two cores were sampled extensively in Hole 1225C, with at least one sample taken from every section of Core 201-1225C-1H and three samples from Core 2H. At greater depths, two interstitial water samples were collected from each core until drilling was terminated at a depth of 305.3 mbsf.

T2. Dissolved species in IW, p. 76.

Overall, microbially mediated reactions drive the variations in interstitial water composition. These reactions result in distinct biogeochemical zones; their establishment and maintenance is largely controlled by diffusive processes across the sediment/water and sediment/basement interfaces as well as by reactions with solid phases in the sediment. Moving from the interfaces toward the sediment in between, we observed a sequence of biogeochemical oxidation-reduction zones, including zones of aerobic respiration, nitrate reduction, manganese reduction, iron reduction, and, finally, sulfate reduction.

Interstitial Water

Alkalinity and DIC have similar downhole profiles. Alkalinity increases from a near-surface value of 2.92 mM to a maximum of 4.25 mM at depths between 100 and 200 mbsf, followed by a decrease downhole (Fig. F5A). There is also a local minimum centered near 50 mbsf, indicating local alkalinity consumption. DIC ranges from a low of 3.2 mM at 3 mbsf to a high of 4.0 mM at 201.7 mbsf; at greater depths DIC decreases to ~3.2 mM at the bottom of Hole 1225C (Fig. F5B). These are the first high-resolution DIC measurements obtained during an ODP leg. Technique development at this first site undoubtedly contributed to the variability in the data, especially in the earliest measurements. DIC is produced by microbial respiration, and alkalinity is primarily produced during sulfate reduction. The net changes in DIC and alkalinity result from production as well as carbonate precipitation driven by equilibration. As with many of the dissolved species at Site 1225, the decrease toward seawater concentrations at depth is due to exchange with water in the underlying basaltic basement.

F5. Dissolved species in IW, p. 43.

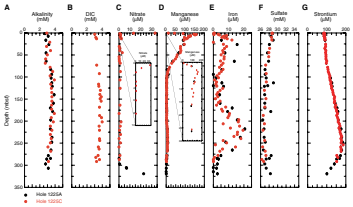

Dissolved oxygen measurements were conducted by microelectrode on selected core sections from Hole 1225C (Sections 201-1225C-1H-1, 1H-2, 1H-3, 2H-1, 2H-2, 2H-5, 32H-7, 33H-2, and 33H-6) and Hole 1225A (Section 201-1225A-35X-5). In each sample, except the one from Section 201-1225A-35X-5, measurements were conducted by inserting the microelectrode probe and reference directly into the core through

holes drilled into the core liner. For the core sample from Section 201-1225A-35X-5, the electrodes were inserted into a segment of the IW whole-round core after loose material had been scraped away. Three sections had detectable concentrations of oxygen: the bottom of Section 201-1225C-1H-1 (50 µM), the top of Section 1H-2 (30 µM), and Section 201-1225A-35X-5 (50 µM). Based on uncertainty in the blank and measured potentials, the analytical uncertainty is estimated to be ~30% for these measurements. The possibility of oxygen infiltrating the sample as a result of cracking associated with the insertion of the probe adds additional uncertainty to the measured oxygen concentration for Section 201-1225A-35X-5; however, accepting the reliability of this measurement implies that the fluid circulating in the underlying basement is oxic.

Nitrate concentrations decrease from 33 µM near the sediment/water interface to <1.5 µM at 1.5 mbsf (Fig. **F5C**). Values remain indistinguishable from zero until ~12 m above the sediment/basement interface and increase to 23 µM in the deepest sample collected (Section 201-1225A-35X-5). Both the shallow and deep gradients are due to microbial nitrate reduction balanced by diffusion into the sediment column. The gradient at the bottom of the hole is consistent with diffuse exchange with a basement fluid that has a nitrate concentration close to that of modern Pacific bottom water (~36 µM) (Levitus et al., 1994).

The downhole profile of dissolved manganese concentrations shows five general features (Fig. **F5D**). Values increase quasi-linearly from the shallowest sample to a peak of 158 µM at 3.65 mbsf (Sample 201-1225C-1H-3, 65–80 cm). Concentrations then decline steadily to ~4 µM at a depth of 110 mbsf and remain below 4 µM, locally decreasing to 2 µM, until 210 mbsf. Dissolved manganese then increases to form a broad peak with values exceeding 7 µM at 250 mbsf. Concentrations are <4 µM from 290 mbsf to the bottom of the hole.

Dissolved manganese has been measured previously at numerous ODP sites, although never in as much detail as at Site 1225. The general profile at this site is similar to that at other open-ocean sites having low to moderate primary productivity in surface waters (e.g., Site 881, northwest Pacific [Shipboard Scientific Party, 1993], and Site 999, Caribbean Sea [Shipboard Scientific Party, 1997]). The concentration peak at 3.65 mbsf probably results from the dissolution of manganese oxide phases driven by microbial manganese reduction. The change in gradient at ~100 mbsf is due to manganese precipitation, most likely as a sulfide phase. The deeper maximum in manganese at 250 mbsf may again reflect bacterial reduction of solid manganese oxide phases.

The downhole profile of dissolved iron concentrations shows considerably more scatter than the dissolved manganese data (Fig. **F5E**). The overall profile consists of two broad peaks centered at ~25 and 230 mbsf. The two iron peaks thus occur more distant from the surface and basement interfaces than the manganese peaks and coincide with intervals of relatively high magnetic susceptibility (see Fig. **F17**). The dissolved iron maxima likely represent release of iron from solid phases such as magnetite by bacterial iron reduction.

The ~50% variation in the iron concentrations of adjacent interstitial water samples raises an intriguing issue because such steep concentration gradients cannot be maintained over significant time. The scatter does not reflect analytical imprecision, which is within ±5% as determined by repeated analysis of samples. Rather, the scatter likely reflects either (1) oxidation during squeezing or water handling that has removed dissolved iron in some samples or (2) detection of particulate

and colloidal iron with particle sizes smaller than the pore size of the filter (0.45 µm) used in collection of the interstitial waters.

Dissolved sulfate concentrations decrease from 28.8 mM at 1.5 mbsf to 27 mM at 83 mbsf and remain near that value for the remainder of the hole (Fig. F5F).

The downhole profile of dissolved strontium is similar to that obtained for Site 851 (Shipboard Scientific Party, 1992). Concentrations are similar to seawater (86 µM) in the uppermost sample at 0.37 mbsf and then steadily rise to 170–186 µM between 220 and 270 mbsf (Fig. F5G). Concentrations sharply decrease to near seawater values above basement. The overall profile suggests an active zone of carbonate recrystallization in lithostratigraphic Subunits ID and IE, with diffusive exchange with a basement fluid similar to seawater.

Concentrations of barium and selected transition metals (copper, molybdenum, nickel, vanadium, and zinc) were below their detection limits in all samples analyzed from Site 1225.

Total sulfide ($\Sigma H_2S = H_2S + HS^-$) dissolved in interstitial water is below the analytical detection limit of 0.2 µM at all depths sampled (Fig. F5H).

The volatile fatty acids, acetate and formate, were examined in 22 IW samples from Holes 1225A and 1225C (Table T2; Fig. F5I). In the majority of samples, acetate was below the detection limit of ~0.5 µM. Formate concentrations exceeded the detection limit of ~0.2 µM in one-half of the samples, with the maximum concentration of 0.9 µM present in the shallowest sample at a depth of 1.50 mbsf (Sample 201-1225A-1H-2, 0–15 cm). Undetectable or extremely low concentrations of acetate distinguish Site 1225 from nearshore coastal environments, where acetate concentrations of ~10 µM are typical.

Methane gas analyses performed during Leg 138 suggested that this gas is present in very low concentrations, presumably at submicromolar levels, throughout the sediment column (Mayer, Pisias, Janecek, et al., 1992). To examine these low gas concentrations, two series of headspace gas analyses were conducted in parallel (see "Gas Analyses," p. 11, in "Biogeochemistry" in the "Explanatory Notes" chapter): (1) the standard procedure in fulfillment of the hydrocarbon monitoring program for safety purposes and (2) a modification of the latter procedure aimed at a more accurate determination of methane concentrations in interstitial water.

Methane was detected in all samples from Holes 1225A and 1225C, with the exception of samples from the very top and bottom of the respective holes. No other hydrocarbons were detected. Methane yields in headspace gas depended on the protocol employed. Methane concentrations in headspace were highest in samples that were extracted for 24 hr and lowest in samples prepared according to the standard safety protocol (extracted at 60°C for 20 min) (Table T3; Fig. F6A). Note that differences in headspace methane between Holes 1225A and 1225C are attributed to the extended extraction time utilized for samples from the latter hole rather than to differences in concentration in these two adjacent holes. Independent of the analytical protocol, all measured values are <3 ppm in the headspace. Even though analyses of methane concentrations in ambient air were highly precise with a standard deviation (σ) below ±0.5 ppm per volume headspace, replicate analyses of selected closely spaced sediment samples had a range approximately twice as large. Accordingly, the relatively high variance of data on a vertical scale of meters to a few tens of meters is interpreted to result from analytical conditions.

T3. Methane in headspace, p. 79.

F6. Methane concentration, p. 45.

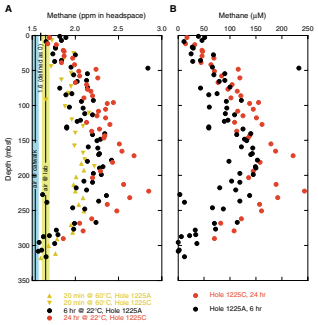

Concentrations of methane in interstitial waters were calculated for both Holes 1225A and 1225C using the porosity estimates derived from gamma ray attenuation (GRA) densitometer measurements (see "Density and Porosity," p. 27, in "Physical Properties"). Despite the variance related to analytical conditions, the overall distribution of methane is well defined. Concentrations increase from background to a broad maximum of 0.1 to 0.2 µM between ~100 and 250 mbsf (Table T3; Fig. F6B). Methane concentrations return to background levels at depth, with the gradient toward the basement being somewhat steeper than the gradient at the sediment/water interface. The broad maximum may reflect a thermodynamic equilibrium concentration under conditions of high sulfate concentrations.

Incubations for hydrogen were conducted on 16 samples. All samples were incubated at 4°C, the approximate midrange temperature (range = 1.4°–7.0°C) of the sediment column (see "Thermal Conductivity," p. 28, in "Physical Properties"). Calculated interstitial fluid concentrations of the incubated sediments are shown in Table T4 and Figure F5J. Between the shallowest hydrogen sample (7.45 mbsf) and 121.45 mbsf, there is a generally monotonic increase from 0.6 to 2.0 nM, except for one sample at a depth of 45.45 mbsf, which has a significantly higher concentration of 3.0 nM. From 140.45 mbsf to the deepest sample at 307.3 mbsf, hydrogen concentrations are lower, ranging from 0.6 to 1.4 nM (average = 1.0 nM). It has been previously observed that hydrogen concentrations measured by this method are defined by the predominant electron acceptor (Lovley and Goodwin, 1988; Hoehler et al., 1998). Concentrations are similar to those observed by Hoehler et al. (1998) in shallow nearshore marine sediments and in experiments where sulfate reduction occurs. A more detailed consideration of the controls on hydrogen concentration requires the analysis of free energies of the dissimilatory reactions that involve hydrogen and are based on measured concentrations of reaction products as well as reactants.

T4. Calculated interstitial water H_2, p. 81.

In Hole 1225A, interstitial water ammonium concentrations are low in the top and bottom sections of the hole, with minima ≤6 µM (Fig. F5K). A broad maximum of 70–77 µM is present at 125–200 mbsf. A similar profile with a broad maximum in ammonium concentrations of ~90–101 µM at the same depth interval was observed previously in Hole 851B (Shipboard Scientific Party, 1992). The deep maximum indicates that production of ammonium.

Dissolved phosphate decreases from 4 µM, a value slightly above local bottom-water concentration, to ~2 µM between 7 and 16 mbsf (Fig. F5L). It is then essentially invariant to a depth of at least 200 mbsf, with the exception of a slight increase from 25 to 75 mbsf. The steep gradient at shallow depths to a minimum at 16 mbsf indicates precipitation of a phosphatic phase such as apatite. The low, relatively invariant phosphate concentrations as compared to ammonium at greater depths suggest that dissolved phosphate concentrations are controlled by equilibrium with a solid phase.

Dissolved silica concentrations increase from 650 µM at the seafloor to 1050 µM at ~180 mbsf (Fig. F5M). The concentrations then vary between 950 and 1100 µM to the base of the hole. The overall downhole trend reflects net dissolution of biogenic silica until a depth of ~150 mbsf. The scatter likely reflects a combination of analytical precision (±40 µM) and variable silica content. Interestingly, silica concentrations do not decrease at the base of the hole, unlike those reported for Site 851 (Shipboard Scientific Party, 1992).

Chloride concentrations increase from 555.1 mM near the sediment/water interface to a maximum of 565.9 mM at a depth of 27.8 mbsf (Fig. F5N). This trend is most likely due to the diffusion of chloride from high-chlorinity glacial seawater out of the sediment column (McDuff, 1985). The values then decline to 563.4 mM at 308 mbsf. This downhole decrease may result from the release of water associated with amorphous silica diagenesis and/or the transport of lower-salinity water from the basement.

Sediments

An extensive set of inorganic carbon analyses exists for Site 851; consequently, during Leg 201 only a broad overview was obtained to provide data for microbiological relationships. The inorganic carbon results from Site 1225 are comparable to those obtained from Site 851 (Shipboard Scientific Party, 1992). In the upper 220 mbsf, $CaCO_3$ percentages are high and variable, ranging from 57% to >80%, with most values between 70% and 80% (Table T5; Fig. F7). Two lower values (42%) are present between 266 and 270 mbsf, with higher values again present at greater depths. The lower $CaCO_3$ percentages at both Site 851 and Site 1225 correspond to more siliceous intervals in the cores (see "Lithostratigraphy," p. 8).

Total organic carbon (TOC) concentrations are low throughout the section, in agreement with the results from Site 851 (Table T5; Fig. F7). All values for TOC are ≤0.42%, with most values falling ≤0.2%.

MICROBIOLOGY

Microbiological sampling for Site 1225 was conducted at regular depth intervals in order to enable a general microbiological inventory throughout the entire sediment column. Microbiology sample intervals of ~19 m resulted from routinely sampling the third section of every second core from Hole 1225A (Fig. F8). Routine subsamples for sulfate reduction rate determinations, deoxyribonucleic acid (DNA), fluorescence in situ hybridization (FISH), adenosine triphosphate (ATP), hydrogen, and lipid biomarker analyses were accordingly taken from each of these samples and processed, fixed, or frozen, as appropriate. Samples for AODC were fixed from the same intervals, and the cells were counted on the ship. A 15-cm segment from every microbiology core section was immediately transferred to the geochemistry laboratory for chemical analysis of interstitial water. Activity measurements, such as bicarbonate turnover, acetate turnover, thymidine incorporation, and hydrogen turnover, were conducted on a subset of the routine samples, in particular, at the upper and lower ends of the sediment column. Samples for cultivations were taken with the aim of comparing distinct depths and chemical zones in the sediment column. Cultivation samples were taken from the surface or the near-surface sediment column (Core 201-1225A-2H), from intermediate depths near 100 and 200 mbsf (Cores 12H and 22H), and from the deepest core of the sediment column (Core 34H) (Fig. F8).

Microbiological sampling in Hole 1225C focused on two additional sample sets (Fig. F9). The mudline core of Hole 1225C was sampled at three depths (Sections 201-1225A-1H-1, 1H-3, and 1H-6) to obtain finer resolution near the sediment surface, where the steepest biogeochemical gradients had been encountered during ODP Leg 138 and were con-

T5. Calcium carbonate and organic carbon, p. 82.

F7. Calcium carbonate and organic carbon, p. 46.

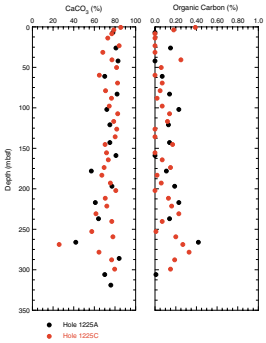

F8. Subsampling for MBIO sections, Hole 1225A, p. 47.

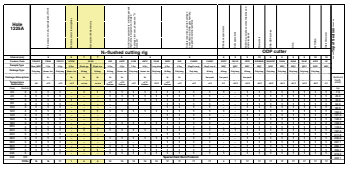

F9. Subsampling for MBIO sections, Hole 1225C, p. 48.

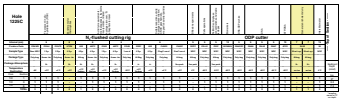

firmed by interstitial water analyses from Hole 1225A. Sampling depths for cultivation of manganese-reducing bacteria in Hole 1225C were chosen according to the analyzed manganese profile of Hole 1225A (Fig. F5).

To explore the composition of microbial communities associated with oceanic crust and their contribution to basalt weathering, XCB drilling into basement rock was performed (Core 201-1225A-35X; 319.6 mbsf). The core catcher yielded a few fragments of basaltic rock, which were sampled separately using a specially designed sample processing scheme (see "Rock Sampling and Distribution," p. 22).

Total Bacterial Enumeration

Samples of 1-cm^3 plugs for prokaryotic cell enumeration were taken on the catwalk from a total of 25 depths between 0.8 and 8.37 mbsf in Hole 1225C (3 samples) and between 8.8 and 319.6 mbsf in Hole 1225A (22 samples). Prokaryotes were present at all 25 depths (Fig. F10). The greatest abundance of cells was found in the near-surface sample (Sample 201-1225A-1H-1, 80–85 cm), which contained 7.5×10^6 cells/cm^3, and the smallest number of cells was found near the sediment/basement interface at 320.45 mbsf (Sample 201-1225A-35X-CC, 0–1 cm), which contained 1.8×10^5 cells/cm^3, a factor of 42 decrease in cell density. The overall depth profile follows a trend observed at other ODP sites (Parkes et al., 1994); however, absolute numbers of prokaryotes are considerably lower than the average numbers for all previously examined sites, particularly in the upper 65 m (Fig. F11), apart from a small increase at ~35 mbsf. Between ~70 and 280 mbsf, data generally agree with the average of previously studied ODP sites, albeit at the lower end of the range, but from ~300 mbsf, prokaryote numbers are again significantly lower than the average.

Site 1225 is located within 100 m of Site 851 (Leg 138), from which prokaryotic counts were previously made (Cragg and Kemp, 1995). There is broad agreement between the two data sets, with an upper zone containing low prokaryotic cell numbers, a central zone of relatively elevated numbers, and low numbers near the basement. Overall, prokaryotic cell counts made at Site 851 are higher than those presented here. At Site 851, prokaryotic cell numbers decreased significantly near basement, reaching 3.7×10^5 cells/cm^3 at 317.4 mbsf. This value is not significantly different than that determined here.

Counting techniques have improved since Leg 138, allowing lower detection limits—estimated here at 4.7×10^4 cells/cm^3 (compared to 1.8×10^5 cells/cm^3; Cragg and Kemp, 1995)—and therefore increased sensitivity. Numbers of dividing cells (suggested as an index of population activity) are typically <10% of the total count. As expected, dividing cells as a percentage of the total count are high near the surface (Fig. F10) and are also elevated between ~55 and 200 mbsf. This agrees with data from Site 851. However, two more increases are identified in the data presented here: one at ~30–50 mbsf and another at 230–270 mbsf. The reasons for these increases are not clear. However, the lower increase occurs at the same depth as increases in dissolved manganese, dissolved iron, TOC, and a probable increase in methane, all indicative of bacterial activity (see Fig. F5).

Samples for prokaryotic cell counts were taken from five slurries prepared in the laboratory, as 2 mL of 25% slurry. Slurries were made from Cores 201-1225A-2H, 12H, 22H, and 34H and from Core 201-1225C-

F10. Prokaryotic cells enumerated by AODC, at Site 1225, p. 49.

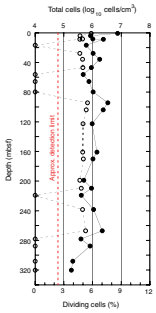

F11. Total prokaryote profile, p. 50.

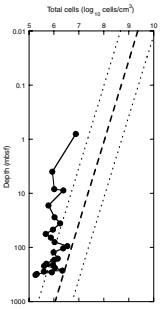

1H. Total counts on five slurry samples did not differ significantly from total counts on adjacent plug samples.

Contamination Tests

While drilling cores for microbiology, the potential for contamination with bacteria from the surface is highly critical. Contamination tests were continuously conducted using solutes (PFT) or bacterial-sized particles (fluorescent microspheres) to check for the potential intrusion of drill water from the periphery toward the center of cores and thus to confirm the suitability of the core material for microbiological research. We used the chemical and particle tracer techniques described in ODP *Technical Note* 28 (Smith et al., 2000). Furthermore, the freshly collected cores were visually examined for possible cracks and other signs of disturbance by observation through the transparent core liner. Core sections observed to be disturbed before or after subsampling were not analyzed further. Such disturbance phenomena are critical to the integrity of the core material and therefore also to its usefulness for microbiological studies.

Perfluorocarbon Tracer

The PFT experiments use a dissolved organic tracer, perfluoromethylcyclohexane, to estimate the level of seawater contamination that has penetrated into sediment cores during drilling. The PFT was injected continuously into the drilling fluid during drilling of Holes 1225A and 1225C. Because the PFT is dissolved in the drilling fluid rather than suspended as a particle, these results are estimates of the potential for microbial contamination and are expected to provide an upper limit of actual microbial contamination. Subcores of 5 cm^3 were taken from the bottom cut of each microbiology (MBIO) section or from the adjacent top of the immediately underlying section, and 5-mL aliquots were taken from each master slurry. Samples from the core catcher were collected to measure the concentration of PFT in samples recovered from the near-basement sample. The delivery of PFT to the drill bit was positively confirmed by measuring the concentration of PFT in drilling fluid removed from the top of the core or by detection of PFT in sediment smeared along the periphery of the core.

At Site 1225, the results of PFT experiments were for the most part ambiguous because of analytical problems and because of problems with sample handling on the catwalk. In particular, gas chromatograph (GC) traces had small peaks (other than the PFT) of similar retention time to that of the PFT. Further, catwalk samples were taken by syringe at the end of sections without using a fresh, sterile scalpel to remove the surface layer contaminated by the slicing of the sections. These problems mostly resulted in ambiguous and unusable results for Site 1225.

However, in a few cases, the results clearly indicated no PFT contamination. These were subcores taken from Cores 201-1225A-16H, 30H, 32H, and the "master slurry" taken from Core 22H. All of these samples had PFT concentrations below detection (corresponding to <0.02 µL seawater/g sediment). Additionally, there were several cases with PFT concentrations so high that there is no ambiguity as to whether or not these were contaminated by seawater during the drilling process. These were all the samples taken from the core catcher from Core 201-1225A-

35X, with PFT concentrations suggesting contamination of ~3 µL seawater/g sediment.

Assuming 5×10^8 bacterial cells/L surface seawater, each 0.1 µL of seawater contamination may represent as many as 50 contaminating cells if the sediment is porous enough to allow the cell to travel with the PFT.

Particulate Tracer

Fluorescent microspheres were used as a particulate tracer on all five cores from which slurries were subsequently made in the laboratory. A 10-mL sample of slurry was processed from each slurry for microsphere detection. Microspheres were detected in two of the five slurry samples (Table T6), indicating potential contamination from drilling fluid. The method of delivery prevents a usefully quantitative estimate of the amount of contamination and can only give a minimum for the amount of contamination. In all cases, the sample taken for direct prokaryotic cell counts was also used as a confirmation sample for the presence or absence of microspheres. Where microspheres were not detected in either sample, further samples from the outside of the relevant cores were taken to confirm microsphere delivery.

T6. Potential contamination of slurries, p. 83.

Overall, both the PFT analyses and the bead counts suggested that the slurry from Core 201-1225A-22H was not contaminated. Only trace amounts of PFT were detected in the subcore, and neither PFT nor beads were detected in the slurry itself. The most substantial contamination, with respect to PFT levels, was found in the XCB core catcher (Core 1225A-35X-CC), from which the basaltic rock samples were obtained. The high bead counts occurring simultaneously with low PFT values in two of the slurries from Sections 201-1225A-2H-3 and 12H-3 suggests that contamination did not occur during drilling but rather occurred during sample handling and processing.

Cultivations

All most probable number (MPN) dilutions and enrichments inoculated using samples from Site 1225 are listed in Table T7. A strong indication for manganese(IV) reduction was given by the manganese(II) interstitial water profile, showing a pronounced peak of manganese(II) close to the sediment surface (Fig. F5). Consequently, MPN enrichments of manganese(IV)-reducing bacteria were made at high resolution in Hole 1225A.

T7. Media inoculated with material from Site 1225, p. 84.

Growth was observed after the first few days of incubation in some of the following enrichment experiments:

1. At 25°C on medium 201-1 (see Table T5, p. 85, in the "Explanatory Notes" chapter) for anaerobic heterotrophs with elemental sulfur as possible electron acceptor, inoculated with slurry made from sediment from the core catcher at the bottom of Hole 1225A (Section 201-1225A-35X-CC). Cells are rather large short rods.
2. At 25°C on medium 201-3 (see Table T5, p. 85, in the "Explanatory Notes" chapter) for anaerobic nitrate-reducing heterotrophs, inoculated with slurry made from sediment from Section 201-1225A-35X-CC. Cells are large rods, partly in chains.
3. At 60°C and pH 8.0 on heterotrophic xylose/ribose-containing medium (Ferm) (see Table T7, p. 88, in the "Explanatory Notes"

chapter) for fermenting bacteria inoculated with sample from near-surface Section 201-1225C-1H-1. Cells are very small short rods.

These first positive results need to be confirmed by further subculturing and verifying by molecular data. Furthermore, the potential for previous contamination of the samples used for enrichment was higher at this first site of Leg 201 than at the following sites. This is particularly true of the first two examples shown above, where high levels of contamination were observed, and illustrates the potential problems of contamination in XCB cores.

FISH-SIMS

Samples were routinely taken for postcruise FISH-secondary ion mass spectrometry (SIMS) analyses from each sampled core section (Fig. F8). In most cases, a 5-cm^3 subcore was injected into 10 mL of filtered ethanol:phosphate buffered saline (PBS) solution and stored at –20°C. However, the samples taken from Cores 201-1225A-2H and 12H and Section 201-1225C-1H-6 were fixed in 3.7% formaldehyde, washed, and stored at –20°C. In addition, a single subsample of the basalt from Core 201-1225A-35X was also collected for postcruise SIMS analysis. This sample was stored in 10 mL of filtered ethanol:PBS solution and stored at –20°C.

^{13}C substrate incubations were initiated for postcruise analysis by FISH-SIMS using material from Cores 201-1225A-2H, 12H, and 22H. In this case, 10 mL of the master slurry was injected into each bottle. For Cores 201-1225A-2H and 12H, the ^{13}C substrates used were methane, acetate, or glucose. For Core 201-1225A-22H, the ^{13}C substrates used were acetate or glucose, with two of each initiated on board.

Rock Sampling and Distribution

Two rock pieces (dark gray to black basalt) were obtained from the core catcher of the lowermost core (Core 201-1225A-35X). These pieces included an oval rock (Fig. F12) (3 cm × 2 cm × 2 cm) and an elongated, thinner rock (2 cm × 1 cm × 1 cm). The rocks were embedded in disturbed sediment, indicative of seawater contamination. Adhering sediment particles were removed by washing the rocks individually in a 250-mL Pyrex bottle containing 50 mL of nitrogen-flushed marine salts solution (see "Rock Sampling," p. 35, in "Microbiology" and Table T8, p. 89, both in the "Explanatory Notes" chapter). After the first washing step, the rocks were transferred into a second wash bottle with fresh nitrogen-flushed marine salts solution and washed again by shaking and rinsing. After this step, the rocks were handled with a sterile forceps and cleaned individually by scraping small remaining pockets of metal oxide and whitish sediment from the surface using sterile syringe needles. The loosened particles were rinsed off with nitrogen-flushed marine salts solution from a syringe.

F12. Basalt from an XCB core catcher, p. 51.

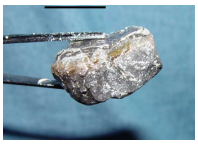

One rock piece was too large for the shipboard rock crusher. It was wrapped in sterile aluminum foil and broken into pieces by repeated energetic strokes with a hammer. The pieces were divided as follows:

1. Small chips and a larger weathered piece were placed in a sterile plastic bag for thin sectioning and petrographic analysis.

2. A weathered piece was stored in PBS/50% ethanol for ion microprobe analysis.
3. The surface of a larger piece was sterilized by soaking in 3-M HCl for 1 min, subsequently washed three times in sterile marine salts solution, crushed into smaller pieces, and used for inoculation of different media at 10° and 15°C. This procedure aimed at isolating endolithic bacteria free of surface contaminants using different media (including media containing combinations of H_2/HCO_3^-/Fe(III)/Mn(IV) for chemolithoautotrophs).
4. Small pieces of crushed rock were collected for inoculation of enrichment media.
5. Small pieces of crushed rock were fixed for AODC.
6. Small pieces of crushed rock for DNA extraction were frozen at –80°C.
7. Small pieces of crushed rock were fixed in PBS/4% formaldehyde for 4′,6-diamindino-2-phenylindole (DAPI) staining, FISH, and thin sectioning.

The smaller rock piece was crushed in a sterile rock crusher and the pieces were divided up as follows:

1. A larger piece was collected for electron microscopy.
2. Smaller pieces were collected for inoculation of enrichment media.
3. Small chips for DNA extraction were frozen at –80°C.

The combined first washes of the two rocks had the consistency of a sediment slurry (100 mL volume; ~10% vol/vol sediment at the bottom), very similar to the slurry from Section 201-1225A-34H-3. This rock-associated sediment was split for the following:

1. Isolations,
2. DNA extractions,
3. AODC counts, and
4. DAPI and FISH analyses.

PHYSICAL PROPERTIES

In this section we describe the downhole distribution of physical property data collected from Site 1225 and compare these data with those from Site 851. Where data were collected at higher spatial resolution than at Site 851, we explain the scientific reasons and objectives for this sampling strategy and interpret the results. New data that were not collected at Site 851 include IR emission and electrical resistance.

A variety of physical property measurements were routinely collected on whole-round sections at Site 1225 to provide downhole data for correlation purposes and for integration with chemical and biological samples. A scan of IR emission along the entire core surface was recorded for most cores from Hole 1225A prior to sectioning and sampling on the catwalk. After sectioning, multisensor track ([MST] magnetic susceptibility, GRA density, *P*-wave velocity, and natural gamma radiation [NGR], for all holes) and thermal conductivity measurements (for Hole 1225A only) were made on whole-round sections, with the exception of those sections removed on the catwalk for microbiological sampling. Several IR images of exposed section ends were taken to monitor inner

core temperature and warming during catwalk sampling. From split cores, we took discrete undisturbed samples for measuring moisture and density (MAD) properties (dry volume and wet and dry mass). We also measured compressional wave velocities using the digital sonic velocimeter and resistance using a third-party device.

Our sampling strategy was designed to address specific leg and related research objectives while maintaining core flow through the laboratory. For Holes 1225A and 1225C, measurement spacings, count times, and data acquisition schemes (DAQs) used for the MST were as follows: magnetic susceptibility meter (spacing = 5 cm, DAQ = 2 × 1s), GRA densitometer (spacing = 10 cm, count time = 5 s), *P*-wave logger (PWL) (spacing = 10 cm, DAQ = 10), and NGR (spacing = 30 cm, count time = 15 s). Hole 1225B comprised a single core that was run at higher resolution and precision on the MST: magnetic susceptibility meter (spacing = 2 cm, DAQ = 1 × 10 s), GRA densitometer (spacing = 2 cm, count time = 10 s), PWL (spacing = 10 cm and 2 cm, DAQ = 10), and NGR (spacing = 15 cm, count time = 30 s). Voids and cracking were logged for the MST where separation was visible, and data were not recorded over these intervals.

MAD, *P*-wave velocity from the velocimeter, and resistance data were only collected from Hole 1225A because of the high degree of correlation between the Site 851 and Hole 1225A MST data. Samples were taken at four per section for the top 10 m (Sections 201-1225A-1H-1 through 2H-6) and the lowermost 20 m (Sections 33H-6 through 35X-4). In between, properties were measured at one per section. MAD measurements were uploaded to the ODP (Janus) database and were used to calculate water content, bulk density, grain density, porosity, void ratio, and dry bulk density. *P*-wave velocities were measured in two directions (PWS1 and PWS2) over the interval 0–3.54 mbsf (Section 201-1225A-1H-3), and thereafter, only PWS3 data were able to be collected. Resistance and porosity measurements were used to compute formation factors for Hole 1225A.

Most of the physical property data show breaks or variation in downhole trends that coincide with the lithostratigraphic boundaries defined by the sedimentology (see **"Lithostratigraphy,"** p. 8). We have indicated these on the accompanying diagrams and explain their physical origin in the summary.

Instrumentation and measurement principles are discussed in **"Physical Properties,"** p. 41, in the "Explanatory Notes" chapter.

Infrared Scanner

Except where there were problems booting the camera and/or computer, each core from Hole 1225A was scanned from top to bottom on the catwalk with an IR camera. The camera was mounted on a trolley and pushed by hand along the core, which resulted in inconsistent scan times ranging between 30 s and 1 min and scan video files ranging from 150 to 330 images. Because of these inconsistencies, extensive postprocessing is required to create a composite downhole plot of depth against core liner temperature. This precluded correlations with other properties. However, a preliminary examination of the data set was conducted.

Selected files were analyzed to produce downhole plots of core liner temperature vs. scan time (i.e., vs. relative depth) (Fig. **F13**). The plots illustrate that core liner temperature varies by up to 2°C along each core, but there is no consistent pattern to this variability from core to

F13. Temperature trends measured with the IR camera, p. 52.

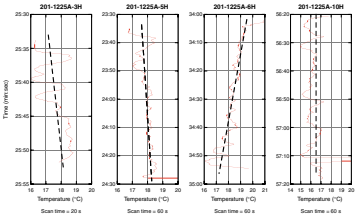

core. We speculate that this absence of a pattern between cores, some scanned only an hour apart, might be attributed to two factors. First, the camera has a significant sensitivity to reflection and ambient light. Although we employed a shield to minimize this effect, the shield may not be adequate. Inconsistencies in ambient light arise from the time of scanning (e.g., day vs. night) and possibly from a slight rocking in the motion of the trolley. Second, the cores are handled by many people prior to scanning on the drill floor and on the catwalk, and it is possible that the duration of their contact with the core results in the minimal temperature variation measured along the length of the core liner.

A comparison of scan profiles of cores from similar depths in Holes 1225A and 1225C (Cores 201-1225A-12H and 201-1225C-12H) was attempted, but no correlation was found, despite similar scan times (Fig. **F14**).

Single IR images were recorded from a selection of section ends before capping, in order to obtain information about the radial temperature distribution at the time of microbiological sampling (see Fig. **F15** as an example). We conducted two experiments on the catwalk during which time-lapse images of a warming transverse (base of Section 201-1225A-11H-6) and longitudinal section (Section 26H-6) were acquired every 15 s over a continuous period of 18 min. The ambient air temperature was 28°C. For the transverse section, the initial temperature profile core center temperature was 9.6°C and liner temperature was 18.4°C at time zero. At the end of the experiment, temperatures were 18.5° and 21.0°C, respectively (Fig. **F16**). We conducted a similar longer-term experiment in the shipboard laboratory to examine the warming of the interior of the cores. Every 15 min, 10 cm was cut from Section 201-1225C-20H-7. For these video sequences, the temperatures seen on the IR images were calibrated against core temperature measured by thermistor. Thermal conductivity was also recorded, and a sample was removed for emissivity analysis of the sediment.

From these preliminary tests we can conclude that the cores from this site have surface temperatures that vary on the order of 2°C along the core when they arrive on the catwalk. The temperature at the center of each core was on the order of 10°C lower than the surface temperature. The ends exposed after sectioning take at least 20 min to equilibrate to ambient temperature. Overall, the setup used for data collection at Site 1225 does not lead to consistent and repeatable temperature measurements of the cores in the range of conditions encountered.

Magnetic Susceptibility

Low-field volume magnetic susceptibility was measured on the MST using the Bartington loop sensor described in **"Magnetic Susceptibility,"** p. 44, in "MST Measurements" in "Physical Properties" in the "Explanatory Notes" chapter. The data correlate well with the Site 851 data across the entire downhole profile (Fig. **F17**). Average magnetic susceptibility varies between 3×10^{-5} and 8×10^{-5} SI units from 0 to 69 mbsf.

From 69 to 72 mbsf, the magnetic susceptibility declines steadily, consistent with the record from Site 851. From 72 to 190 mbsf, magnetic susceptibility remains level at ~0×10^{-5} SI units. Between 190 and 230 mbsf, magnetic susceptibility increases to ~10×10^{-5} SI units. From there it declines steadily to 300 mbsf, where it again reaches 0×10^{-5} SI units, except for a peak at 256 mbsf. Between 300 mbsf and the base of the sedimentary section, magnetic susceptibility climbs back to an average of ~2×10^{-5} to 3×10^{-5} SI units.

F14. Comparison Holes 1225A and 1225C, p. 53.

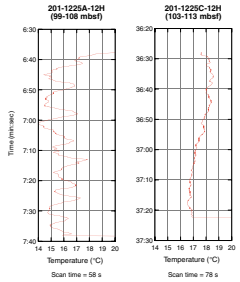

F15. Bottom end of a core immediately after section splits, p. 54.

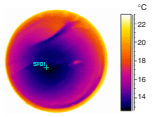

F16. Temperature increase of an exposed section end, p. 55.

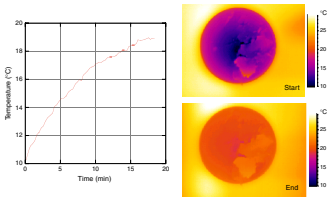

F17. Magnetic susceptibility data, Sites 1225 and 851, p. 56.

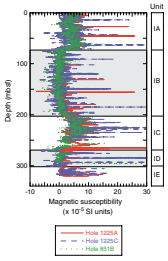

Our data for Hole 1225A show high magnetic susceptibilities (up to 1292 × 10^{-5} SI units), primarily in sections 1 and 2 of every core, and sporadically below this in most cores below Core 201-1225A-3H. Chips of rusty metal, 1–2 mm in diameter and present variably in layers up to 10 cm thick or as individual grains, are visible through the core liner. We believe these chips came from the drill pipe, concentrated at the base of the hole during each core trip, and then were sampled at the top of the succeeding core. The problem persisted to the base of Hole 1225A but did not affect Holes 1225B or 1225C.

Paleomagnetism

Cores from Hole 1225A were run on the cryogenic magnetometer to correlate with data collected at Site 851 and to investigate whether the paleomagnetic record is preserved in the lower part of the hole where magnetic susceptibility is high. Paleomagnetic data were not collected at Site 851 below 150 mbsf. Study of the Site 1225 cores only included those taken from zones of high magnetic susceptibility (Cores 201-1225A-1H through 11H [0–90 mbsf] and Cores 21H through 34H [190–300 mbsf]). The first two cores were measured for natural remanent magnetization (NRM) and were demagnetized to peak alternating fields (AFs) of 5, 10, 15, and 20 mT. The remaining cores were measured for NRM and cleaned at 15 mT. In order to correct for orientation, the magnetic readings from the Tensor tool and the local geomagnetic deviation (8.9°) were added to the declination measured by the cryogenic magnetometer.

The results correlated well to the detailed magnetic work conducted at Site 851. There is more noise at the top of the cores, likely due to the iron filings from the drilling, mentioned above. In the interest of time, our paleomagnetic interpretation was limited to the identification of normal and reversed epochs in the uppermost 90 m (Fig. **F18**). The reversal record for the lowermost section (190–300 mbsf) is less clear (Fig. **F18**). However, it does appear to contain a reversal record. Therefore, we conclude that the signal has not been completely degraded by time. This could suggest stability in the iron geochemistry of this zone over millions of years.

At Site 1225, we collected 32 discrete samples for paleomagnetic measurements from the working halves of the core. The sampling frequency was one sample from each core from Hole 1225C (Cores 201-1225C-1H through 27H; 0–254.5 mbsf). AF demagnetization of the NRM was conducted up to 40 mT in 10- or 5-mT steps on ~29 samples. Anhysteretic remanent magnetization (ARM) was measured to 40 mT in 10-mT steps with a 29-µT direct current–biasing field. AF demagnetization of the ARM was conducted to 40 mT in 10-mT steps. The rest of the samples will be thermally demagnetized on shore.

The intensity after 20-mT AF demagnetization in Hole 1225C samples agrees with the intensity after 15-mT AF demagnetization measured by the cryogenic magnetometer in Hole 1225A samples (Fig. **F19**). Lithostratigraphic Subunits IA and IC (see **"Lithostratigraphy,"** p. 8) exhibit higher magnetic intensity. The uppermost brown sand-sized foraminifer-, diatom-, and radiolarian-rich nannofossil ooze containing iron and manganese oxides (Sample 201-1225C-1H-2, 93.5–95.5 cm) strongly shows the effect of downward drilling-induced overprint (Fig. **F20**). A pale brown layer (Sample 201-1225C-1H-3, 109–111 cm) below the brown layer shows a more stable magnetization (Fig. **F21**). The white foraminifer-, diatom-, and radiolarian-rich nannofossil ooze with

F18. Declination and inclination profiles, p. 57.

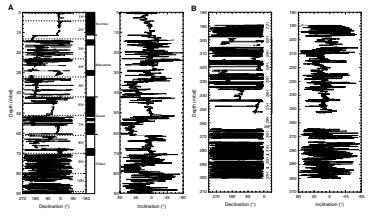

F19. Magnetic intensity at Site 1225, p. 58.

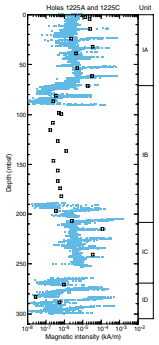

F20. Principal component analysis, 201-1225C-1H-2, 93.5–95.5 cm, p. 59.

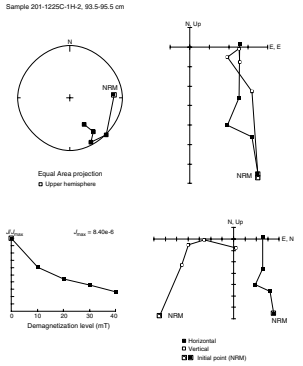

F21. Principal component analysis, 201-1225C-1H-3, 109–111 cm, p. 60.

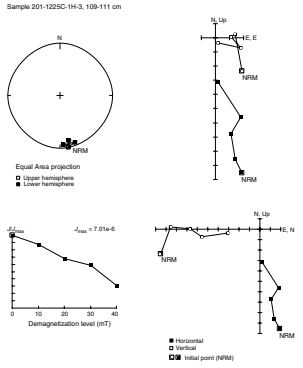

purple pyrite laminae layers (Sample 201-1225C-5H-1, 138–140 cm) in lithostratigraphic Subunit IA shows a magnetic direction that was not demagnetized by AF demagnetization up to 40 mT (Fig. F22).

Pale yellow and yellowish white diatom-bearing nannofossil ooze layers (Samples 201-1225C-23H-5, 69–71 cm, and 26H-3, 87–89 cm) in lithostratigraphic Subunit IC show higher intensity than those in Subunit IA. AF demagnetization as high as 40 mT could not demagnetize these samples, which is probably due to postdepositional chemical remanent magnetization (for an example see Fig. F23). Thermal demagnetization is needed to determine the magnetic carrier and original directions.

Density and Porosity

Density data were measured on the MST by the GRA densitometer and calculated from the MAD data. GRA data from Holes 1225A and 1225C were compared with the Hole 851B data (Fig. F24). Data from Holes 1225A and 1225C were collected with a 5-s count time at 10-cm spacing. GRA density increases from 1.40 to 1.62 g/cm³ over the interval 0–190 mbsf and then declines back to 1.4 g/cm³ by 250 mbsf. Below 250 mbsf, GRA density first increases to 1.64 g/cm³ at a depth of ~260 mbsf and then falls to a low of 1.2 g/cm³ at 270 mbsf. At 294 mbsf, GRA density peaks at a downhole maximum of 1.74 g/cm³ before declining to ~1.54 g/cm³ at the base of the Hole 1225A.

The scatter for the 2- and 5-s count times (Holes 851B and 1225A, respectively) was compared using a 5-m moving average, and it was determined that the two are not statistically significantly different (Fig. F25). The downhole profiles correlate well and can be used for meter-scale correlation with confidence. Regular or cyclic downhole variability in GRA density data with a spatial frequency on a scale of ~10 m is greater than for any other physical property data collected at comparable spatial resolution at Site 1225.

Moisture and density measurements for Hole 1225A (Fig. F26) compare favorably to both Leg 201 GRA-derived and Leg 138, Hole 851B GRA- and mass/volume-derived values (Fig. F25). Grain density measurements (Fig. F26B) exhibit much greater scatter than the results of Hole 851B, which we attribute to initial pycnometer (volume) errors at this site. Combining Holes 851B and 1225A grain density data sets results in the following average grain densities:

Subunit IA = 2.66 g/cm³,
Subunit IB = 2.60 g/cm³,
Subunit IC = 2.54 g/cm³,
Subunit ID = 2.62 g/cm³, and
Subunit IE = 2.62 g/cm³.

The subunit-specific bulk density–porosity pattern is thus dominated by water content variability and not by changes in grain densities. Of particular interest are the four ~40-m porosity cycles in Subunit IB, in which porosities fluctuate by 10%–12%. Postcruise analysis must be performed to determine the lithologic, diagenetic, and consolidation attributes responsible for this pattern.

F22. Principal component analysis, 201-1225C-5H-1, 138–140 cm, p. 61.

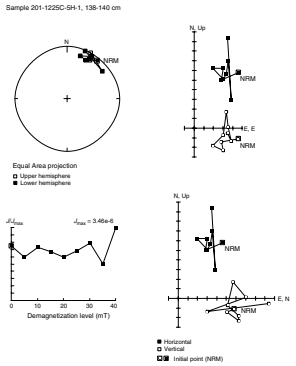

F23. Principal component analysis, 201-1225C-12H-5, 69–71 cm, p. 62.

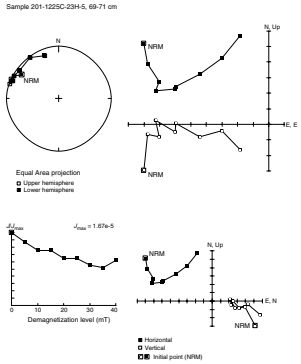

F24. GRA density, Sites 1225 and Site 851B, p. 63.

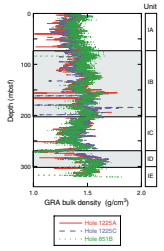

F25. GRA density overlain on MAD measurements, p. 64.

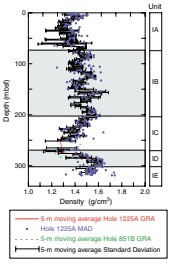

Compressional Wave Velocity

P-wave data from the MST PWL were recorded from all cores, with the exception of the XCB core at the base of Hole 1225A (Core 201-1225A-35X). *P*-wave velocities were also measured using the *P*-wave velocimeter insertion probe system along the core axis (z-axis) and across the core axis (y-axis) (PWS1 and PWS2, respectively). The PWS3 contact probe system was used to measure *P*-wave velocities through the cut half of the core (x-axis). Measurements were taken either in the z- and y-axis directions (Section 201-1225A-1H-3 and shallower) or in the x-axis direction. Very rarely were all three directions able to be recorded at a single location. Expansion cracks were variably present in the cores, probably resulting in some attenuation of the acoustic signal, but only in a few places was wetting of the core required to allow transmission of the acoustic pulse. The velocity profiles recorded by the PWL on the MST read consistently slower than those from the velocimeter (Fig. F27). From 0 to 182 mbsf, the PWS3 was the faster by ~20 m/s. Between 182 and 250 mbsf, the two are in reasonable agreement, but below this interval, the PWS3 value is again generally faster by ~15 m/s. Both downhole velocity profiles illustrate an increase from seafloor velocities to peaks at ~20 mbsf, and then they decline to lows at ~65 mbsf. Below this level velocities gradually increase, reaching ~1550 m/s just below 150 mbsf (based on the velocimeter data). Velocities then decline to downhole lows of ~1495 m/s at ~220 mbsf. Below 220 mbsf, velocities increase irregularly to reach a downhole high of ~1580 m/s. Although the general shape of the velocity profiles is similar to other physical property parameters, there is no direct correlation between peaks and troughs at depth.

Natural Gamma Ray Emission

Natural gamma radiation was measured on the MST track for Holes 1225A and 1225C (spacing = 30 cm, count time = 15 s) and was also measured by wireline logs. The NGR profile shows a minimal downhole trend, decreasing from ~13–14 counts per second (cps) total emission near the top of both holes to ~12–13 cps at the base of both holes (Fig. F28). There are narrow peaks of 17–19 cps at depths of 84, 110, 265, and 302 mbsf, and above 3 mbsf, the count is consistently >20 cps. There is good correlation between the GRA density, the NGR, and the wireline log data. The GRA data tend to be noisier than the wireline data, with some cyclicity present in the latter that are not obvious in the former.

Thermal Conductivity

Thermal conductivity measurements were made in Hole 1225A at a rate of one per core (usually section 3 at 75 cm, if this was available). Values range between 0.77 and 1.11 W/(m·K) (average = 0.89 W/[m·K]). A slight but steady downhole increase is the only perceptible trend in these data (Fig. F29A).

A plot of average normalized thermal conductivity vs. bulk density (Fig. F29B) shows almost exact correlation, indicating that the thermal conductivity is a direct function of water content of the sediments. The only obvious deviation from this relationship is at a depth of ~170 mbsf, where the thermal conductivity is lower than expected for the measured bulk density.

F26. GRA and grain density and porosity, p. 65.

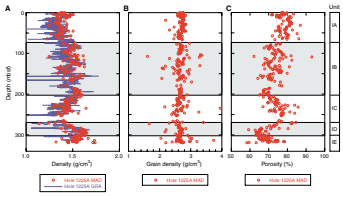

F27. MST and PWS velocity profiles, p. 66.

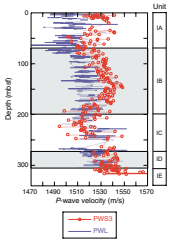

F28. Comparison of NGR measurements, p. 67.

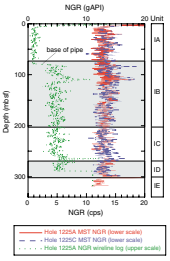

F29. Thermal conductivity and projected temperature profiles, p. 68.

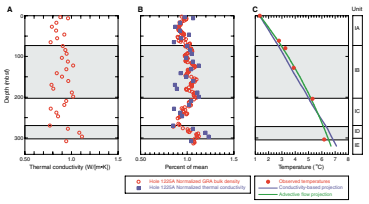

Several methods were used to analyze the temperature data measured by the downhole probe and to reconcile these with the thermal conductivity data. A linear fit of the temperature profile has a correlation coefficient of $R^2 = 0.97$, indicating a deviation from the linear model that cannot be explained by measurement error. To examine deviations caused by variations in the thermal conductivity, a temperature gradient for each core was computed by dividing the core length by the measured thermal conductivity and multiplying by the average heat flow. These gradients were combined to form the composite temperature profile shown in Figure F29C. The composite result shows that variations in the measured sediment thermal conductivities cannot explain the temperature deviations from a linear profile. The temperature data are best fit by a profile that curves downward. In some cases, curved temperature profiles can be caused by downward increases in thermal conductivity. However, the thermal conductivities measured at Site 1225 show large variability and only a slight downward increase of 0.3 mW/(m·K)/km (Fig. F29A). Fitting the temperature profile curvature with a steady-state conductive model requires a rate of thermal conductivity increase eight times greater than that of the measured values. Curved profiles can also be caused by upward flow of fluids transporting heat from deeper in the section. Using a model of steady-state fluid flow with advective heat transport requires an upward flow velocity of ~2 cm/yr to match the curved profile. This flow rate is an order of magnitude greater than that obtained by fitting the Site 1225 chloride interstitial water concentrations (see "Interstitial Water," p. 14, in "Geochemistry"). An alternative model that would generate the observed profile is a transient lowering of the basement temperature. The timing required for a basement temperature transient was not analyzed.

Formation Factor

Formation factor was determined from resistance measurements taken using the four-needle electrode array. Resistance measurements were normalized against the resistance of surface seawater, which was measured periodically as the sediment measurements were made. The data show an overall downhole increase (Fig. F30), which is consistent with a decline in porosity with depth. The only zone that deviates from this trend lies between 265 and 287 mbsf, where the formation factor is consistently lower than the linear downhole trend of the data.

A plot of anisotropy of conductivity (Fig. F30) shows a wide scatter across Subunits IA and IE, indicating that laminations in the sediment are restricting interstitial water flow to dominantly horizontal pathways. In contrast, Subunits IB, IC, and ID are more homogeneous in their conductivity structure, suggesting equal vertical and horizontal flow.

F30. Formation factor and conductive anisotropy profiles, p. 69.

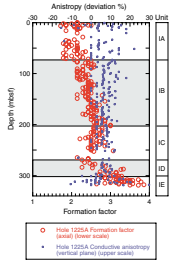

Summary and Discussion

The physical properties measured on cores at Site 1225 correlate well with those obtained during Leg 138 at Site 851. In this section, we summarize the correlation between different physical properties and interpret the physical origin of the lithostratigraphic boundaries and subunits defined in "Lithostratigraphy," p. 8.

Subunit IA (0–70 mbsf) has low but consistent magnetic susceptibility and consistently high GRA density.

The boundary between Subunits IA and IB corresponds to the loss of magnetic susceptibility. The boundary is not discernible on the MST NGR record and lies within the attenuation zone of the drill pipe for the wireline NGR data. This boundary is also the point at which sonic velocity starts to increase from a reasonably stationary downhole trend in Subunit IA, but these data are very noisy and could not be used to reliably pick the transition. Similarly, there is no clear break in either of the density data sets that corresponds to the boundary. The thermal conductivity record has a much lower spatial resolution than the other records and cannot be used in defining the transition.

Subunit IB (70–200 mbsf) is characterized by little or no ferrimagnetic mineral content. The unit is also marked by an increase in infaunal activity, evidenced by the intensity of bioturbation, together with an intensification of color banding (see **"Description of Lithostratigraphic Units,"** p. 8 in "Lithostratigraphy"). These observations suggest that the loss of the magnetic susceptibility signal may have been caused by biogeochemical dissolution of magnetic minerals rather than by dilution through increased sedimentation.

There is no marked change in the density of the sediments between Subunits IA and IB, and this agrees with the sedimentary observations. Velocity and density increase, reaching maximum values adjacent to the bottom of the subunit at ~160 mbsf. The density data are, in general, less noisy than the *P*-wave velocity data. Up to four cycles with a regular spatial frequency of ~40 m are present in the former. As expected, porosity steadily declines with depth but only until the base of Subunit IB. Thermal conductivity generally increases from the surface to the base of Subunit IB.

The boundary between Subunits IB and IC (200 mbsf) is most clearly marked by the return of a magnetic susceptibility signature. *P*-wave velocity peaks at ~150 mbsf in the midpart of Subunit IB and then declines to a low that corresponds to the transition between Subunits IB and IC. This boundary also corresponds to an abrupt decrease in bulk density, which is the start of a continuous decline in this parameter until near the base of Subunit IC.

Subunit IC (200–270 mbsf) has a significant magnetic susceptibility signature. It is also characterized by a porosity increase and density decrease. Thermal conductivity steadily declines until the base of Subunit IC, where the minimum downhole value of 0.769 W/(m·K) was recorded. Subunit IC is characterized by trends in physical properties that deviate from a simple variance with depth relationship. Together, the physical properties indicate a higher than expected water content within Subunit IC. There is no obvious compositional variation in the sediment to explain this. Sediment descriptions indicate that the only differences between Subunits IB and IC are a progressive increase in the diatom content with depth in Subunit IC, together with an absence of the bioturbation that typified Subunit IB. The comparatively low average grain density for Subunit IC can be explained by the higher proportion of opal-A ($SiO_2 \cdot nH_2O$; grain density = 1.890 g/m^3) compared with calcite (grain density = 2.710 g/m^3) in this subunit.

Compositional data indicate that the Subunit IC/ID boundary (270 mbsf) is the horizon at which diagenetic restructuring of biogenic silica starts (see **"Description of Lithostratigraphic Units,"** p. 8, in "Lithostratigraphy"). Magnetic susceptibility is low to absent across Subunit ID (270–300 mbsf), and the reason for this is not clear. The sediments are not as intensely bioturbated as those in Subunit IB, but the green and orange/purple banding is present and the sedimentation and or-

ganic carbon accumulation rates are relatively low, as they were during the succeeding deposition of Subunit IC, suggesting dissolution is again more likely than dilution as the mechanism. Other physical parameters such as bulk density, porosity, and *P*-wave velocity return to the trends across this layer expected with burial.

Subunit IE (300–305 mbsf) consists of nannofossil ooze/chalk across which a relatively low magnetic susceptibility signal is present. *P*-wave velocities from the velocimeter are highly variable but generally increase with depth. Both GRA and bulk density are lower in this subunit than in the overlying sediment, but the data are highly variable, as are the porosity data.

DOWNHOLE TOOLS

Five types of downhole tools were employed at Site 1225. These were the Adara temperature shoe, the DVTP, the DVTP-P, the APC-M tool, and the PCS. Deployments of the first four tools are described in the following subsections; deployments of the PCS are discussed in **Dickens et al.** (this volume).

In Situ Temperature Measurements

Six reliable determinations of downhole temperatures were made at depths between 0 and 303 mbsf in Hole 1225A using the Adara APC temperature tool or the DVTP (Table **T8**). As described in **"Downhole Tools,"** p. 49, in the "Explanatory Notes" chapter, in situ temperatures were estimated by extrapolation of the station data using thermal conductivities measured on adjacent cores to correct for the frictional heating on penetration. The 95% confidence intervals from the temperature fits are all <0.03°C. Testing of the probe tip thermistor on DVTP tool 2 showed that it read 0.38°C too high in the laboratory at ~19°C. Therefore, the temperature reading for 303.7 mbsf was adjusted down by 0.38°C. This changed the computed gradient by <0.1°C/km. The estimated in situ temperatures from both the Adara and DVTP define a gradient of 0.0174°C/m over the upper 303 m of sediment (Fig. **F31**). Extrapolating this temperature gradient yields a value of 6.97°C at the base of the hole. Multiplying the gradient by an average thermal conductivity of 0.89 W/(m·K) (see Fig. **F29A** and accompanying text in **"Thermal Conductivity,"** p. 28, in "Physical Properties") yields a conductive heat flow estimate of 15.5 mW/m² at Site 1225. This value lies near the low end of global heat flow database values for this area (Pollock et al., 1993). The temperature data define a profile that is curved slightly downward compared to a linear profile. Possible interpretations of the observed curvature are discussed under **"Thermal Conductivity,"** p. 28, in "Physical Properties."

T8. Downhole temperature measurements, p. 85.

F31. Temperature vs. depth, p. 70.

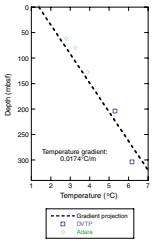

Other Tools

The APC-M tool was deployed in Hole 1225A continuously from Cores 201-1225A-5H through 14H. The recovered data from this run showed that the tool and data logger initially functioned correctly. Part way through the run after Core 201-1225A-8H, the data logger stopped recording. Upon recovery, the failure was attributed to a loose battery connection. The data from the APC-M tool will be analyzed postcruise.

The DVTP-P was deployed unsuccessfully twice in Hole 1225A at depths of 205.3 and 302.2 mbsf. The recorded data indicated that during both runs the nonindurated, fine-grained formation sediments clogged the filter. During the second run, there was a pressure drop to roughly atmospheric level during penetration. This failure was attributed to a leak in the line connecting the pressure transducer to the probe tip.

DOWNHOLE LOGGING

Operations

One logging run was made at Site 1225 with the triple combo tool string (see **"Downhole Logging,"** p. 53, in the "Explanatory Notes" chapter). After the last core was recovered at 1930 hr on 10 February, the hole was conditioned for logging. It was swept with 20 bbl of sepiolite mud; a wiper trip determined that there was 2 m of fill at the bottom of the hole. The hole was then displaced with 130 bbl of sepiolite, and the bottom of the drill string was positioned at 80 mbsf. Logging rig-up started at 0030 hr on 11 February. The 35-m-long logging string started downhole at 0300 hr, and two passes were made without difficulty, both times reaching the bottom of the hole at the wireline depth 323 mbsf. Logging operations and rig-down were completed by 1045 hr on 11 February (see Table **T9** for a complete summary of the operations).

T9. Detail of logging operations, p. 86.

Data Quality

The caliper log (Fig. **F32A**) shows that the borehole diameter was generally large and irregular. However, except in a few intervals (above 103 mbsf and from 200 to 230 mbsf), the caliper arm remained in good contact with the formation, suggesting that the data are of good quality. Even in the interval with poor contact, the density and porosity data, which are the most dependent on borehole wall contact, do not seem to have been significantly affected. Both logs agree very well for most of the logged section with the MAD measurements made on cores (shown as discrete circles in Figs. **F32E** and **F32F**). The only significant excursion in the density log that could be attributed to borehole effect is present between 100 and 103 mbsf. The lower density values in this interval were not observed in the cores. Above 100 mbsf, the density log is again in agreement with the MAD measurements. The porosity log seems more affected by the enlarged hole above 100 mbsf. Above this depth, both porosity logs (near- and far-source/receiver spacing) have values higher than the core measurements. The near-array porosity reading is the highest because the shorter distance between the neutron source and the receiver makes it more sensitive to borehole enlargements (see **"Downhole Logging,"** p. 53, in the "Explanatory Notes" chapter). The far-array porosity is less affected, but its significant differences from core measurements suggest that it is unreliable above 90 mbsf. Below 100 mbsf, both porosity logs are in good agreement with the MAD measurements. As neutrons penetrate deeper into the nondisturbed formation to reach the far receiver, the far porosity readings are generally slightly lower than the near porosity.

F32. Main logs recorded in Hole 1225A, p. 71.

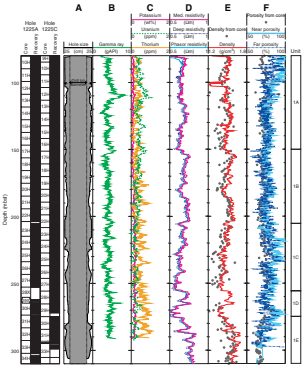

Comparison with Hole 851B Logs

Figure F33 compares the logs from Hole 1225A (solid red line) with the data recorded in Hole 851B during Leg 138 (green dashed line). The comparison between the two calipers in Figure F33A shows that hole conditions were better in Hole 851B. However, Figure F33G shows that, despite the different hole qualities, the density logs are almost identical, confirming that except for the 100- to 103-mbsf interval, the density log in Hole 1225A did not suffer from the large borehole diameter. The few differences between the two density logs in the deeper part of the hole could indicate differences in stratigraphic thickness between the two sites. When comparing the two curves, one can note that similar features between the two logs have a larger vertical extent in Hole 851B. This apparent greater thickness of the deeper sequences might be a result of the tool sticking to the borehole wall and of the wireline stretching. It might also indicate a higher sedimentation rate at Site 851 in the early stages of sediment deposition on the oceanic crust. The differences in sequence thickness between the two sites are also apparent in the two resistivity logs in Figure F33F, which are almost identical above 230 mbsf.

The main differences between the two data sets are in the gamma ray log and in the element concentrations derived from this log. In particular, the thorium concentration in Figure F33C seems to increase with depth in Hole 1225A, whereas it was uniformly very low in Hole 851B. The differences cannot be attributed to the larger borehole diameter in Hole 1225A. If any effect was expected, the larger hole should induce decreased gamma ray counts, but gamma ray values are generally higher in Hole 1225A. The main reason for the differences lies in the different tools used and in the very low natural radioactivity of the calcareous ooze that constitutes the major component of the sediments at the two sites. Both tools (the Natural Gamma Tool [NGT] used during Leg 138 and the Hostile Environment Gamma Ray Sonde (HNGS) used in Hole 1225A, see "Downhole Logging," p. 53, in the "Explanatory Notes" chapter) operate here in the lower range of their sensitivity. Because the HNGS was developed more recently and employs a larger and improved scintillation detector than the NGT, the readings in Hole 1225A should be more accurate. Consequently, the downhole increase in thorium detected at Site 1225 should be real, although it could not be detected during Leg 138.

Logging Stratigraphy

The sediments at Site 1225 can be generally described by low natural radioactivity and physical attributes (density and resistivity) typical of high porosity. Both porosity logs and MAD measurements show that the porosity is consistently at ~70%, explaining the generally low density and resistivity. The low gamma ray values are typical of the calcareous sediments present at Site 1225. Because of the fairly uniform lithology indicated by consistently low gamma ray values, our characterization of the formation from the logs is based on the physical measurements that show the clearest distinction, specifically the resistivity and the density. Because of the limited variations in all data, we consider that the sediments penetrated by Hole 1225A correspond to only one logging unit; however, minor covariation differences allow us to distinguish five subunits (see Fig. F32).

F33. Log comparison between Holes 1225A and 851B, p. 72.

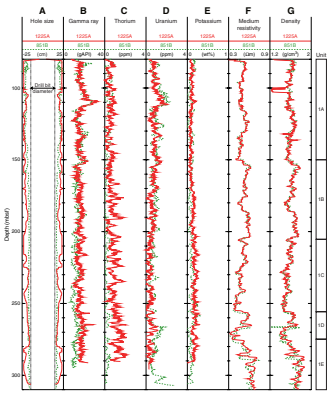

Logging Subunit 1A (80–150 mbsf) is characterized by generally higher gamma ray and uranium readings and by lower resistivity and density than the underlying sediments.

Logging Subunit 1B (150–205 mbsf) displays generally higher resistivity and density values than the surrounding formations. Its top and bottom are defined, respectively, by a sharp increase in resistivity and density at 150 mbsf and by a similar decrease at 205 mbsf. The bottom of this subunit corresponds to the bottom of lithostratigraphic Subunit IB, which is characterized by an increase in diatom ooze (see **"Description of Lithostratigraphic Units,"** p. 8, in "Lithostratigraphy").

In logging Subunit 1C (205–255 mbsf), resistivity and density decrease steadily with depth, whereas logging Subunit 1D (255–272 mbsf) consists of a distinct ~20-m-thick layer with higher resistivity and density indicative of a more cohesive and possibly more lithified unit. Core description showed that logging Subunit 1D has a higher proportion of nannofossil ooze to diatom ooze in Core 201-1225A-29P and Cores 201-1225C-28H and 29H. Core recovery in both Holes 1225A and 1225C was also slightly lower over this interval, which is consistent with a higher induration.

The top of logging Subunit 1E at 272 mbsf coincides with the top of lithostratigraphic Subunit ID, which is defined by an increase in diatoms (See **"Description of Lithostratigraphic Units,"** p. 8, in "Lithostratigraphy"). This subunit is characterized by a steady increase in resistivity and density, with the highest values in Hole 1225A recorded below 285 mbsf.

Temperature Log

Temperatures were recorded with the Lamont-Doherty Earth Observatory (LDEO) Temperature/Acceleration/Pressure (TAP) memory tool attached at the bottom of the triple combo string (Fig. **F34**). Because only a few hours had passed since the end of drilling operations and hole conditioning, the borehole temperature is not representative of the actual equilibrium temperature distribution of the formation. In the case of Hole 1225A, the warm (~25°C) surface seawater used during drilling generated borehole fluid temperatures higher than the formation temperatures. Discrete measurements made with the DVTP indicate a maximum formation temperature of 6.56°C at 320 mbsf (see **"In Situ Temperature Measurements,"** p. 31, in "Downhole Tools"), whereas the maximum temperature recorded by the TAP tool at the same depth is 7.90°C. Temperature variations in this record could, in principle, indicate possible fluid conduits intersected by the borehole. However, despite its coincidence with a relatively lower resistivity interval at ~180 mbsf, the ~1°C temperature increase at this depth is more likely the result of an incomplete "hole displacement" during hole conditioning before logging. Based on the bit diameter size, 130 bbl of mud was used to stabilize the hole for logging. Because of the enlarged hole conditions, with an average diameter of 42 cm, this volume filled only the deepest ~140 m of the hole. The observed temperature increase at ~180 mbsf is likely the result of the denser and warmer drilling mud cooling more slowly than the overlying borehole seawater. Because the temperature sensor is in an open compartment located at the bottom of the 35-m-long tool string, it is in the turbulence following the tool string on its way up. As a result, the temperature profiles recorded while logging uphole are almost uniform, as the string carried some of the downhole fluid and heat in its wake. By the time of the second pass

F34. Hole 1225A temperature log, p. 73.

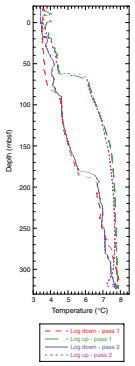

down an hour later, the borehole fluids had recovered their gravitational equilibrium and the temperature increase at 180 mbsf is apparent again.

REFERENCES

Baker, P.A., Stout, P.M., Kastner, M., and Elderfield, H., 1991. Large-scale lateral advection of seawater through oceanic crust in the central equatorial Pacific. *Earth Planet. Sci. Lett.,* 105:522–533.

Berggren, W.A., Hilgen, F.S. Langereis, C.G., Kent, D.V., Obradovich, J.C., Raffi, I., Rayun, M.E., and Shakleton, N.J., 1995a. *Late Neogene Chronology: new perspectives in high-resolution stratigraphy.* GSAB, 107:1272–1287.

Berggren, W.A., Kent, D.V., Swisher, C.C., and Aubry, M.P., 1995b. A revised Cenozoic geochronology and chronostratigraphy. *In* Berggren, W.A., Kent, D.V., Aubry, M.P., and Hardenbol, J., (Eds.), *Geochronology, Time Scales and Global Stratigraphic Correlation*. Spec. Pub.— SEPM 59:129–212.

Cragg, B.A., and Kemp, A.E.S., 1995. Bacterial profiles in deep sediment layers from the eastern equatorial Pacific Ocean, Site 851. *In* Pisias, N.G., Mayer, L.A., Janecek, T.R., Palmer-Julson, A., and van Andel, T.H. (Eds.), *Proc. ODP, Sci. Results,* 138: College Station, TX (Ocean Drilling Program), 599–604.

D'Hondt, S., Rutherford, S., and Spivack., A.J., 2002. Metabolic activity of the subsurface biosphere in deep-sea sediments. *Science,* 295:2067–2070.

Dickens, G.R., and Owen, R.M., 1999. The latest Miocene–early Pliocene biogenic bloom: a revised Indian Ocean perspective, *Mar. Geol.,* 161:75–91.

Farrell, J.W., Raffi, I., Janecek, T.C., Murray, D.W., Levitan, M., Dadey, K.A., Emeis, K.-C., Lyle, M., Flores, J.-A., and Hovan, S., 1995. Late Neogene sedimentation patterns in the eastern equatorial Pacific. *In* Pisias, N.G., Mayer, L.A., Janecek, T.R., Palmer-Julson, A., and van Andel, T.H. (Eds.), *Proc. ODP, Sci. Results,* 138: College Station, TX (Ocean Drilling Program), 717–756.

Hoehler, T.M., Alperin, M.J., Albert, D.B., and Martens, C.S., 1998. Thermodynamic control on hydrogen concentrations in anoxic sediments. *Geochim. Cosmochim. Acta,* 62:1745–1756.

————, 2001. Apparent minimum free energy requirements for methanogenic Archaea and sulfate-reducing bacteria in an anoxic marine sediment, *FEMS Microbio. Ecol.,* 38:33–41.

King, G.M., 1984. Utilization of hydrogen, acetate, and noncompetitive substrates by methanogenic bacteria in marine sediments, *Geomicrobiol. J.,* 3:275–306.

Levitus, S., Burgett, R., and Boyer, T., 1994. *World Ocean Atlas 1994* (Vol. 3): *Nutrients*. NOAA Atlas NESDIS 3, U.S. Department of Commerce Washington D.C.

Lovley, D.R., and Goodwin, S., 1988. Hydrogen concentrations as an indicator of the predominant terminal electron-accepting reactions in aquatic sediments, *Geochim. Cosmochim. Acta,* 52:2993–3003.

Mayer, L., Pisias, N., Janecek, T., et al., 1992. *Proc. ODP, Init. Repts.,* 138 (Pt. 1): College Station, TX (Ocean Drilling Program).

McDuff, R.E., 1985. The chemistry of interstitial waters, Deep Sea Drilling Project Leg 86. *In* Heath, G.R., Burckle, L.H., et al., *Init. Repts. DSDP,* 86: Washington (U.S. Govt. Printing Office), 675–687.

Murray, R.W., Miller, D.J., and Kryc, K.A., 2000. Analysis of major and trace elements in rocks, sediments, and interstitial waters by inductively coupled plasma–atomic emission spectrometry (ICP-AES). *ODP Tech. Note,* 29 [Online]. Available from World Wide Web: <http://www-odp.tamu.edu/publications/tnotes/tn29/INDEX.HTM>. [Cited 2002-01-23]

Oremland, R.S., Marsh, L.M., and Polcin, S., 1982. Methane production and simultaneous sulfate reduction in anoxic salt marsh sediments. *Nature,* 296:143–145.

Oremland, R.S., and Polcin, S., 1982. Methanogenesis and sulfate reduction: competitive and noncompetitive substrates in estuarine sediments. *Appl. Environ. Microbiol.,* 44:1270–1276.

Oyun, S., Elderfield, H., and Klinkhammer, G.P., 1995. Strontium isotopes in pore waters of east equatorial Pacific sediments: indicators of seawater advection

through oceanic crust and sediments. *In* Pisias, N.G., Mayer, L.A., Janecek, T.R., Palmer-Julson, A., and van Andel, T.H. (Eds.), *Proc. ODP, Sci. Results,* 138: College Station, TX (Ocean Drilling Program), 813–819.

Parkes, R.J., Cragg, B.A., Bale, S.J., Getliff, J.M.,Goodman, K., Rochelle, P.A., Fry, J.C., Weightman, A.J., and Harvey, S.M., 1994. A deep bacterial biosphere in Pacific Ocean sediments. *Nature,* 371:410–413.

Pisias, N.G., Mayer, L.A., Janecek, T.R., Palmer-Julson, A., and van Andel, T.H. (Eds.), 1995. *Proc. ODP, Sci Results,* 138: College Station, TX (Ocean Drilling Program).

Pollack, H.N., Hurter, S.J., and Johnson, J.R., 1993. Heat flow from the Earth's interior: analysis of the global data set. *Rev. Geophysics,* 31:267–280.

Sclater, J.G., Crowe, J., and Anderson, R.N., 1976. On the reliability of ocean heat flow averages. *J. Geophys. Res.,* 81:2997–3006.

Shipboard Scientific Party, 1992. Site 851. *In* Mayer, L., Pisias, N., Janecek, T., et al., *Proc. ODP, Init. Repts.,* 138 (Pt. 2): College Station, TX (Ocean Drilling Program), 891–965.

————, 1993. Site 881. *In* Rea, D.K., Basov, I.A., Janecek, T.R., Palmer-Julson, A., et al., *Proc. ODP, Init. Repts.,* 145: College Station, TX (Ocean Drilling Program), 37–83.

————, 1997. Site 999. *In* Sigurdsson, H., Leckie, R.M., Acton, G.D., et al., *Proc. ODP, Init. Repts.,* 165: College Station, TX (Ocean Drilling Program), 131–230.

Smith, D.C., Spivack, A.J., Fisk, M.R., Haveman, S.A., Staudigel, H., and ODP Leg 185 Shipboard Scientific Party, 2000. Methods for quantifying potential microbial contamination during deep ocean coring. *ODP Tech. Note,* 28 [Online]. Available from the World Wide Web: <http://www-odp.tamu.edu/publications/tnotes/tn28/INDEX.HTM>. [2002-03-30]

Sørensen, J., Christensen, D., and Jørgensen, B.B., 1981. Volatile fatty acids and hydrogen as substrates for sulfate-reducing bacteria in anaerobic marine sediment. *Appl. Environ. Microbiol.,* 42:5–11.

Spivack, A.J., and You, C.F, 1997. Boron isotopic geochemistry of carbonates and pore waters, Ocean Drilling Program Site 851. *Earth Planet. Sci. Lett.,* 152:113–122.

van Andel, T.H., Heath, G.R., and Moore, T.C., Jr., 1975. Cenozoic history and paleoceanography of the central equatorial Pacific Ocean: a regional synthesis of Deep Sea Drilling Project data. *Mem.—Geol. Soc. Am.,* 143.

Von Herzen, R.P., and Uyeda, S., 1963. Heat flow through the Pacific Ocean floor. *J. Geophys. Res.,* 68:4219–4250.

Wellsbury, P., and Parkes, R.J., 1995. Acetate bioavailability and turnover in an estuarine sediment. *FEMS Microbiol. Ecol.,* 17:85–94.

Figure F1. Lithostratigraphic summary for Site 1225. a*/b* = green-red value/blue-yellow value, TD = total depth.

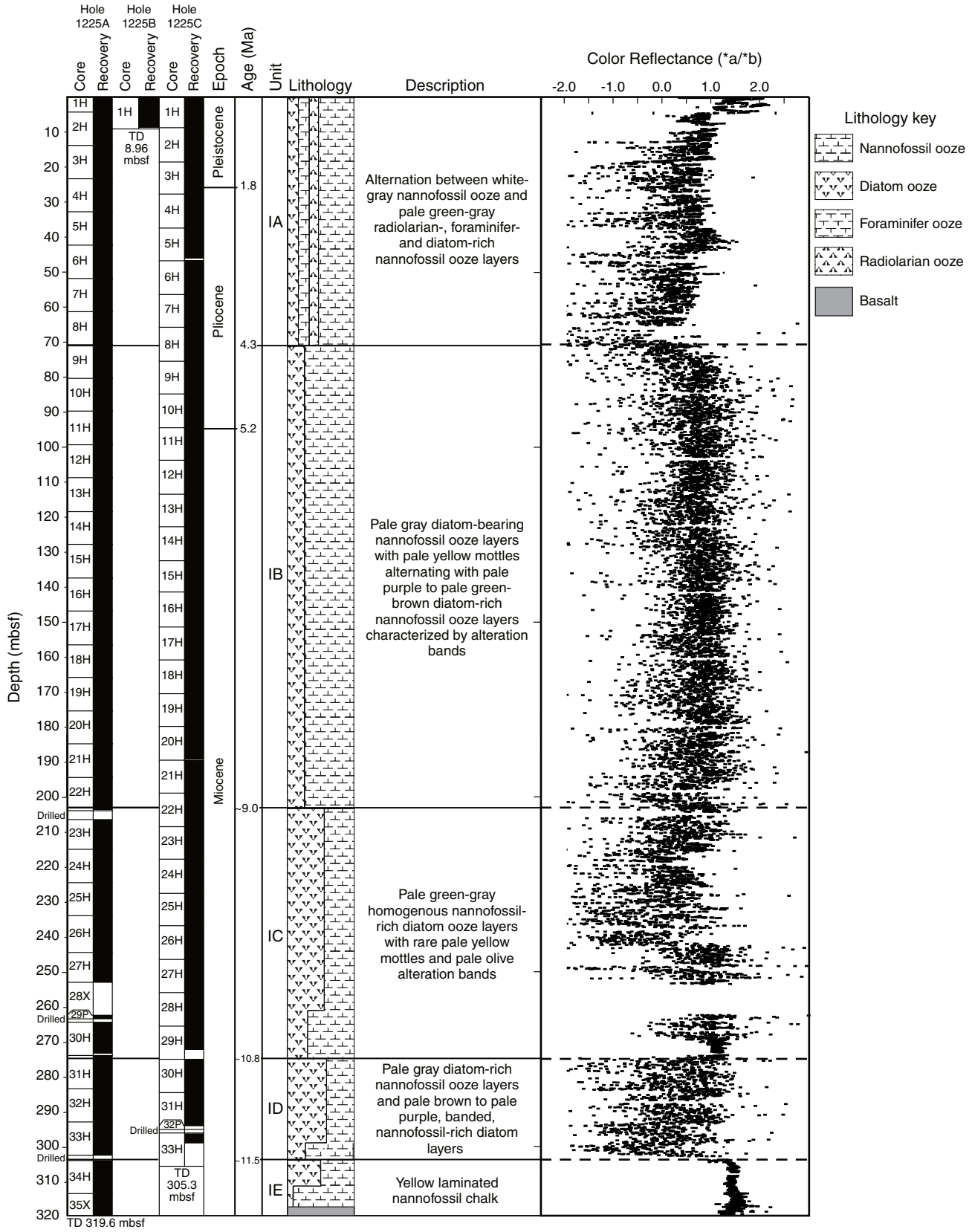

Figure F2. Examples of XRD analyses for Site 1225. For discussion see "Mineralogy," p. 11, in "Lithostratigraphy." TD = total depth.

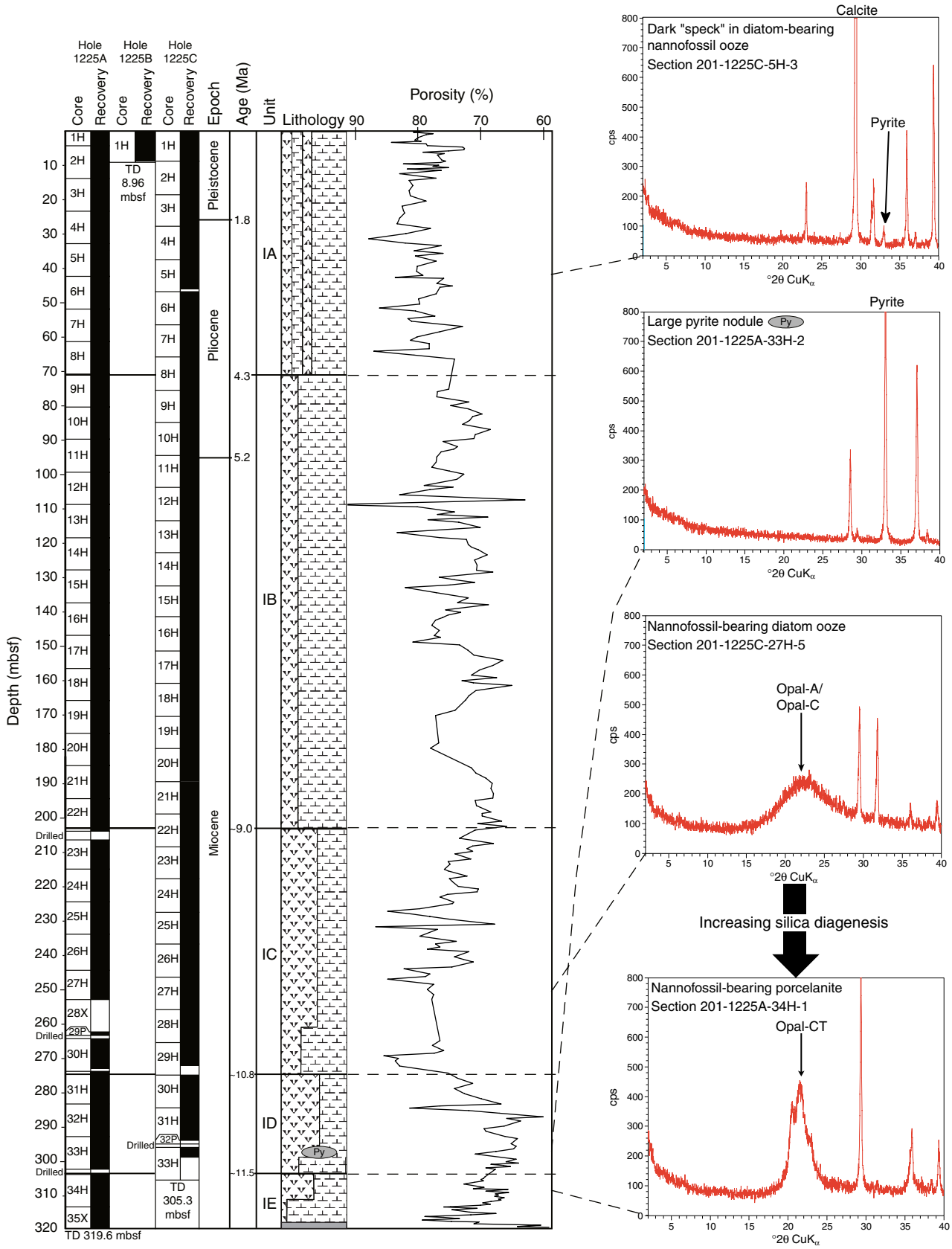

Figure F3. Intensity of bioturbation (the line is a moving average, 10 terms) and magnetic susceptibility at Site 1225. For explanation see **"Mineralogy,"** p. 11, in "Lithostratigraphy." TD = total depth.

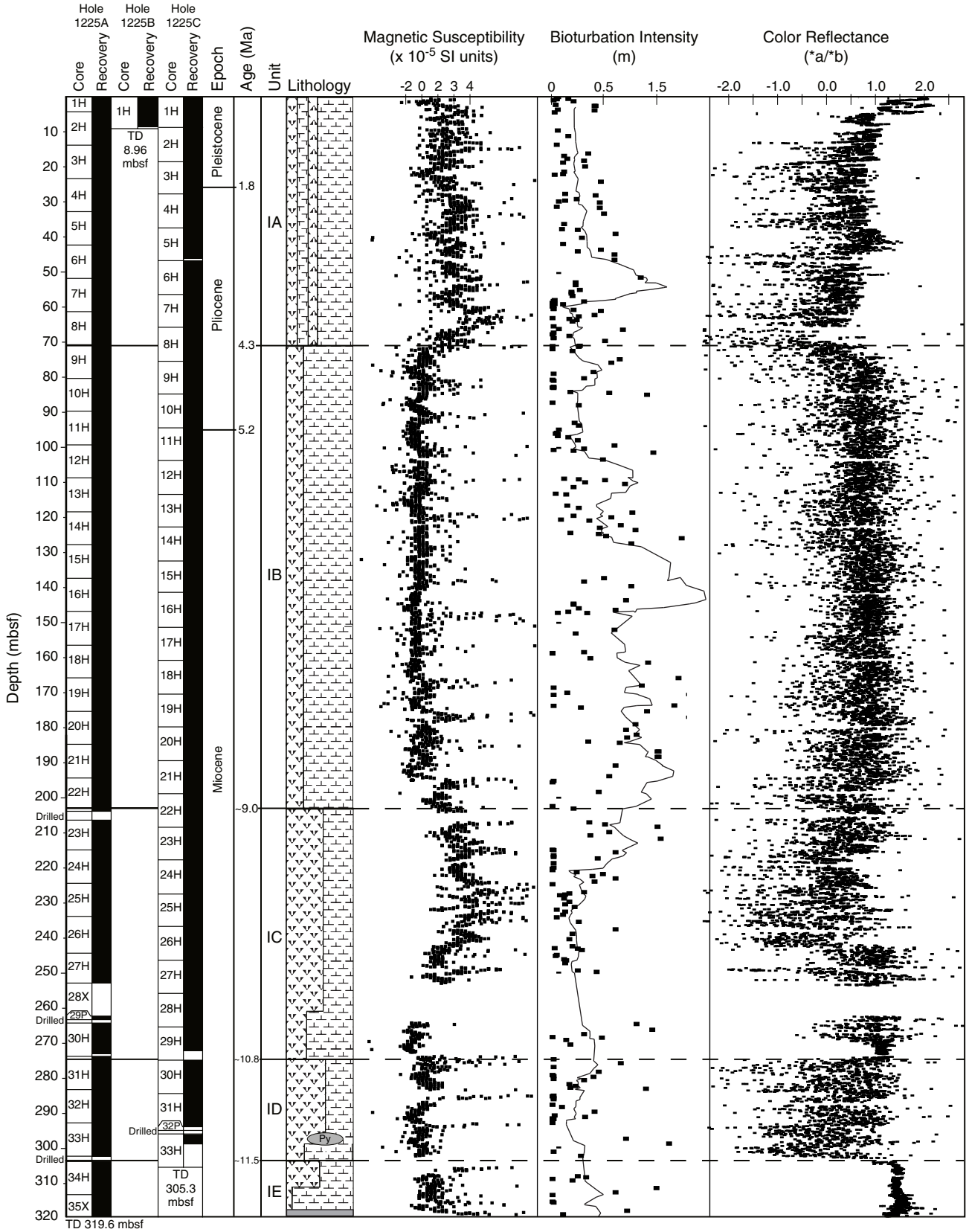

Figure F4. Color close-up photos. **A.** Alteration features in Subunit IB. Pale purple and green alteration banding is truncated by reaction halos around burrows. **B.** Concentric reaction halos around a burrow in Subunit IB. **C.** Laminated porcelanite nodule in Subunit IE. The presence of porcelanite indicates the onset of silica diagenesis (opal-A to opal-CT transition) in the lower part of the sedimentary section. (Continued on next page.)

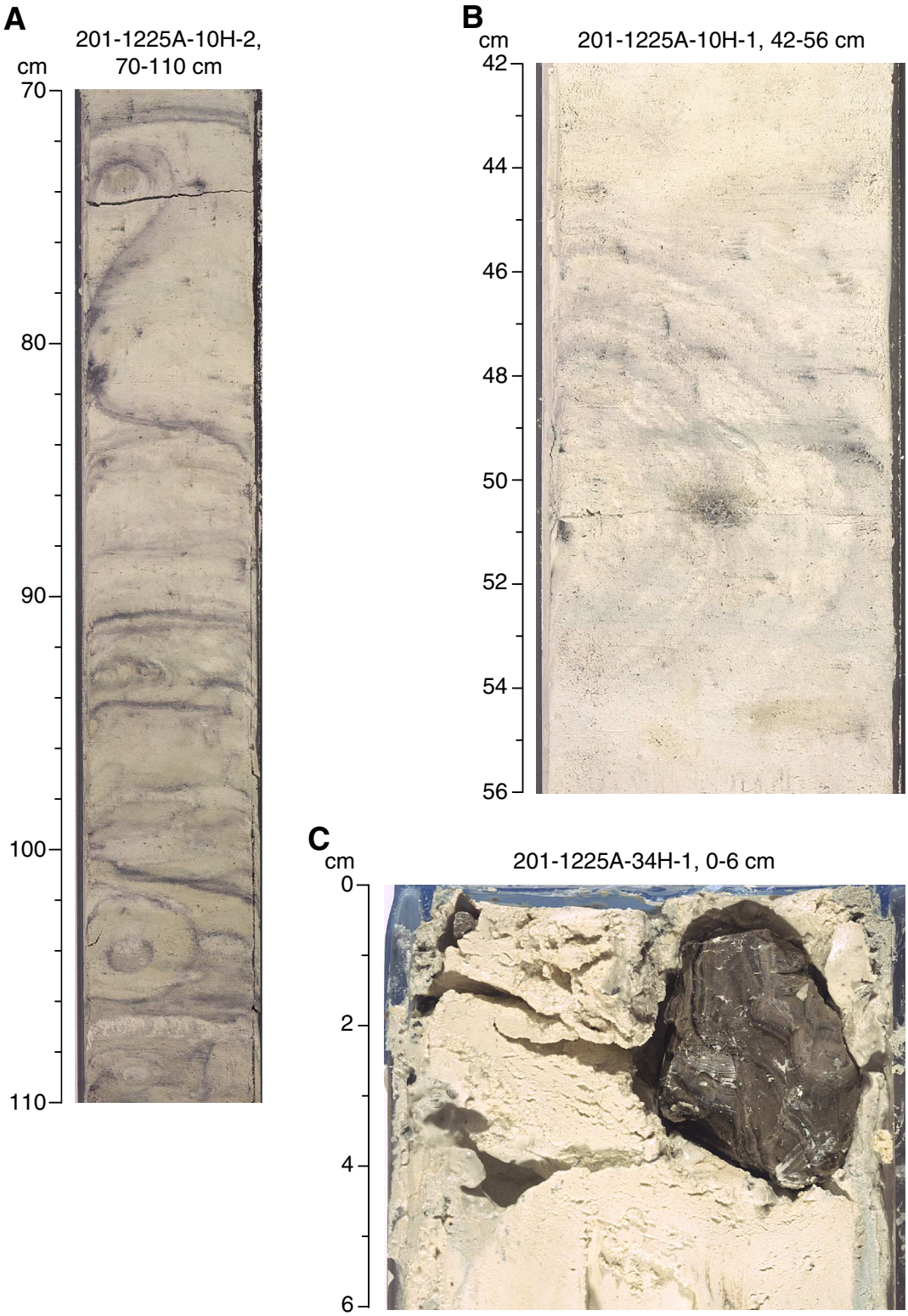

Figure F4 (continued). D. Volcanic glass shards in laminated chalk of Subunit IE. **E.** Laminated nannofossil chalk in Subunit IE. The yellowish color may be due to bleaching by oxygenated seawater flowing through the oceanic basement and lower interval of the sedimentary section. **F.** Dark pyrite spot in Subunit IA. These spots are present throughout the hole. **G.** Pyrite nodule. Pyrite nodules and pyritized burrows are present at several levels of Subunit IC.

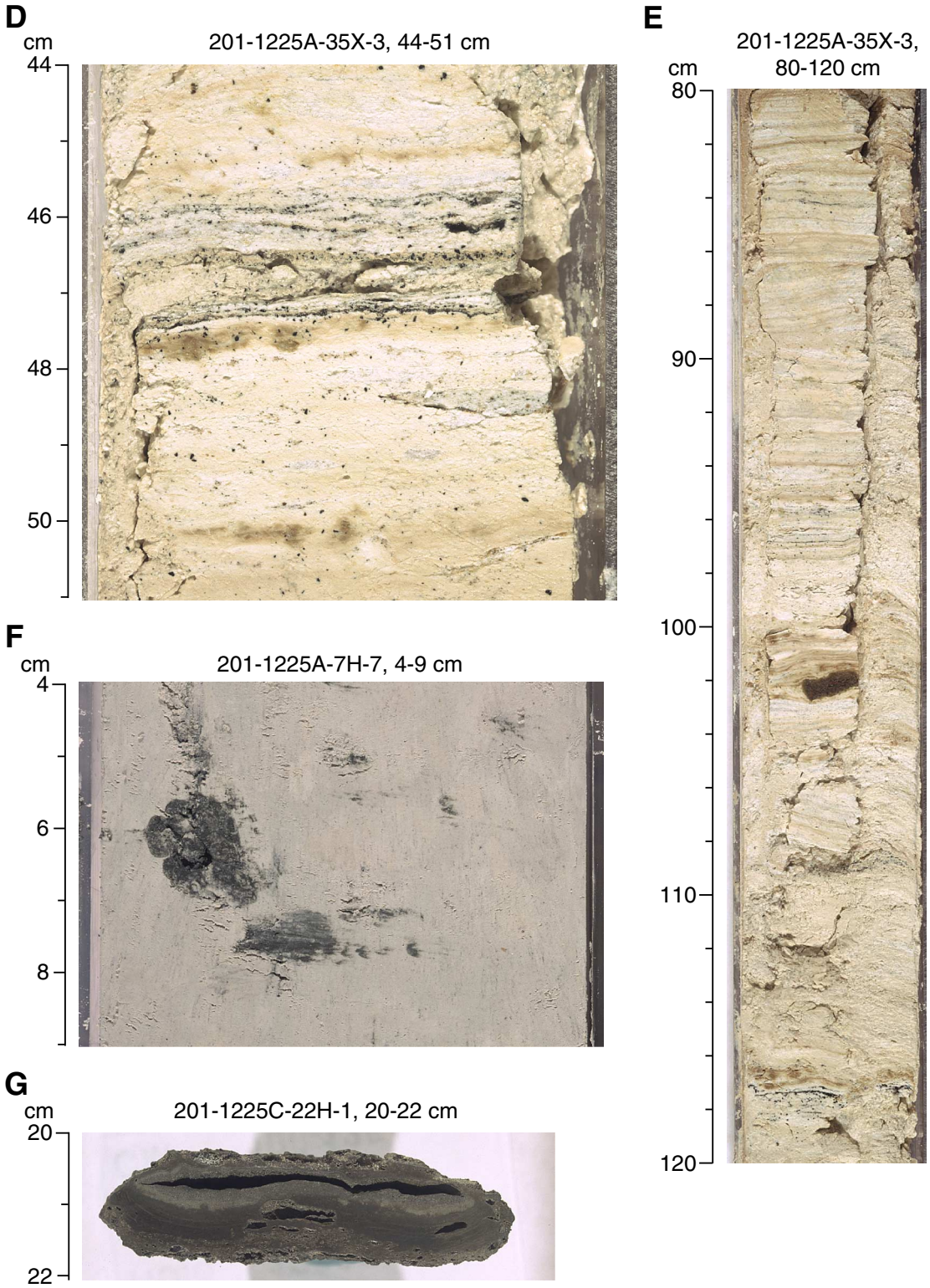

Figure F5. Concentrations of various dissolved species in interstitial waters from Holes 1225A and 1225C. (**A**) Alkalinity, (**B**) dissolved inorganic carbon (DIC), (**C**) nitrate, (**D**) manganese, (**E**) iron, (**F**) sulfate, and (**G**) strontium. (Continued on next page.)

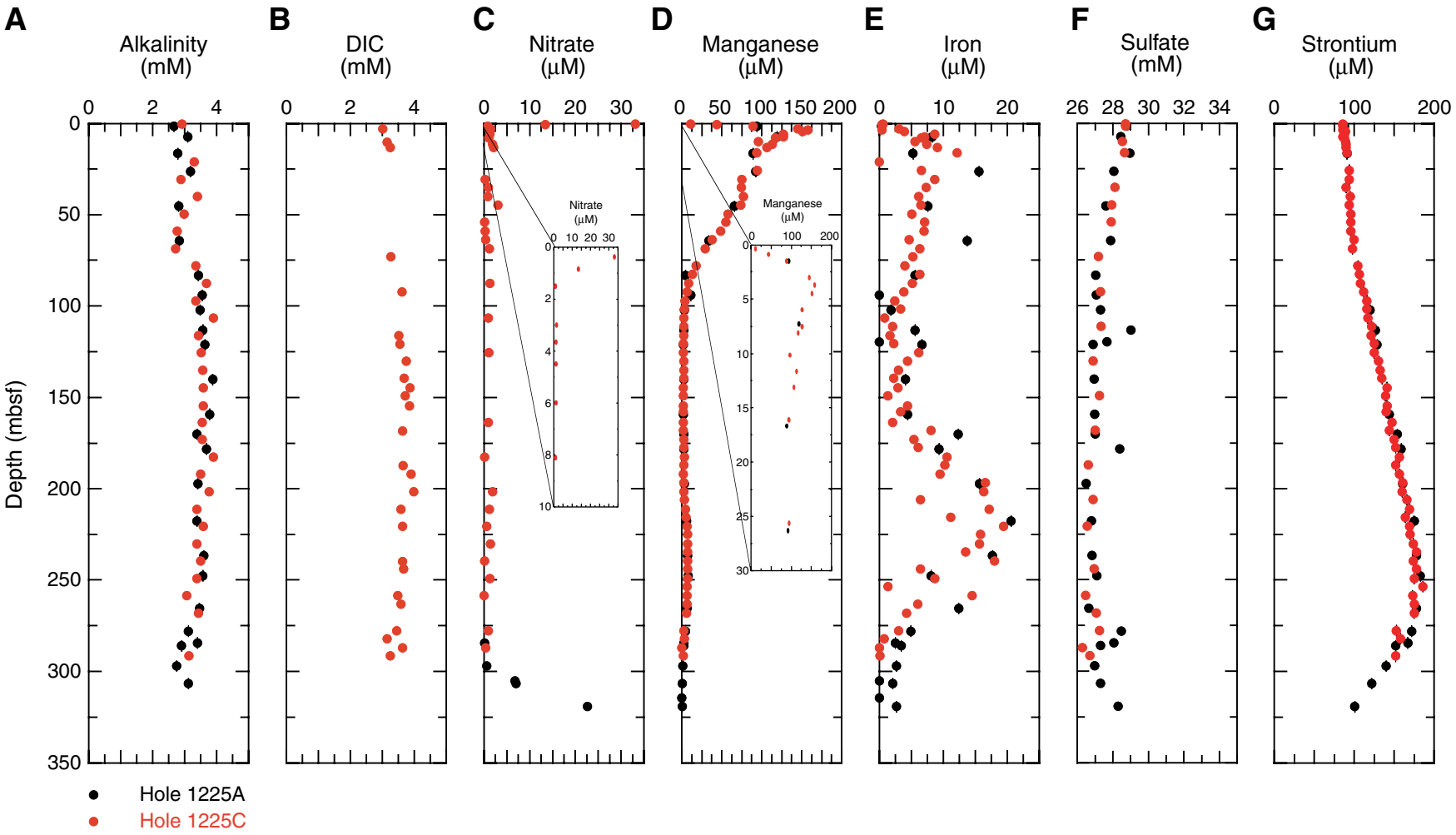

Figure F5 (continued). (H) total sulfide, (I) volatile fatty acids, (J) hydrogen, (K) ammonium, (L) phosphate, (M) silica, and (N) chloride.

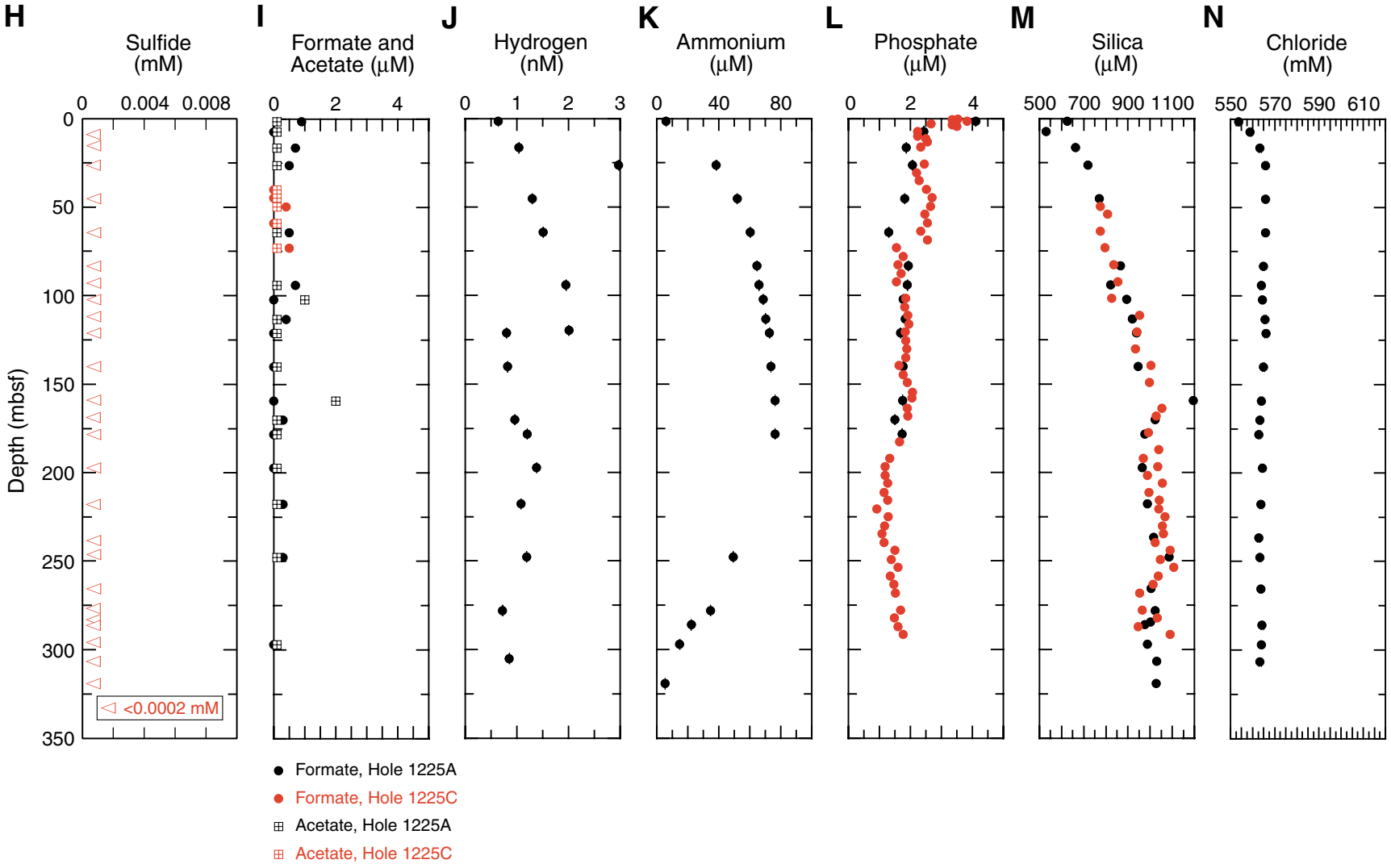

Figure F6. A. Methane concentration in Holes 1225A and 1225C obtained under different headspace incubation techniques. Only samples with a sediment volume of 3 mL are illustrated. The two vertical lines designate the mean values of replicate analyses of methane concentrations in ambient air on the catwalk (n = 5) and in the chemistry laboratory (n = 4); the shaded bars indicate the standard deviation of the respective measurements. For subsequent determination of concentrations of methane in interstitial waters, the value of 1.6 ppm was subtracted from the measured value. **B.** Methane concentrations in interstitial waters of Holes 1225A and 1225C. Porosity data are derived from GRA data (see "Density and Porosity," p. 27, in "Physical Properties"). Note that the systematically higher concentrations in Hole 1225C reflect the longer incubation time rather than differences in concentrations of the two adjacent holes.

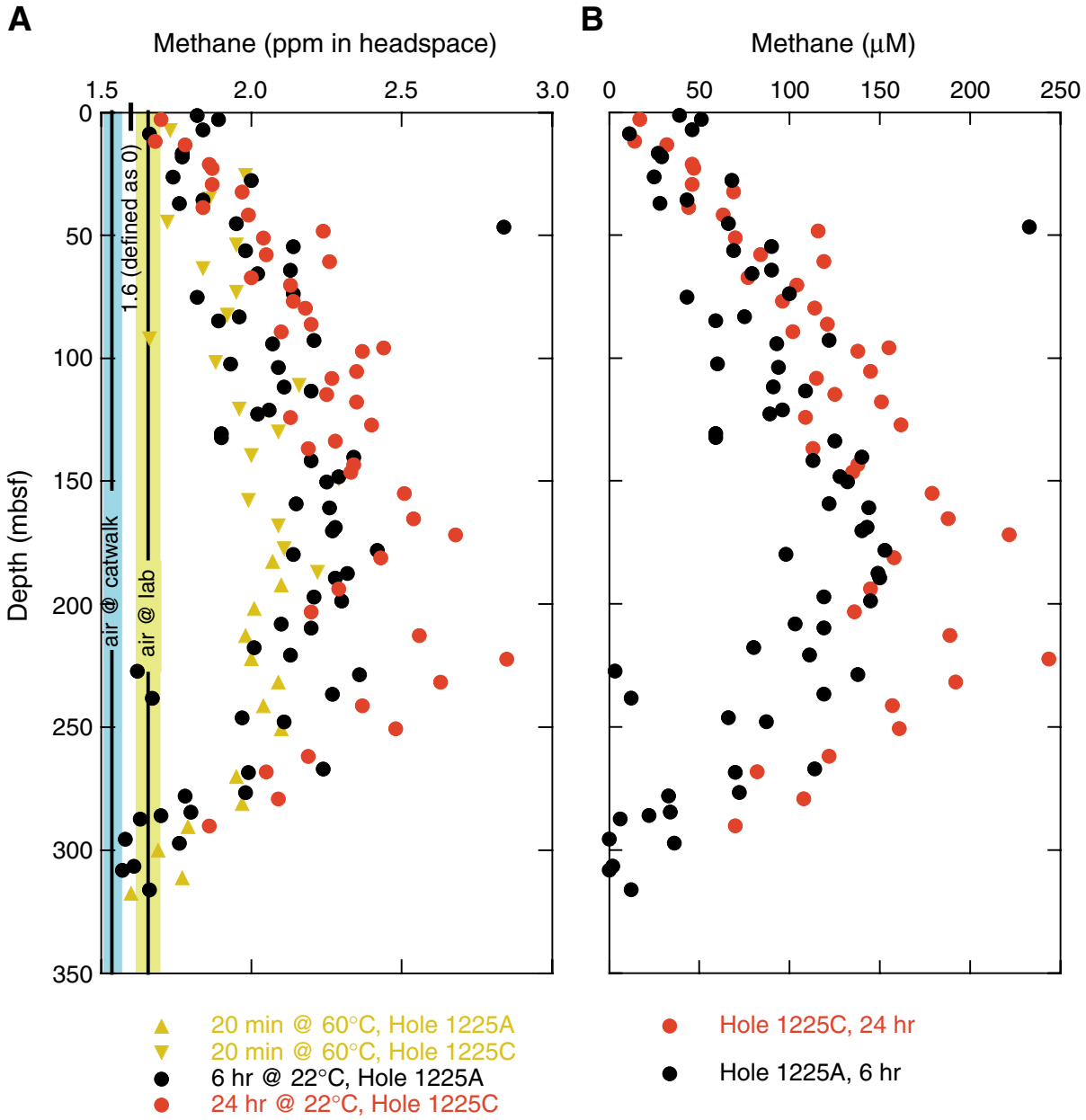

Figure F7. Calcium carbonate and organic carbon concentrations in sediments from Holes 1225A and 1225C.

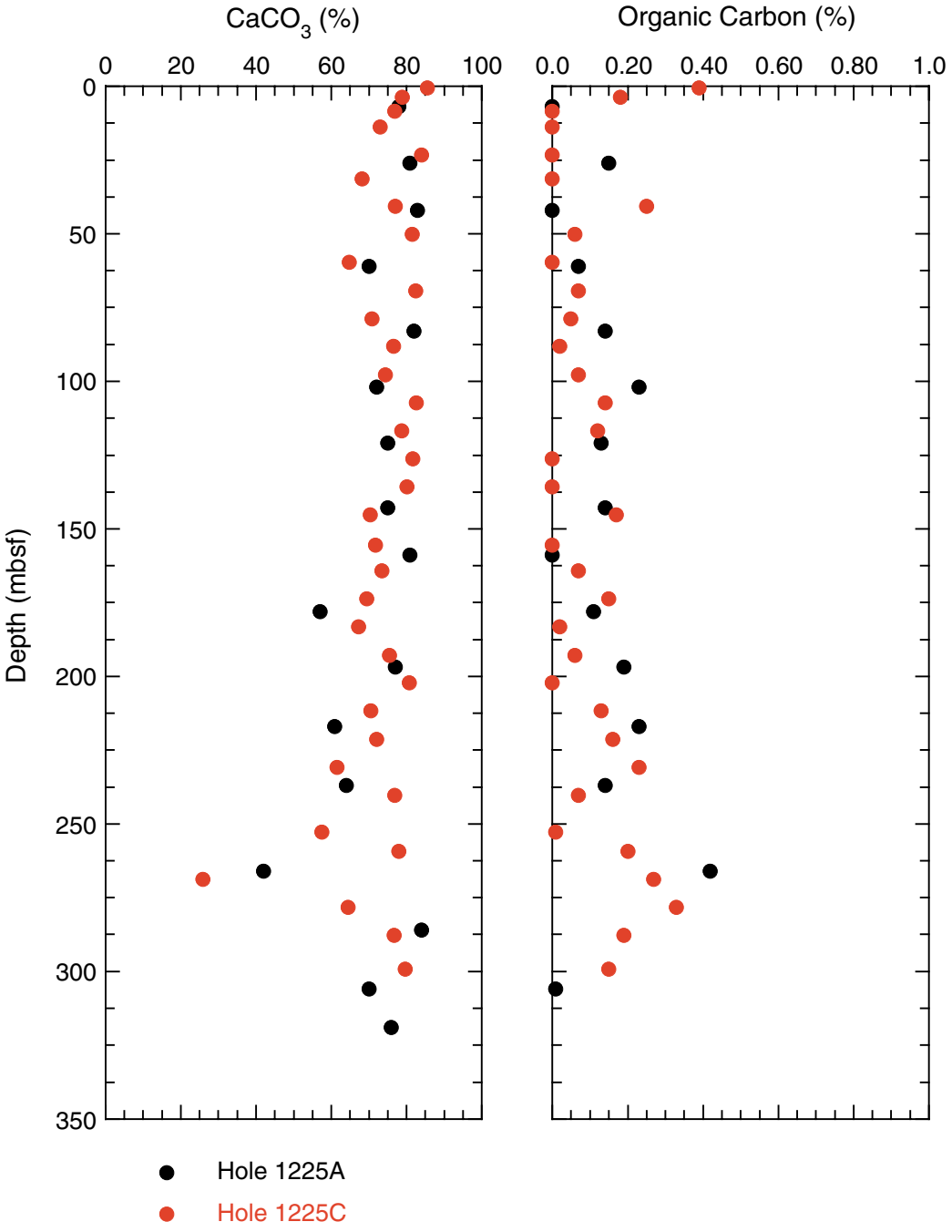

Figure F8. Graphical representation of subsampling and analysis program for the MBIO core sections from Hole 1225A. The sequence of subsections runs from the top of the core (right) toward the bottom (left). Cuts represented by dotted lines were cut in the nitrogen-flushed cutting rig. DNA = deoxyribonucleic acid, ATP = adenosine triphosphate. WRC = whole-round core. See Table T2, p. 82, in the "Explanatory Notes" chapter for explanation of sampling codes.

Hole 1225A		Fluorescent in situ hybridization (FISH)			Enrichments for thermophiles	General enrichment slurry		Activity measurements: methanogenesis, thymidine incorporation, tritiated hydrogen turnover, phosphate ^{33}O turnover					Sulfate reduction activity; hydrogen concentration; CNHS geochemistry; magnetic bacterial particles				Diffusion experiments	Cell separations	Fe/Mn/S solid-phase concentrations and stable isotopes	Biomarkers	DNA-ODP archive	DNA			ATP/DNA	Interstitial water	-----Top of Section -----
		N_2-flushed cutting rig															ODP cutter										
Interval (cm)		6			6	7	7	6			6		6				5	5	5	10	5	5	5	5	10	15	
Curators Code		FISHWR	FISHH	FISHTS	HTEW	SLUR		H3S	ABTP	O18B	ABTP	PO4B	SRRF	H2S	CHNSS	CHNSF	DIFFF	CELLS	FESF	BIOMHIN	DNAODP	DNAN	DNAS	DNAT	ATPS	IW	
Sample Type		Rem. WRC	1 Syr	2 Syr	6 Syr	20-mL syr	20-mL syr	4 Syr	4 Syr	1 Syr	8 Syr	1-cm slice	4 Syr	4 Syr	Plug/1-cm sl	Res/1-cm sl	WRC	WRC	WRC	WRC	WRC	WRC	WRC	WRC	WRC	WRC	
Package Type		Poly-bag	Anaer. Jar	Poly-bag	Anaer. Jar	Al-bag	Al-bag	Al-bag	Anaer. Jar	Poly-bag	Anaer. Jar	Poly-bag	Al-Bag	Poly-bag	Poly-bag	Al-bag	Al-bag	Poly-bag	Al-bag	Poly-bag	Poly-bag	Poly-bag	Poly-bag	Poly-bag	Poly-bag		
Package Atmosphere			N_2		N_2	N_2	N_2	N_2	N_2		N_2		N_2	N_2		Vac pack	Vac pack		Vac pack								
Temperature Destination		-80°	+4°C	+4°C	+4°C	on ice	on ice	+4°C Radvan	+4°C Radvan	+4°C	+4°C Radvan	-20°C	+4°C Radvan	+4°C	+4°C	+4°C	4°C	-80°C	-20°C	-80°C	-80°C	-80°C	-80°C	-80°C	-80°C	4°C	Sediment Depth (mbsf)
Core	Section																										top
2H	3	1	1	1	-	1	1	1	1	1	1	1	1	1	1	1	1	-	1	1	1	1	1	1	1	1	7.3
4H	3	1	1	1	-	-	-	1	1	1	1	1	1	1	1	1	-	-	1	1	1	1	1	1	1	1	26.3
6H	3	1	1	1	1	-	-	1	1	1	1	1	1	1	1	1	-	-	1	1	1	1	1	1	1	1	45.3
8H	3	1	1	1	-	-	-	-					1	1	1	1	-	-	1	1	1	1	1	1	1	1	64.3
10H	3	1	1	1	-	-	-	-					1	1	1	1	-	-	1	1	1	1	1	1	1	1	83.3
12H	3	1	1	1	-	1	1	1	1	1	1	1	1	1	1	1	1	-	1	1	1	1	1	1	1	1	102.3
14H	3	1	1	1	-	-	-	-					1	1	1	1	-	-	1	1	1	1	1	1	1	1	121.3
16H	3	1	1	1	-	-	-	-					1	1	1	1	-	-	1	1	1	1	1	1	1	1	140.3
18H	3	1	1	1	-	-	-	1	1	1	1	1	1	1	1	1	-	-	1	1	1	1	1	1	1	1	159.3
20H	3	1	1	1	-	-	-	-					1	1	1	1	-	-	1	1	1	1	1	1	1	1	178.3
22H	3	1	1	1	-	1	1	1	1	1	1	1	1	1	1	1	1	1	1	1	1	1	1	1	1	1	197.3
24H	3	1	1	1	-	-	-						1	1	1	1	-	-	1	1	1	1	1	1	1	1	217.8
26H	3	1	1	1	-	-	-	1	1	1	1	1	1	1	1	1	-	-	1	1	1	1	1	1	1	1	236.8
30H	3	1	1	1	-	-	-	-	-	-			1	1	1	1	-	-	1	1	1	1	1	1	1	1	267.1
32H	3	1	1	1	-	-	-	1	1	1	1	1	1	1	1	1	-	-	1	1	1	1	1	1	1	1	286.1
34H	3	1	1	1	-	1	1	1	1	1	1	1	1	1	1	1	-	-	1	1	1	1	1	1	1	1	306.7
35X	5			1	-	-	-	1	1	1	1	1	1	1	1	1	1	-	1	1	1	1	1	1	1	1	319.2
35X	CC	Special Hard Rock Protocol																									320.1
	TOTAL	16	16	17	1	4	4	10	10	10	10	10	17	17	17	17	4	1	17	17	17	17	17	17	17	17	

Figure F9. Graphical representation of subsampling and analysis program for the MBIO core sections from Hole 1225C. The sequence of subsectioning runs from the top of the core (right) toward the bottom (left). Cuts represented by dotted lines were cut in the nitrogen-flushed cutting rig. DNA = deoxyribonucleic acid, ATP = adenosine triphosphate. WRC = whole-round core. See Table T2, p. 82, in the "Explanatory Notes" chapter for explanation of sampling codes.

Hole 1225C		Fluorescent in situ hybridization (FISH)			Enrichments for thermophiles	Activity measurements: methanogenesis, thymidine incorporation, tritiated hydrogen turnover, ^{18}O phosphate turnover					Sulfate reduction activity; hydrogen concentration; ONHS geochemistry; magnetic bacterial particles				Diffusion experiments	Cell separations	Fe/Mn/S solid-phase concentrations and stable isotopes	Biomarkers	DNA-ODP archive	DNA				ATP/DNA	General enrichment slurry		Interstitial water	------Top of Section ------
		N_2-flushed cutting rig													ODP cutter														
Interval (cm)		6			6	6			6		6				5	5	5	10	5	5	5	5	10	7	7	15		
Curators Code		FISHWR	FISHH	FISHTS	HTEW	H3S	ABTP	O18B	ABTP	PO4B	SRRF	H2S	CHNSS	CHNSF	DIFFF	CELLS	FESF	BIOMHIN	DNAODP	DNAN	DNAS	DNAT	ATPS	SLUR		IW		
Sample Type		Rem. WRC	1 Syr	2 Syr	6 Syr	4 Syr	4 Syr	1 Syr	8 Syr	1-cm sl	4 Syr	4 Syr	Plug/1-cm sl	Res/1-cm sl	WRC	WRC	WRC	WRC	WRC	WRC	WRC	WRC	WRC	20-mL syr	20-mL syr	WRC		
Package Type		Poly-bag	Anaer. Jar	Poly-bag	Anaer. Jar	Al-bag	Anaer. Jar	Poly-bag	Anaer. Jar	Poly-bag	Al-Bag	Poly-bag	Poly-bag	Al-bag	Al-bag	Poly-bag	Al-bag	Poly-bag	Poly-bag	Poly-bag	Poly-bag	Poly-bag	Poly-bag	Al-bag	Al-bag			
Package Atmosphere			N_2		N_2	N_2	N_2		N_2		N_2	N_2		Vac pack	Vac pack		Vac pack							N_2	N_2			Sediment Depth (mbsf)
Temperature Destination		-80°	+4˚C	+4˚C	+4˚C	+4˚C Radvan	+4˚C Radvan	+4˚C	+4˚C Radvan	-20˚C	+4˚C Radvan	+4˚C	+4˚C	+4˚C	4˚C	-80˚C	-20˚C	-80˚C	-80˚C	-80˚C	-80˚C	-80˚C	-80˚C	on ice	on ice	4˚C		
Core	Section																											top
1H	1	1	1	1	-	1	1	1	1	1	1	1	1	1	-	-	1	1	1	1	1	1	1	1	1	1		0*
1H	3	1	1	1	-	-	1	1	1	1	1	-	1	1	-	1	1	1	1	1	1	1	1	-	-	1		3.0
1H	6	1	1	1	-	-	-	-	-	-	1	-	1	1	-	-	1	1	1	1	1	1	1	-	-	1		7.5
	TOTAL	3	3	3	0	1	2	2	2	2	3	1	3	3	0	1	3	3	3	3	3	3	3	1	1	3		

*sampling started at 37 cm depth

Figure F10. Total prokaryotic cells (solid circles) enumerated by AODC and the percentage of that population involved in cell division (open circles) with depth at Site 1225. Dividing cell percentages become increasingly unreliable as total cell counts decrease below 10^6/cm^3, since the total number of counted cells is then 20–30 and the dividing cells comprise only 5%–10% of this number. The empirical limit for cell counts (~4.7×10^4 cells/cm^3) is indicated; natural cell abundances under the detection limits are not quantifiable, and are listed here arbitrarily as 1×10^4 cells/cm^3.

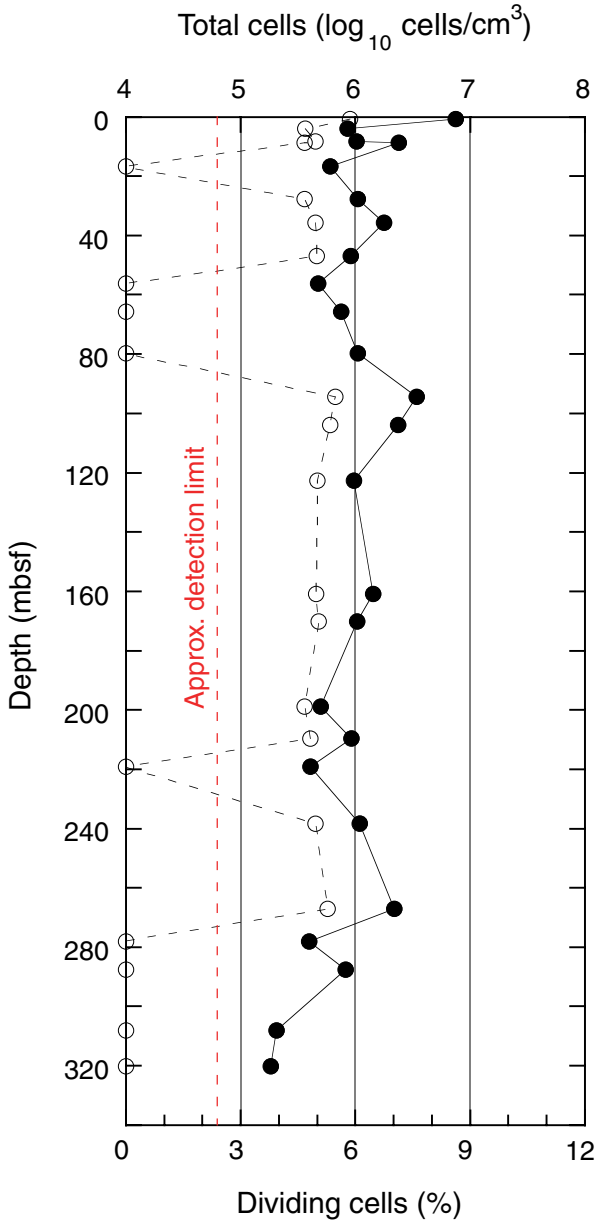

Figure F11. Profile of total prokaryote numbers in Hole 1225C (upper three data points) and Hole 1225A (rest of data points). Heavy dashed line is a model regression line derived from previous ODP legs and updated from Parkes et al., 1994 [$\log_{10}$ cells = 8.03 – 0.66 $\log_{10}$ depth (m)], the lighter dashed lines represent the ±2-σ envelope of cell concentrations at previously censused ODP sites.

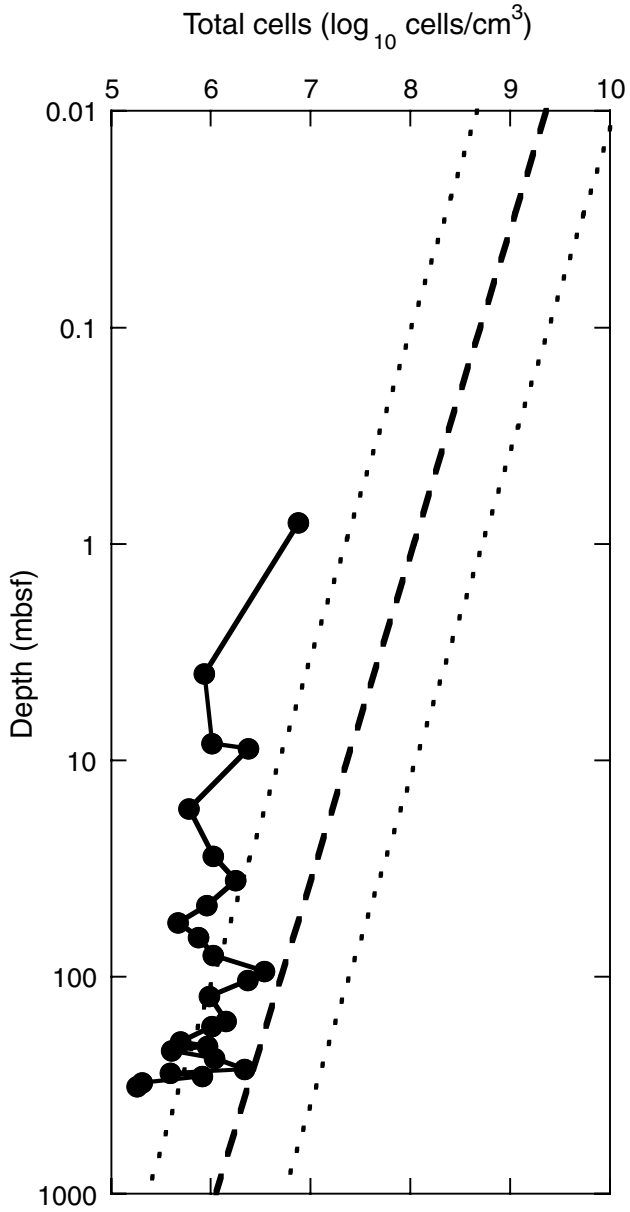

Figure F12. Piece of basalt from the bottom core of Hole 1225A trapped in the core catcher of an XCB core that had penetrated ~1 m into the basement rock (Sample 201-1225A-35X-CC, 25 cm). The rock was split and used for microbiology and other analyses. Scale bar = 2.5 cm.

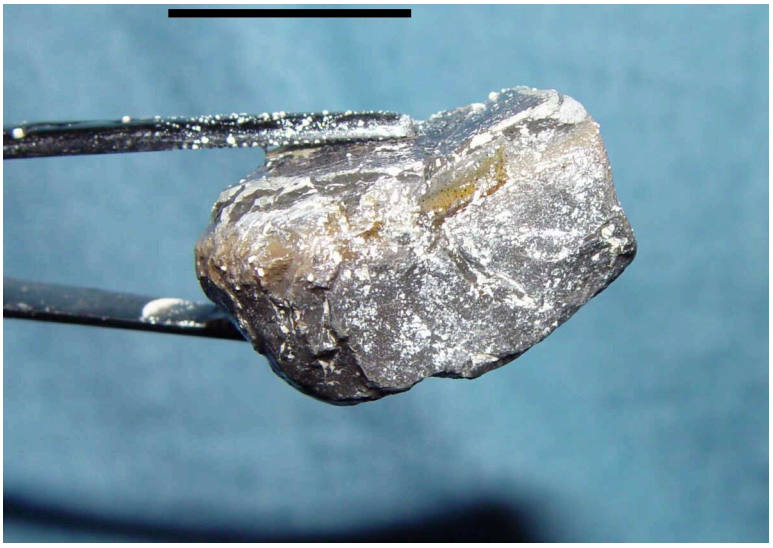

Figure F13. Comparison of temperature trends measured with the IR camera from the top to the bottom of cores. No consistent trend is apparent. Trend lines are estimated best-fit regressions drawn in by hand. Tops of cores are at tops of figures.

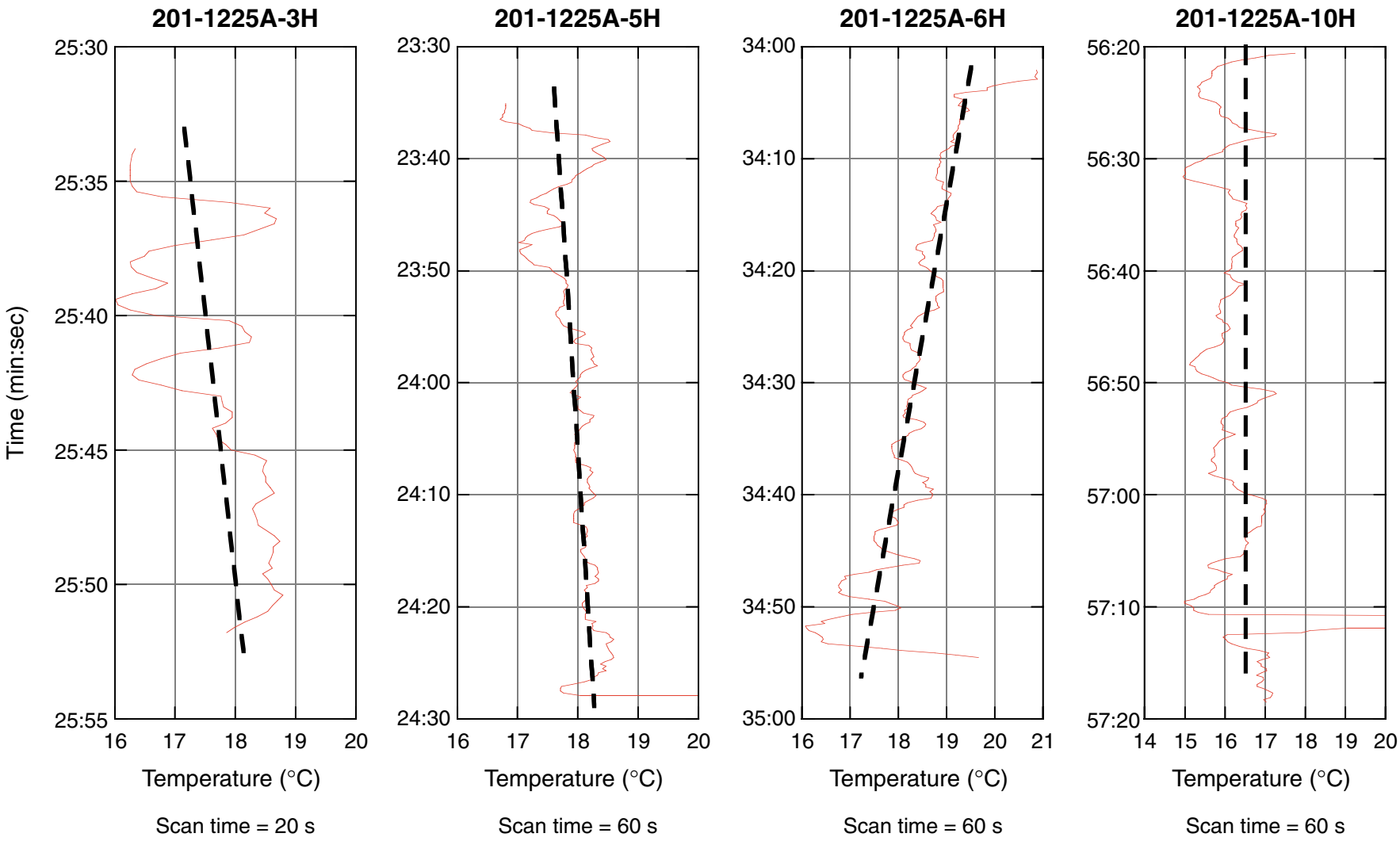

Figure F14. Comparison of temperature trends measured with the IR camera for cores from Holes 1225A and 1225C. No correlation is evident.

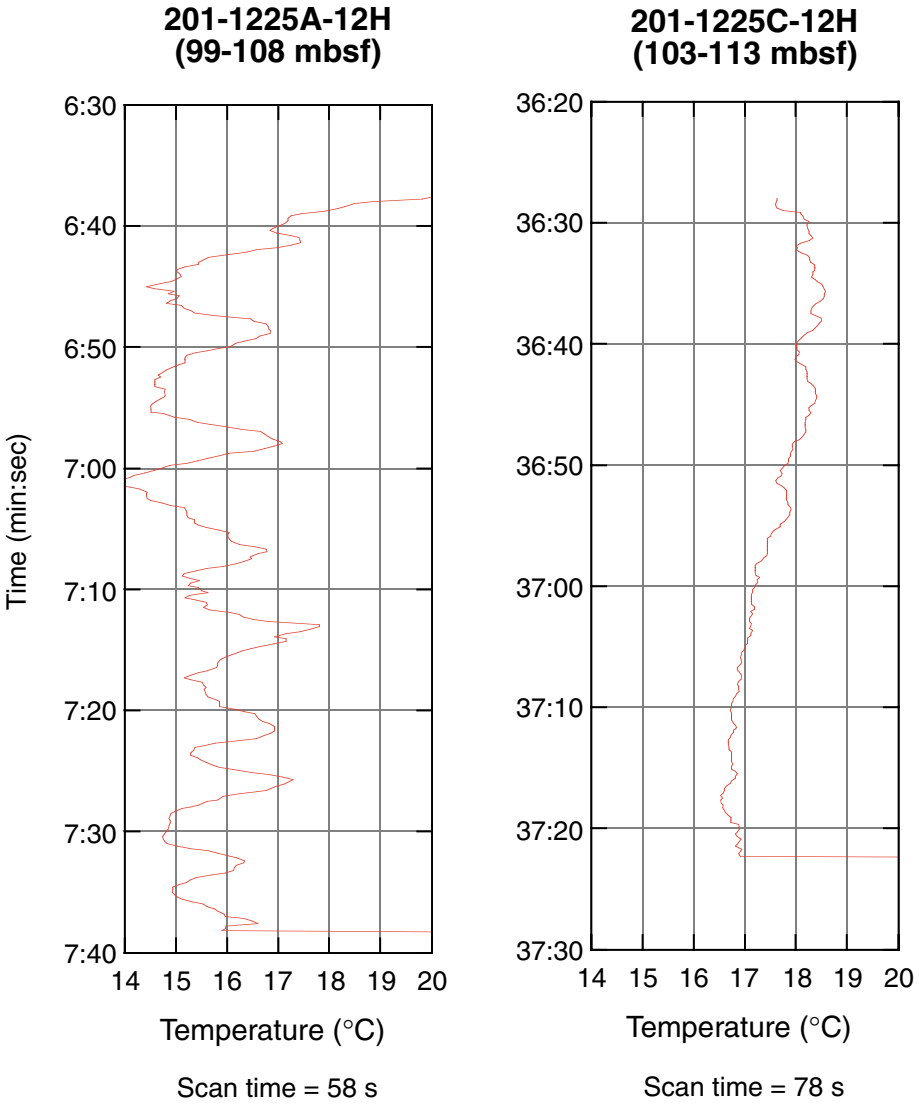

Figure F15. Image of the bottom end of Section 201-1225A-10H-1, taken immediately after section splits. The lowest temperature, 12.6°C, near the middle of the core is indicated by the cross. The radial warming of the core from its wire line trip is evident, with the warmest temperatures present adjacent to the core liner.

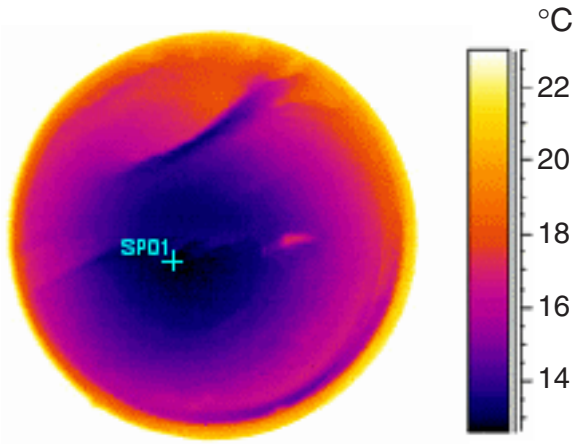

Figure F16. Temperature increase of an exposed section end (Section 201-1225A-11H-6, bottom). Temperature in the core center at the start is 9.6°C. Within 20 min the rate of temperature increase has slowed, and a maximum temperature of 18.5°C was recorded during the experiment.

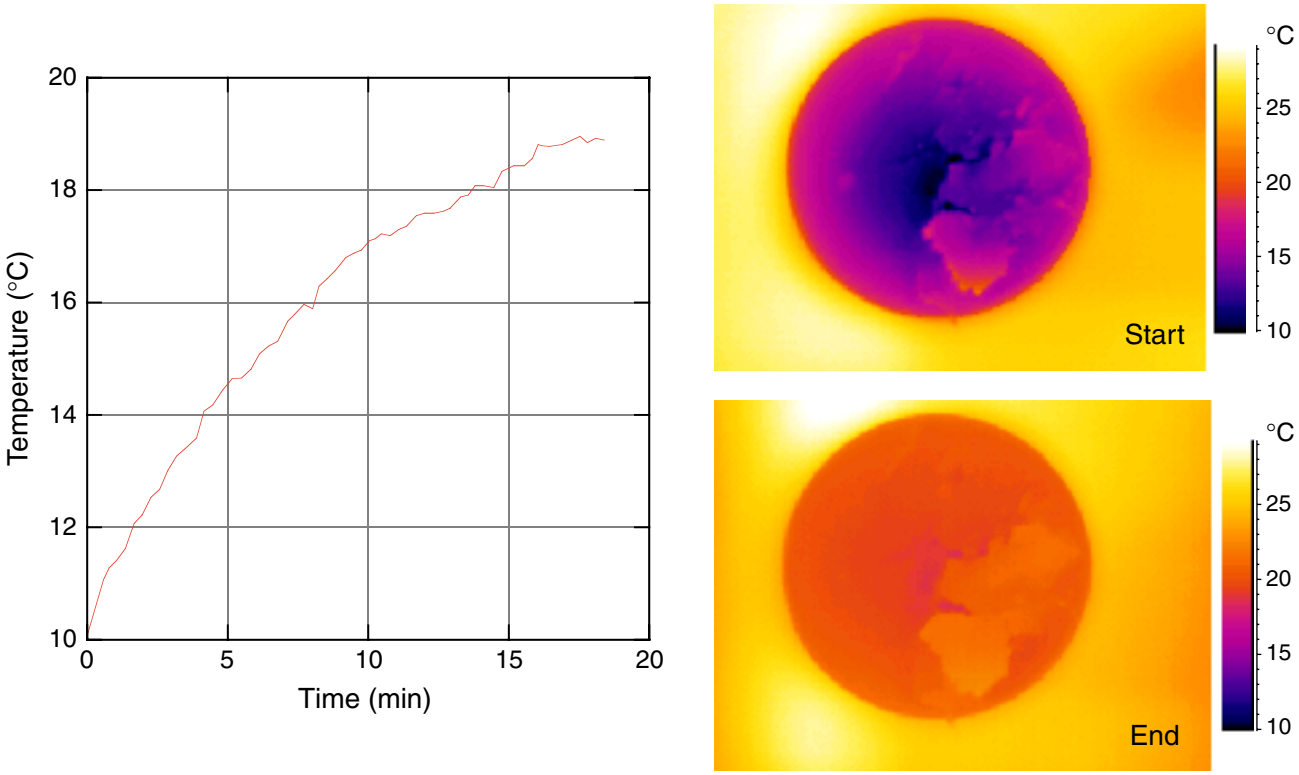

Figure F17. Comparison of magnetic susceptibility data from Sites 1225 and 851.

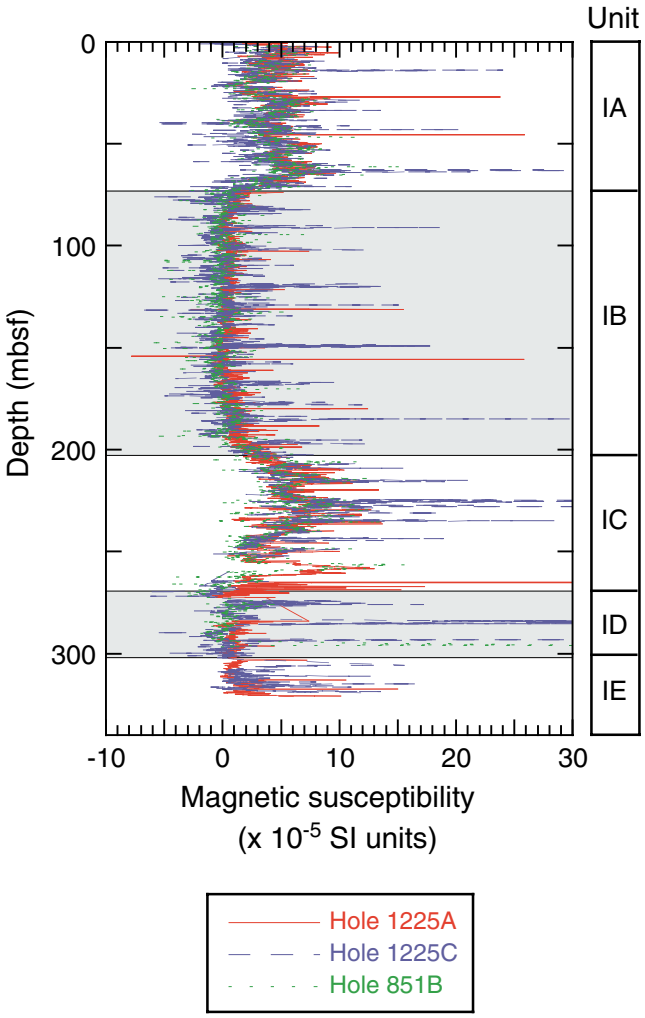

Figure F18. A. Declination and inclination profiles for the uppermost 90 m of Hole 1225A, demagnetized at 15 mT, with identification of polarity chronozones. **B.** Declination and inclination profiles for the lowermost 110 m of Hole 1225A, demagnetized at 15 mT.

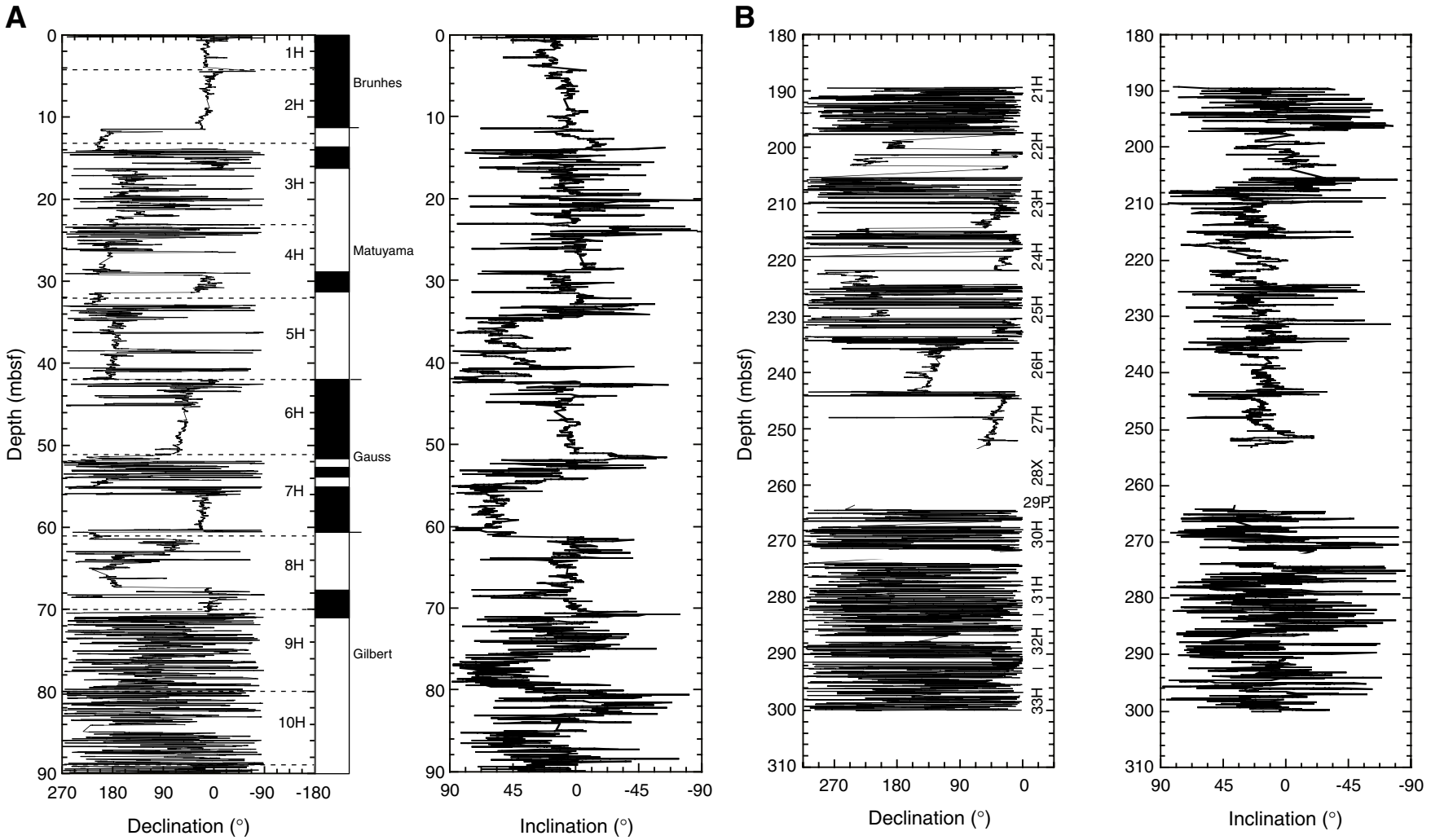

Figure F19. Magnetic intensity at Site 1225. Solid squares show the intensity of archive-half sections after 15-mT AF demagnetization measured by pass-through cryogenic magnetometer in Hole 1225A. Open squares show the intensity of discrete samples from the working half of cores after 20-mT AF demagnetization measured by spinner magnetometer in Hole 1225C.

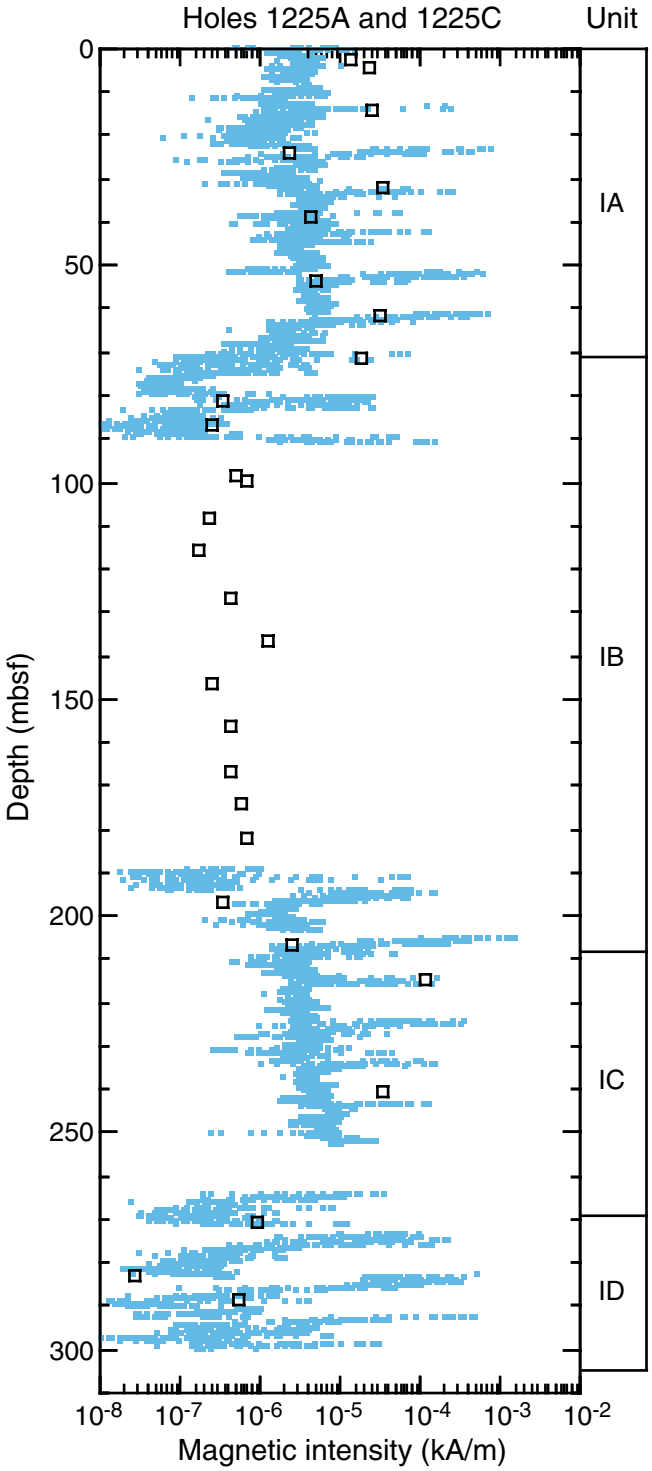

Figure F20. Principal component analysis of natural remanent magnetization (NRM) of Sample 201-1225C-1H-2, 93.5–95.5 cm, including equal-area projection of directions of magnetization during demagnetization, intensity of magnetization plotted vs. demagnetization, and vector component diagrams showing projection of magnetic vector's endpoints on horizontal and vertical planes.

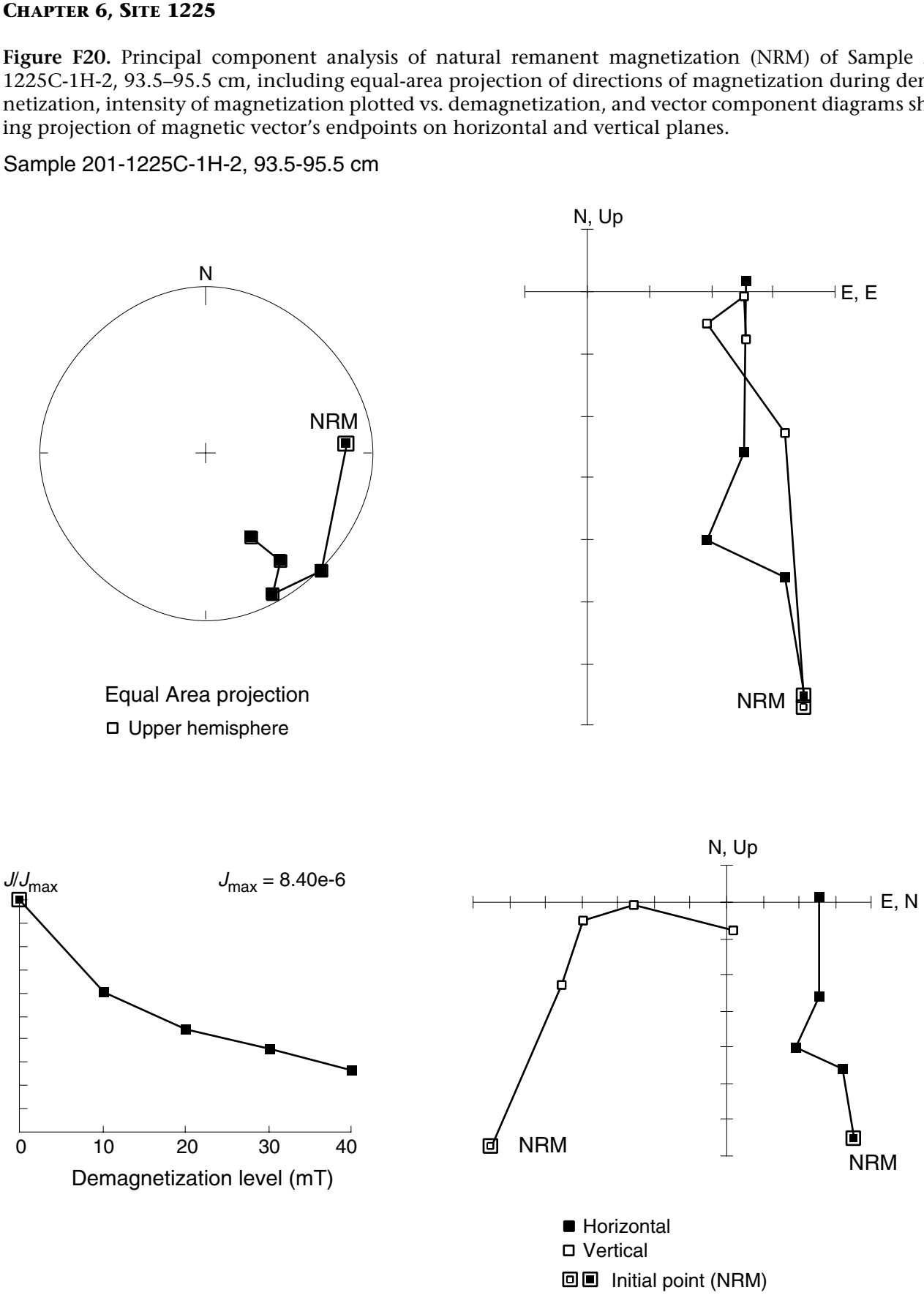

Figure F21. Principal component analysis of natural remanent magnetization (NRM) of Sample 201-1225C-1H-3, 109–111 cm, including equal area projection of directions of magnetization during demagnetization, intensity of magnetization plotted vs. demagnetization, and vector component diagrams showing projection of magnetic vector's endpoints on horizontal and vertical planes.

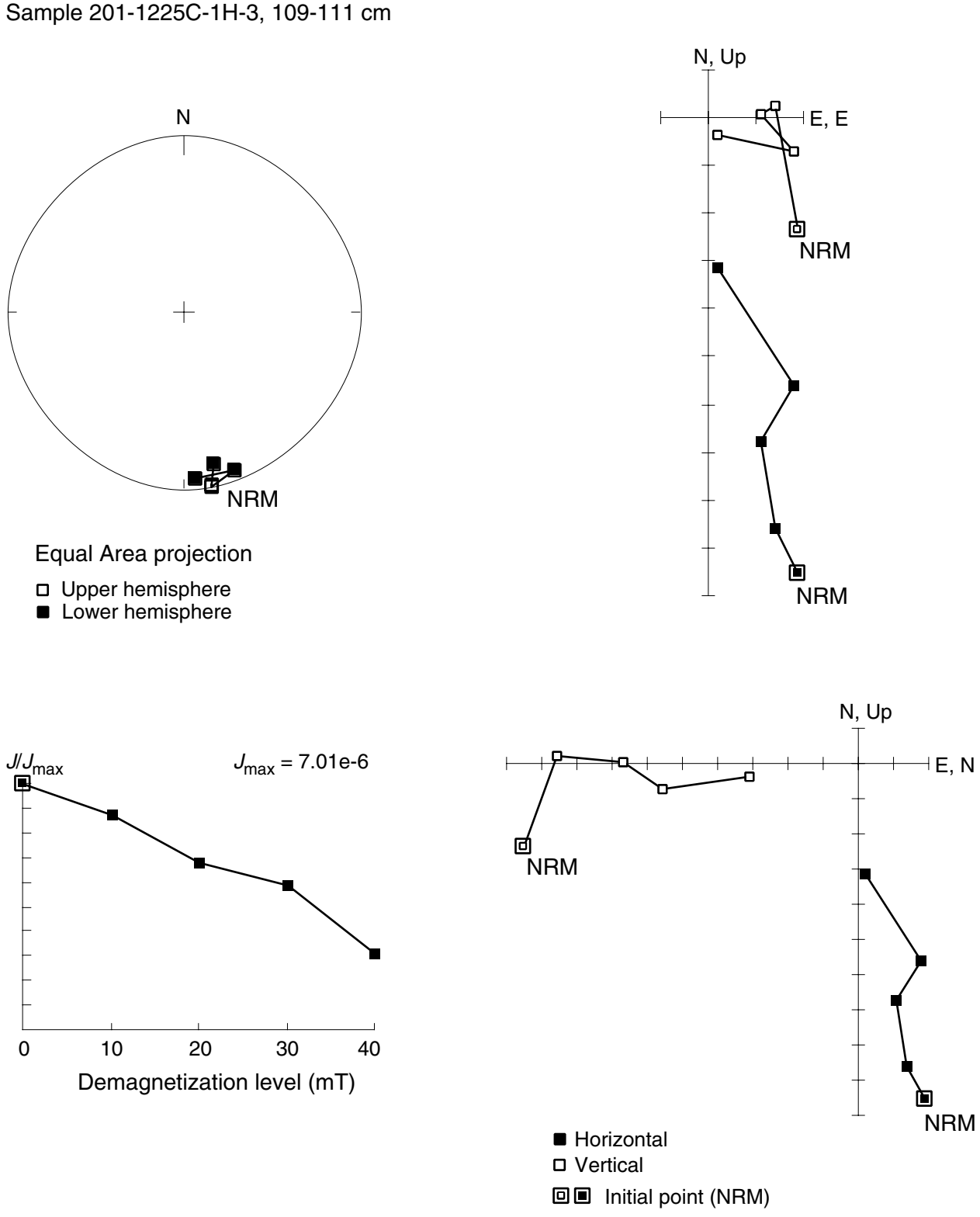

Figure F22. Principal component analysis of natural remanent magnetization (NRM) of Sample 201-1225C-5H-1, 138–140 cm, including equal area projection of directions of magnetization during demagnetization, intensity of magnetization plotted vs. demagnetization, and vector component diagrams showing projection of magnetic vector's endpoints on horizontal and vertical planes.

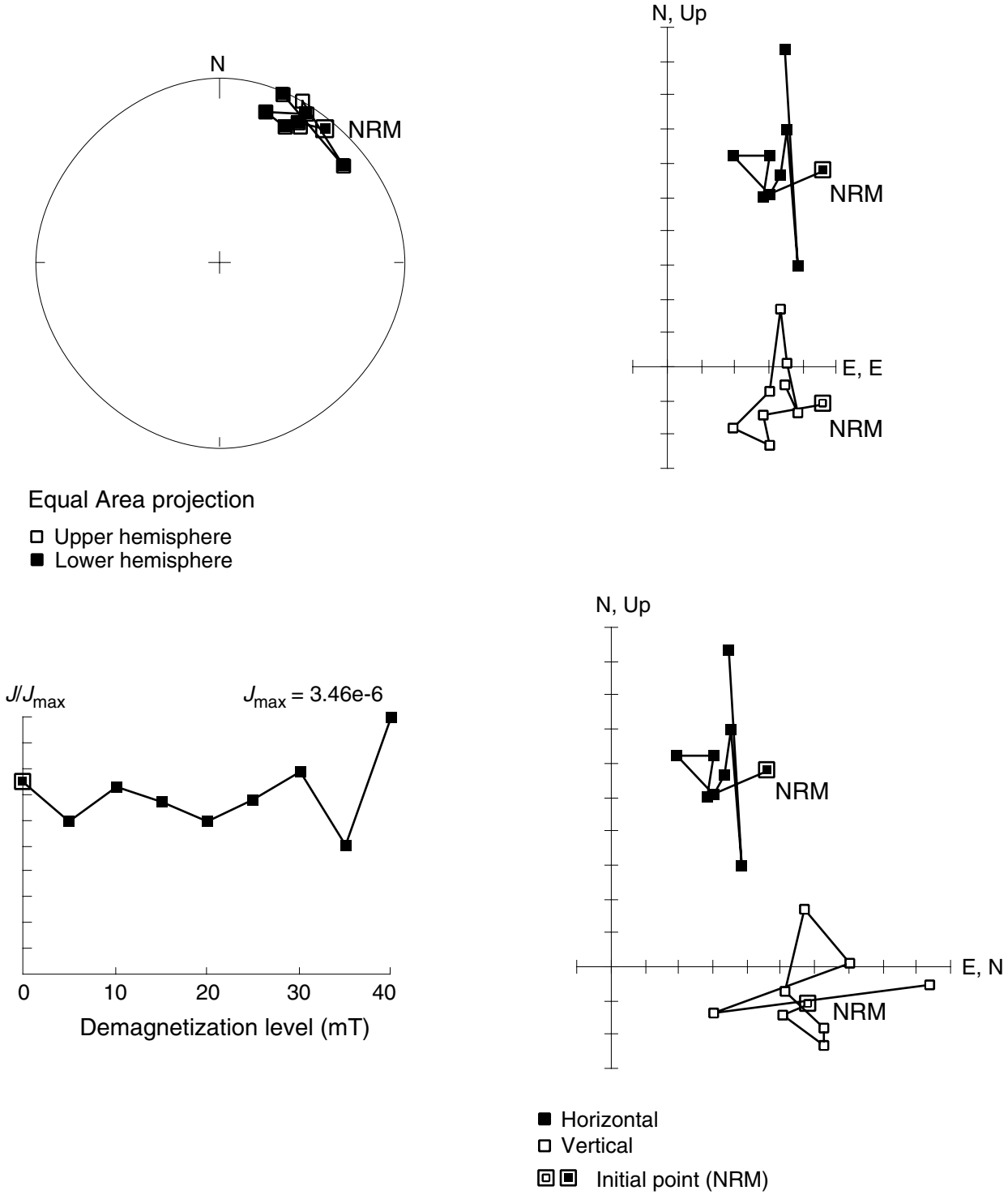

Figure F23. Principal component analysis of natural remanent magnetization (NRM) of Sample 201-1225C-23H-5, 69–71 cm, including equal area projection of directions of magnetization during demagnetization, intensity of magnetization plotted vs. demagnetization, and vector component diagrams showing projection of magnetic vector's endpoints on horizontal and vertical planes.

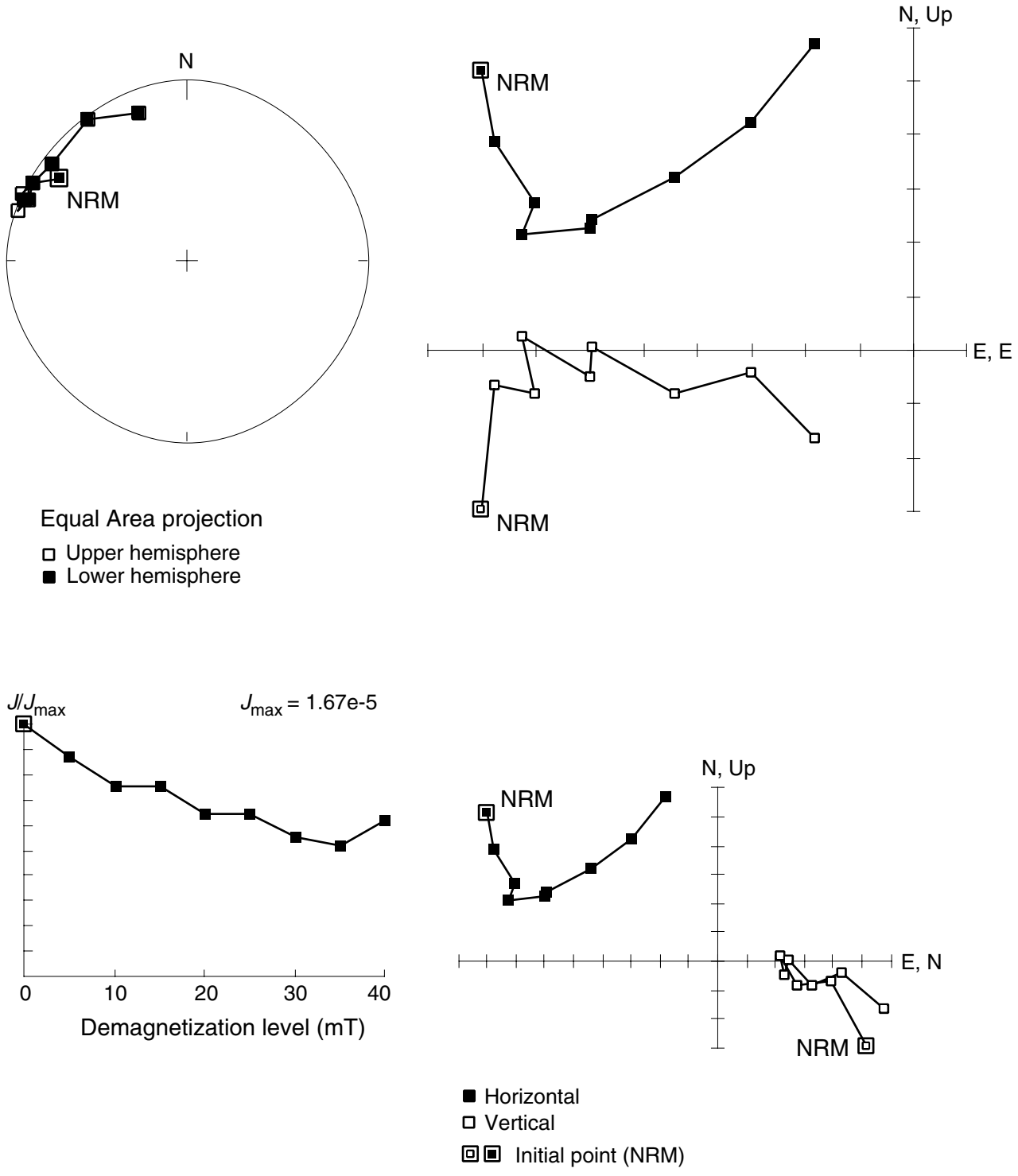

Figure F24. Comparison of GRA density data from Site 1225 (Holes 1225A and 1225C) and Hole 851B.

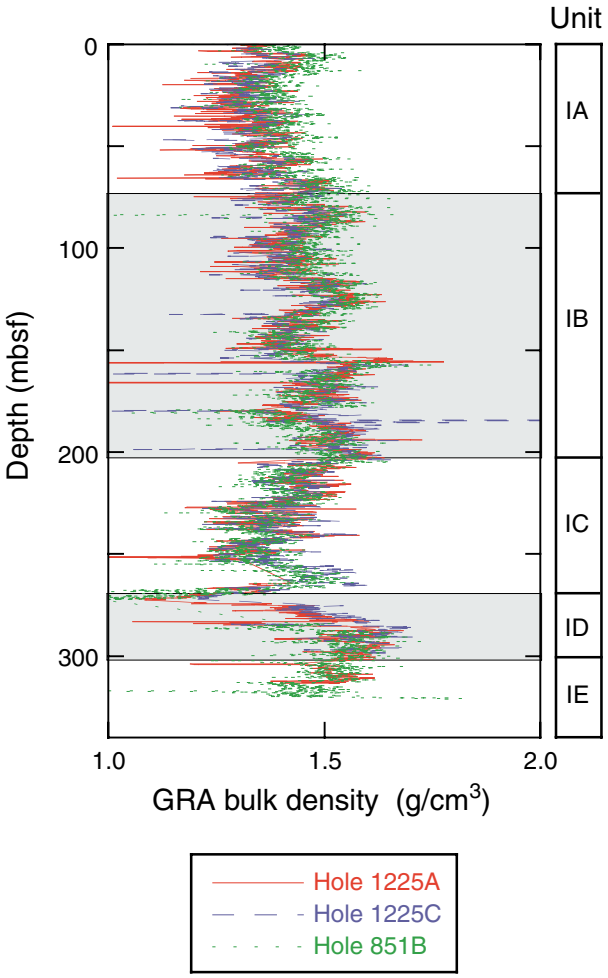

Figure F25. Moving averages (5 m) for Holes 1225A and 851B. Gamma ray attenuation (GRA) density data are overlain on Hole 1225A moisture and density (MAD) measurements. The two GRA-based density profiles are statistically not significantly different.

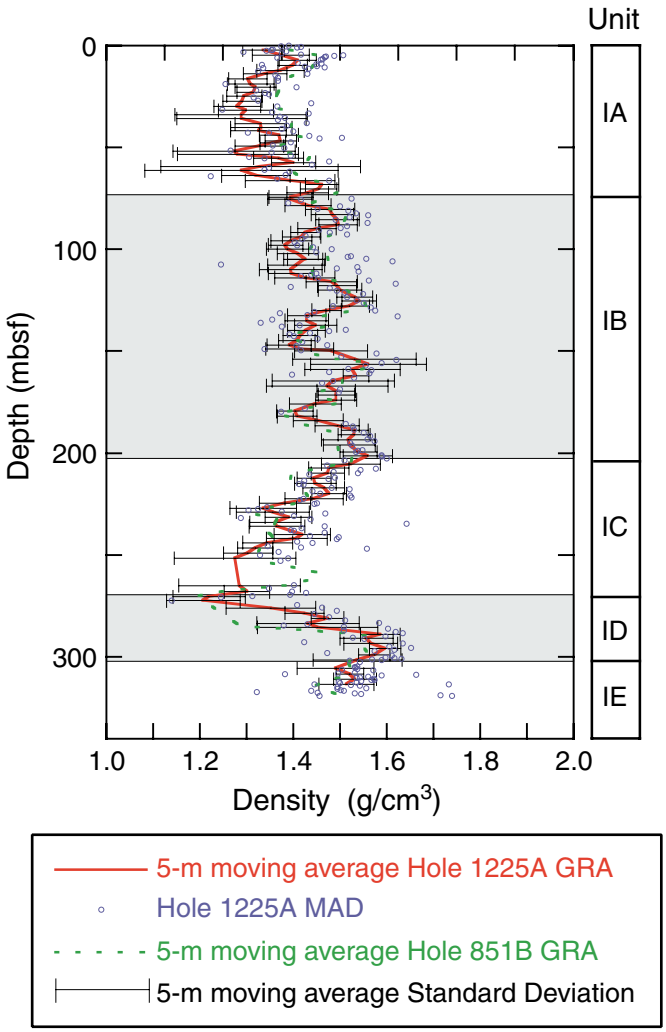

Figure F26. Hole 1225A measurements. **A.** GRA-based and mass/volume (MAD) bulk density. **B.** Grain density. **C.** Porosity.

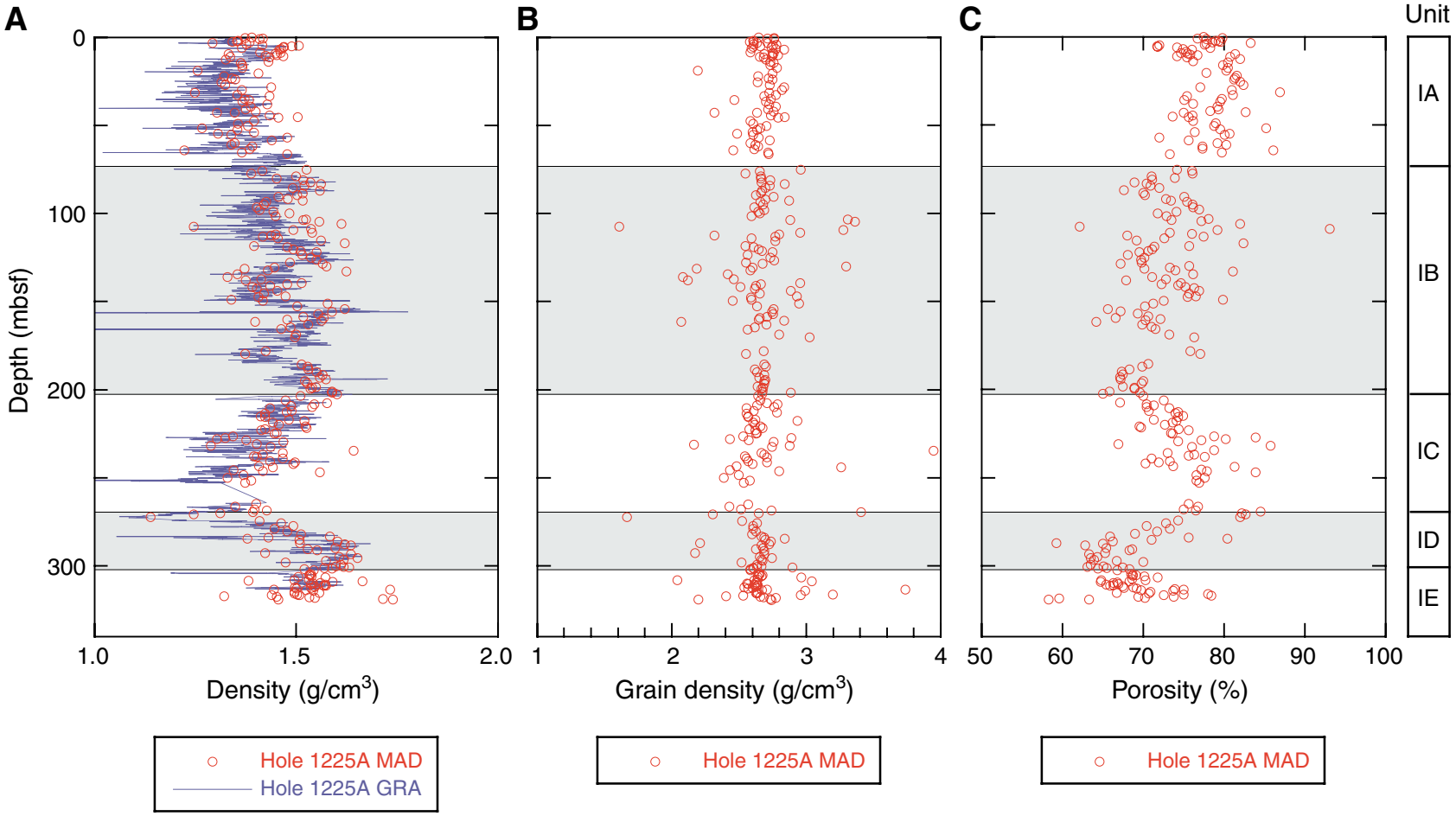

Figure F27. Velocity profiles from the MST (*P*-wave logger [PWL]) and the PWS. The velocities measured by the MST are consistently lower, except in Subunit IC.

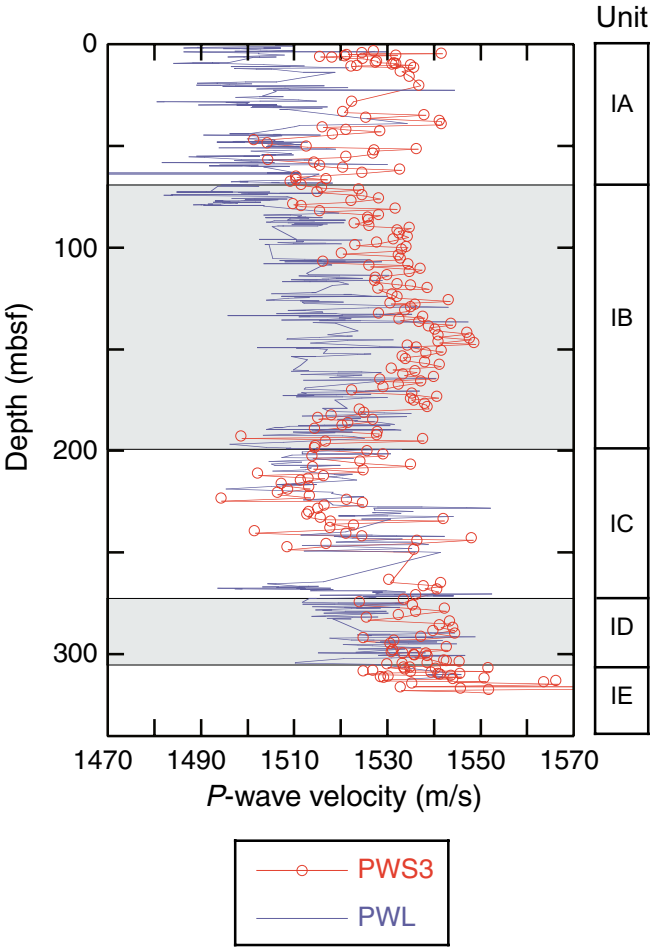

Figure F28. Comparison of natural gamma radiation (NGR) for multisensor track (MST)-derived (Holes 1225A and 1225C) and wireline logging (Hole 1225A) data.

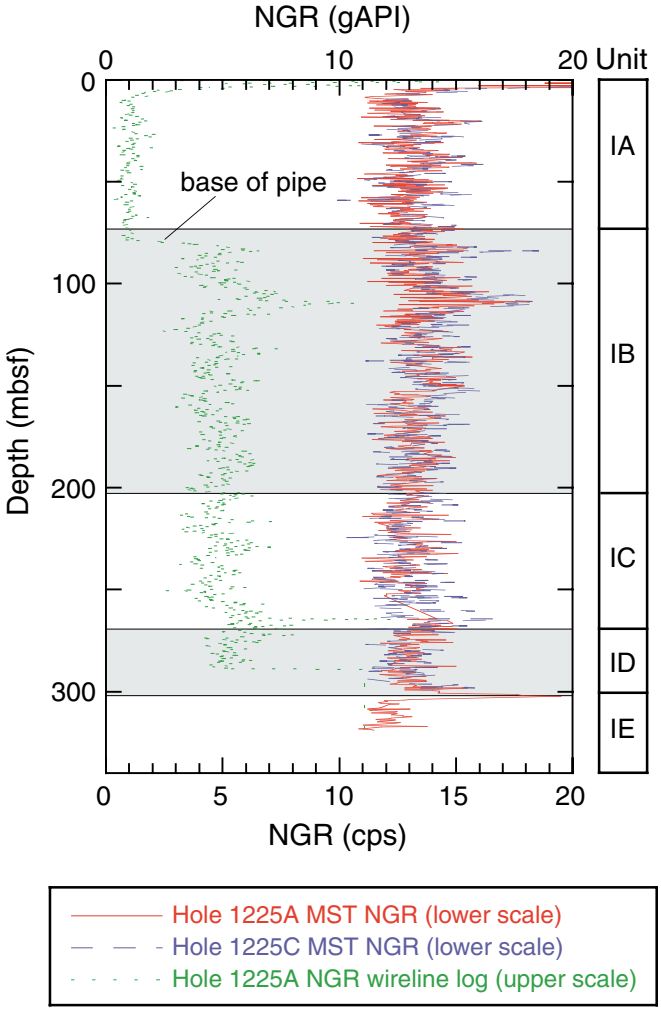

Figure F29. Thermal conductivity and projected temperature profiles for Hole 1225A. **A.** Thermal conductivity measurements made using needle-probe instrument. **B.** Comparison of profile mean-normalized thermal conductivity and bulk density. The correlation between the two data sets shows that thermal conductivity variations are dependent on water content. **C.** Observed and projected temperatures in Hole 1225A. GRA = gamma ray attenuation.

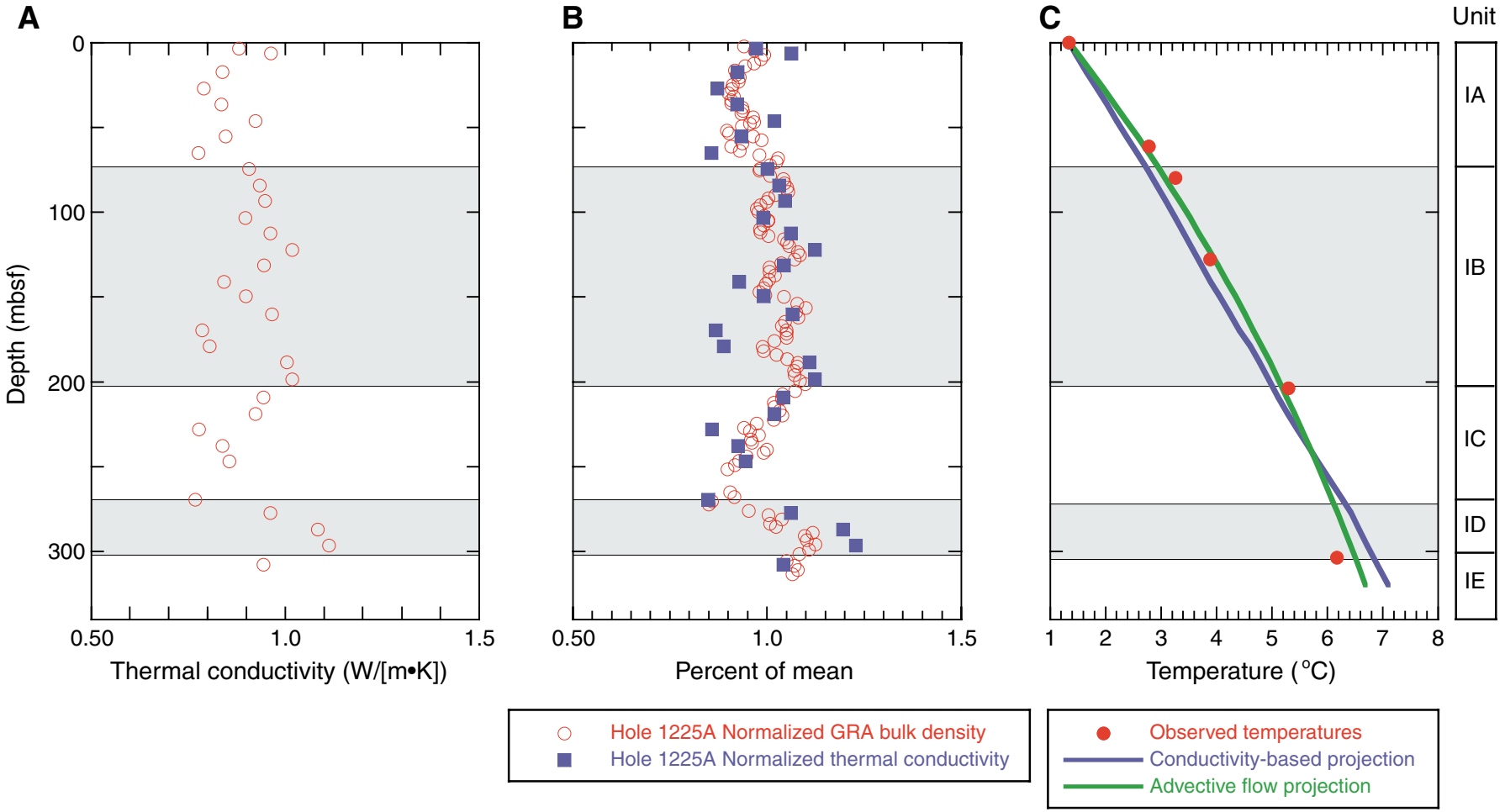

Figure F30. Downhole profile of formation factor and conductive anisotropy (axial [z] relative to transverse [y] measurements).

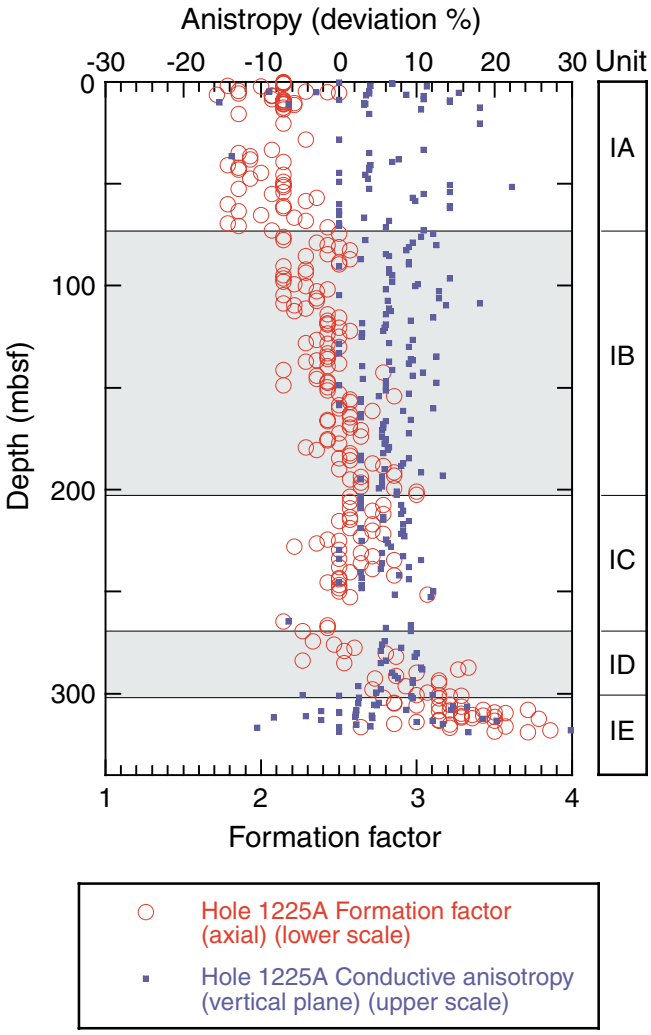

Figure F31. All temperatures measured in Hole 1225A plotted vs. depth with best-fit linear profile. DVTP = Davis-Villinger Temperature Probe.

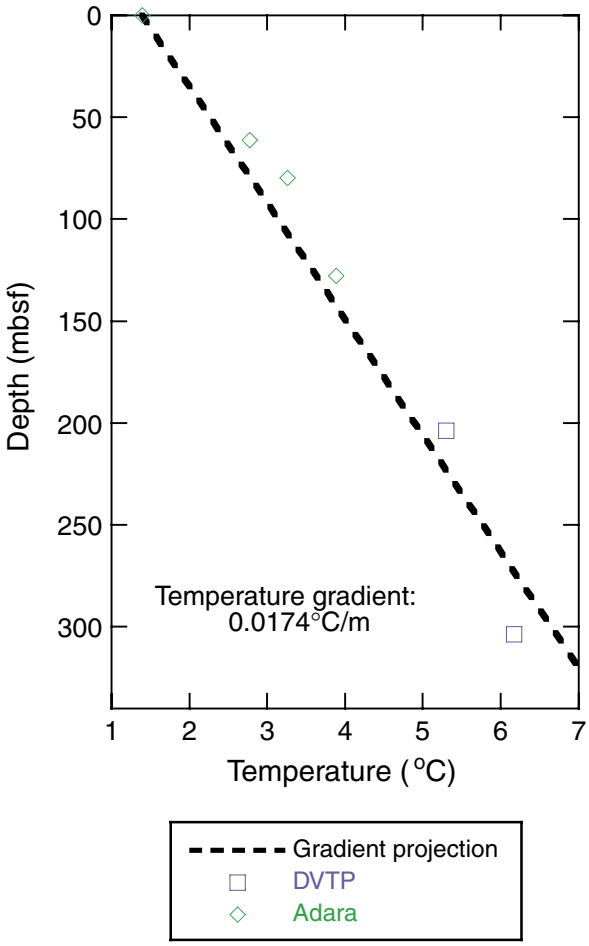

Figure F32. Main logs recorded in Hole 1225A. **A.** Hole diameter is measured by the caliper arm of the density sonde. **B.** Gamma radiation is a measure of the natural radioactivity of the formation. **C.** Concentrations of potassium, thorium, and uranium derived from the gamma ray counts. **D.** Resistivity measured by the Phasor Dual Induction tool with three depths of investigation. **E.** Density log (red line) compared with density measurements made on core samples (shaded circles) (see **"Density and Porosity,"** p. 27, in "Physical Properties"). **F.** Porosity log for the two receivers spacing of the Accelerator Porosity Sonde (APS) compared with porosity measurements made on core samples (shaded circles) (see **"Density and Porosity,"** p. 27, in "Physical Properties"). HNGS = Hostile Environment Natural Gamma Ray Sonde, SGT = Scintillation Gamma Ray Tool.

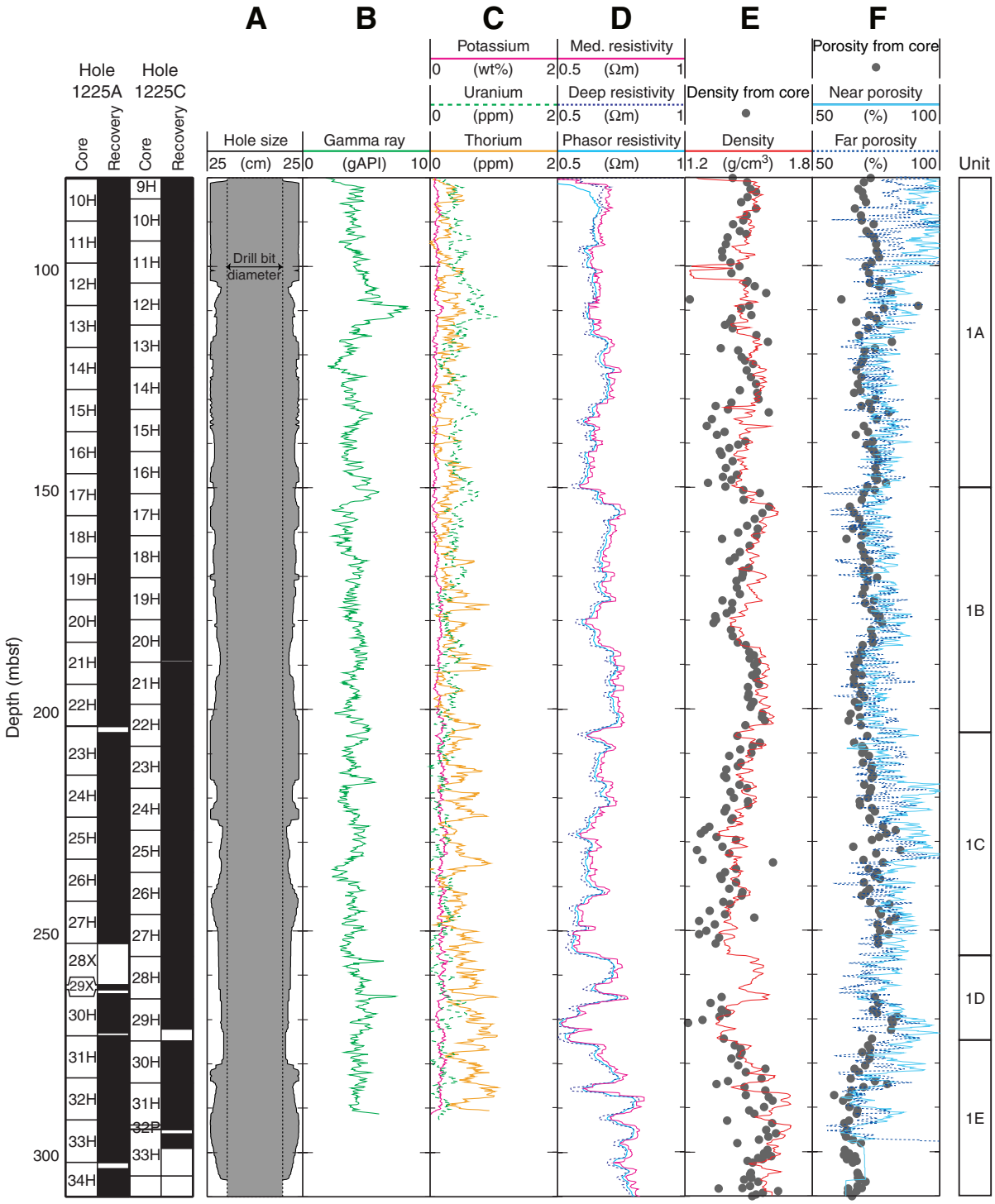

Figure F33. Comparison between logs from Hole 1225A (red) and the data recorded during ODP Leg 138 in neighboring Hole 851B (green). **A.** Hole diameter. **B.** Gamma radiation. **C.** Thorium. **D.** Uranium. **E.** Potassium. **F.** Medium resistivity. **G.** Density.

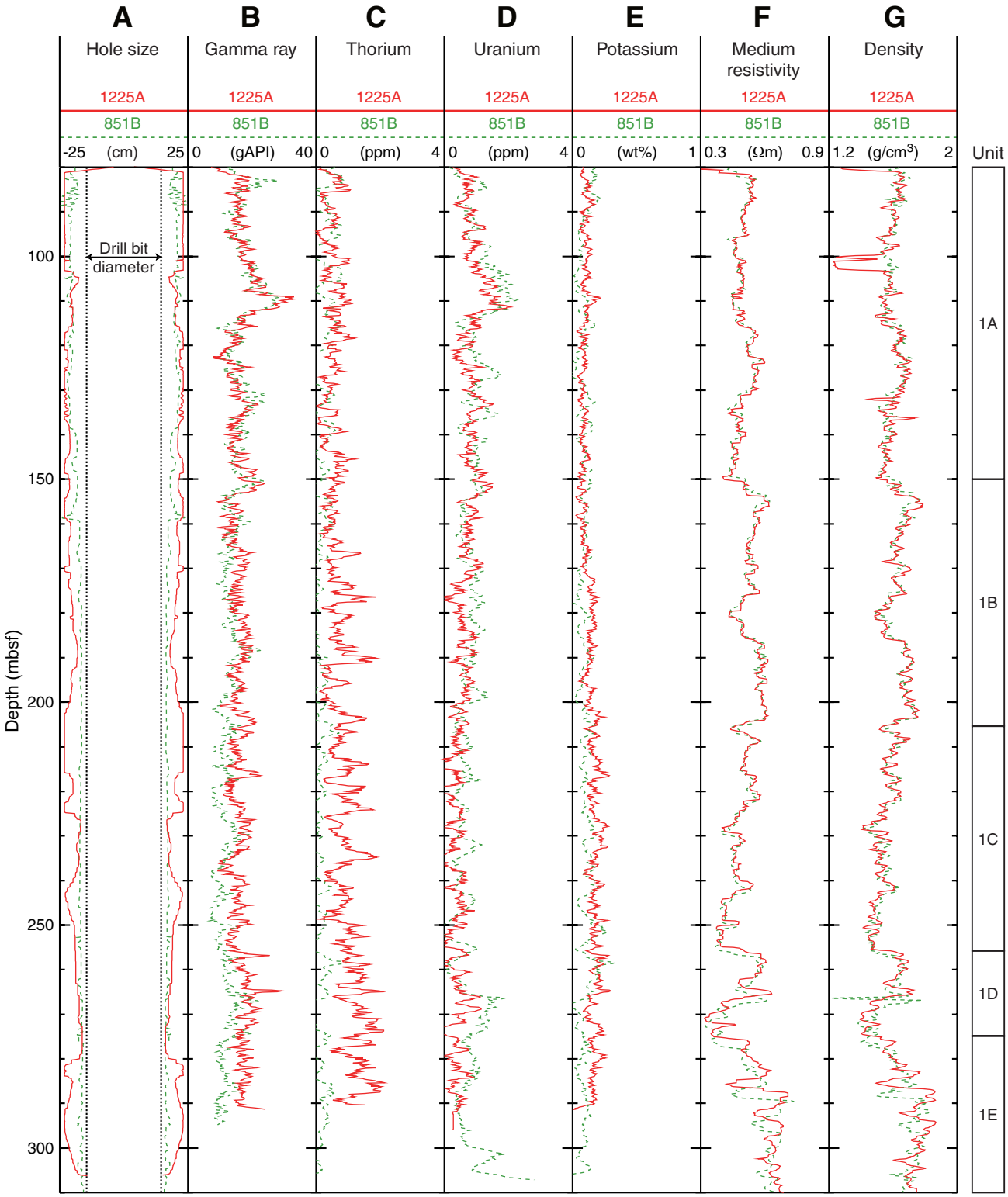

Figure F34. Temperature log recorded in Hole 1225A. Temperature data were recorded continuously during the two passes of the tool string.

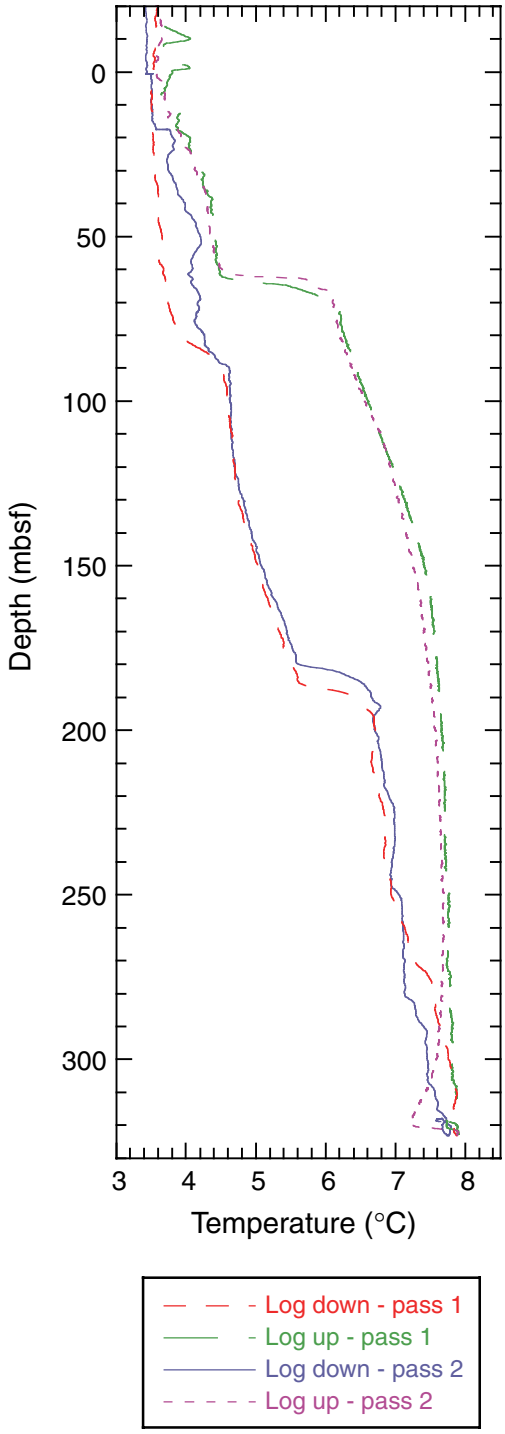

Table T1. Coring summary, Site 1225. (Continued on next page.)

Hole 1225A
Latitude: 2°46.2469′N
Longitude: 110°34.2889′W
Time on site (hr): 132.25 (2125 hr, 7 Feb–0930 hr, 13 Feb 2002)
Time on hole (hr): 86.00 (2115 hr, 7 Feb–1115, 11 Feb 2002)
Seafloor (drill pipe measurement from rig floor, mbrf): 3772.20
Distance between rig floor and sea level (m): 10.90
Water depth (drill pipe measurement from sea level, m): 3761.30
Total depth (drill pipe measurement from rig floor, mbrf): 4091.80
Total penetration (meters below seafloor, mbsf): 319.60
Total length of cored section (m): 315.60
Total length of drilled intervals (m): 4.00
Total core recovered (m): 321.65
Core recovery (%): 101.92
Total number of cores: 35
Total number of drilled intervals: 3

Hole 1225B
Latitude: 2°46.2526′N
Longitude: 110°34.2891′W
Time on hole (hr): 2.00 (1115 hr, 11 Feb–1315 hr, 11 Feb 2002)
Seafloor (drill pipe measurement from rig floor, mbrf): 3771.0
Distance between rig floor and sea level (m): 10.9
Water depth (drill pipe measurement from sea level, m): 3760.1
Total depth (drill pipe measurement from rig floor, mbrf): 3780.0
Total penetration (meters below seafloor, mbsf): 9.0
Total length of cored section (m): 9.0
Total length of drilled intervals (m): 0.0
Total core recovered (m): 8.96
Core recovery (%): 99.6
Total number of cores: 1
Total number of drilled intervals: 0

Hole 1225C
Latitude: 2°46.2572′N
Longitude: 110°34.2890′W
Time on hole (hr): 44.25 (1315 hr, 11 Feb–0930 hr, 13 Feb 2002)
Seafloor (drill pipe measurement from rig floor, mbrf): 3771.2
Distance between rig floor and sea level (m): 11.0
Water depth (drill pipe measurement from sea level, m): 3760.2
Total depth (drill pipe measurement from rig floor, mbrf): 4076.5
Total penetration (mbsf): 305.3
Total length of cored section (m): 304.3
Total length of drilled intervals (m): 1.0
Total core recovered (m): 305.51
Core recovery (%): 100.4
Total number of cores: 33
Total number of drilled intervals: 1

Core	Date (Feb 2002)	Local time (hr)	Depth (mbsf) Top	Depth (mbsf) Bottom	Length (m) Cored	Length (m) Recovered	Recovery (%)
201-1225A-							
1H	8	0900	0.0	4.3	4.3	4.29	99.8
2H	8	1015	4.3	13.8	9.5	10.03	105.6
3H	8	1120	13.8	23.3	9.5	9.85	103.7
4H	8	1230	23.3	32.8	9.5	9.81	103.3
5H	8	1415	32.8	42.3	9.5	10.16	107.0
6H	8	1525	42.3	51.8	9.5	10.11	106.4
7H	8	1705	51.8	61.3	9.5	9.95	104.7
8H	8	1815	61.3	70.8	9.5	10.01	105.4
9H	8	1945	70.8	80.3	9.5	10.02	105.5
10H	8	2050	80.3	89.8	9.5	10.06	105.9
11H	8	2155	89.8	99.3	9.5	10.01	105.4
12H	8	2300	99.3	108.8	9.5	9.96	104.8
13H	9	0010	108.8	118.3	9.5	10.03	105.6
14H	9	0150	118.3	127.8	9.5	10.23	107.7
15H	9	0310	127.8	137.3	9.5	9.98	105.1
16H	9	0415	137.3	146.8	9.5	10.23	107.7
17H	9	0540	146.8	156.3	9.5	9.56	100.6
18H	9	0655	156.3	165.8	9.5	9.78	103.0

Table T1 (continued).

Core	Date (Feb 2002)	Local time (hr)	Depth (mbsf) Top	Depth (mbsf) Bottom	Length (m) Cored	Length (m) Recovered	Recovery (%)
19H	9	0800	165.8	175.3	9.5	9.98	105.1
20H	9	0925	175.3	184.8	9.5	9.96	104.8
21H	9	1025	184.8	194.3	9.5	9.62	101.3
22H	9	1145	194.3	203.8	9.5	9.96	104.8
			*****Drilled from 203.8 to 205.3 mbsf*****				
23H	9	1715	205.3	214.8	9.5	10.11	106.4
24H	9	1835	214.8	224.3	9.5	10.05	105.8
25H	9	1950	224.3	233.8	9.5	10.03	105.6
26H	9	2135	233.8	243.3	9.5	10.02	105.5
27H	9	2325	243.3	252.8	9.5	10.13	106.6
28X	10	0330	252.8	262.2	9.4	0.00	0.0
29P	10	0530	262.2	263.2	1.0	1.41	141.0
			*****Drilled from 263.2 to 264.2 mbsf*****				
30H	10	0725	264.2	273.7	9.5	8.79	92.5
31H	10	0905	273.7	283.2	9.5	10.12	106.5
32H	10	1050	283.2	292.7	9.5	10.00	105.3
33H	10	1230	292.7	302.2	9.5	10.03	105.6
			*****Drilled from 302.2 to 303.7 mbsf*****				
34H	10	1745	303.7	313.2	9.5	10.12	106.5
35X	10	1925	313.2	319.6	6.4	7.25	113.3
				Cored totals:	315.6	321.65	101.9
				Drilled total:	4.0		
				Total:	319.6		
201-1225B-							
1H	11	1310	0.0	9.0	9.0	8.96	99.6
				Cored totals:	9.0	8.96	99.6
201-1225C-							
1H	11	1415	0.0	8.8	8.8	8.79	99.9
2H	11	1510	8.8	18.3	9.5	9.96	104.8
3H	11	1630	18.3	27.8	9.5	10.04	105.7
4H	11	1720	27.8	37.3	9.5	10.01	105.4
5H	11	1840	37.3	46.8	9.5	9.31	98.0
6H	11	1935	46.8	56.3	9.5	10.02	105.5
7H	11	2035	56.3	65.8	9.5	9.84	103.6
8H	11	2135	65.8	75.3	9.5	10.02	105.5
9H	11	2230	75.3	84.8	9.5	9.87	103.9
10H	11	2325	84.8	94.3	9.5	9.73	102.4
11H	12	0025	94.3	103.8	9.5	9.91	104.3
12H	12	0125	103.8	113.3	9.5	9.64	101.5
13H	12	0220	113.3	122.8	9.5	9.84	103.6
14H	12	0320	122.8	132.3	9.5	9.83	103.5
15H	12	0415	132.3	141.8	9.5	9.80	103.2
16H	12	0525	141.8	151.3	9.5	10.05	105.8
17H	12	0700	151.3	160.8	9.5	9.52	100.2
18H	12	0800	160.8	170.3	9.5	9.66	101.7
19H	12	0900	170.3	179.8	9.5	9.86	103.8
20H	12	0950	179.8	189.3	9.5	9.13	96.1
21H	12	1055	189.3	198.8	9.5	9.70	102.1
22H	12	1200	198.8	208.3	9.5	9.65	101.6
23H	12	1325	208.3	217.8	9.5	9.89	104.1
24H	12	1445	217.8	227.3	9.5	10.02	105.5
25H	12	1645	227.3	236.8	9.5	9.95	104.7
26H	12	1830	236.8	246.3	9.5	10.08	106.1
27H	12	1940	246.3	255.8	9.5	10.06	105.9
28H	12	2110	255.8	265.3	9.5	10.08	106.1
29H	12	2230	265.3	274.8	9.5	6.86	72.2
30H	13	0005	274.8	284.3	9.5	10.04	105.7
31H	13	0145	284.3	293.8	9.5	10.09	106.2
32P	13	0330	293.8	294.8	1.0	1.02	102.0
			*****Drilled from 294.8 to 295.8 mbsf*****				
33H	13	1845	295.8	305.3	9.5	3.24	34.1
				Cored totals:	304.3	305.51	100.4
				Drilled total:	1.0		
				Total:	305.3		

Table T2. Concentrations of dissolved species in interstitial waters, Holes 1225A and 1225C. (See table notes. Continued on next two pages.)

Core, section, interval (cm)	Depth (mbsf)	pH	Alk (mM)	SAL	Cl^- (mM)		SO_4^{2-} (mM)	H_4SiO_4 (µM)	HPO_4^{2-} (µM)	NH_4^+ (µM)	Fe (µM)	Mn (µM)	Sr (µM)	ΣH_2S (mM)	DIC (mM)	VFA (µm)		NO_3^- (µM)
																Acetate	Formate	
201-1225A-																		
1H-2, 0-15	1.50	7.66	2.67	34.5	553.8		28.76	625	4.1	6.2	0.3	94.0	88			BDL	0.9	
2H-3, 0-15	7.30	7.22	3.10	34.0	558.9		28.45	531	2.4		8.3	119.3	87	BDL		BDL	<0.2	
3H-2, 135-150	16.65	7.60	2.79	34.0	563.4		28.98	664	1.9		5.3	89.5	91	BDL		BDL	0.7	
4H-3, 0-15	26.30	7.54	3.19	34.0	565.9		28.06	720	2.1	38.5	15.6	92.7		BDL		BDL	0.5	
6H-3, 0-15	45.30	7.57	2.81	35.0	565.9		27.63	771	1.8	51.9	7.6	66.1		BDL				
8H-3, 0-15	64.30	7.66	2.83	34.5	565.9		27.90		1.3	60.4	13.7	33.6		BDL		BDL	0.5	
10H-3, 0-15	83.30	7.50	3.43	34.5	564.9		27.05	866	1.9	64.8	5.6	4.9		BDL				
11H-3, 135-150	94.15	7.47	3.55	35.0	563.9		27.09	822	1.9	65.9		11.4		BDL		BDL	0.7	
12H-3, 0-15	102.30	7.48	3.48	34.5	564.4		27.33	895	1.8	68.6	1.8	3.3	120	BDL		1.0	<0.2	
13H-3, 135-150	113.15	7.43	3.57	34.0	565.6		29.04	920	1.8	70.3	5.6	2.3	127	BDL		BDL	0.4	
14H-1, 135-150	119.65			34.5			27.68							BDL				
14H-3, 0-15	121.30	7.45	3.64		566.1		26.89	938	1.7	72.9	6.7	2.0	129	BDL		BDL	<0.2	
16H-3, 0-15	140.30	7.46	3.88	34.0	564.9		26.95	946	1.8	73.7	4.1	2.4		BDL		BDL	<0.2	
18H-3, 0-15	159.30	7.49	3.78	34.5	563.9		26.99	1195	1.8	76.2	4.4	1.8	144	BDL		2.0	<0.2	
19H-3, 135-150	170.15	7.32	3.39	34.5	563.4		27.01	1024	1.5		12.3	2.4	154	BDL		BDL	0.3	
20H-3, 0-15	178.30	7.44	3.68	34.5	562.9		28.40	975	1.7	76.2	9.3	3.0	159	BDL		BDL	<0.2	
22H-3, 0-15	197.30	7.54	3.41	34.5	564.4		26.51	965			15.7	3.4	161	BDL		BDL	<0.2	
24H-3, 0-15	217.80	7.49	3.39	34.5	563.8		26.81	987			20.6	5.8	175	BDL		BDL	0.3	
26H-3, 0-15	236.80	7.50	3.60	34.5	562.8		26.83	1016			17.7	7.5	178	BDL				
27H-3, 135-150	247.65	7.47	3.57	34.5	563.3		27.12	1085		49.4	8.1	7.6	183	BDL		BDL	0.3	
30H-2, 0-15	265.59	7.50	3.46	35.0	563.7		26.65	1004			12.4	6.6	178	BDL				
31H-3, 135-150	278.05	7.53	3.11	34.5			28.48	1023		34.7	4.9	4.9	172	BDL				
32H-1, 122-137	284.42	7.55	3.40	34.5			28.07	1002	1.6		2.5	2.9	167	BDL				0.2
32H-3, 0-15	286.07	7.71	2.91	34.5	564.3		27.33	976		22.2	3.4	3.0	152	BDL				
33H-3, 135-150	297.05	7.51	2.75	34.5	564.0		26.98	987	1.5	14.9	2.7	1.3	140	BDL		BDL	<0.2	0.6
34H-1, 140-150	305.10													BDL				6.7
34H-3, 0-15	306.70	7.56	3.12	34.5	563.4		27.31	1029	1.2		2.1	0.3	122	BDL				7.0
35X-1, 135-150	314.55			34.0										BDL				
35X-5, 12-27	319.32						28.32	1026	1.3	5.4	2.7	0.5	101	BDL				22.7
201-1225C-																		
1H-1, 37-47	0.37	7.68	2.92		555.1		28.73		3.5		0.6	11.6	86					33.1
1H-1, 85-95	0.85				556.1				3.3		0.4	44.4	86					13.5
1H-2, 0-15	1.50				579.2	*	28.73		3.8		0.4	89.3	86					0.8
1H-3, 0-15	3.00								2.7		3.1	145.4	87		3.02			1.4
1H-3, 65-80	3.65								3.4		0.4	158.2	86	BDL				1.2
1H-4, 0-15	4.50				557.1				3.5		3.9	151.5	89					1.3
1H-5, 0-15	6.00										8.7	127.7	88	BDL				1.3
1H-6, 0-15	7.50				559.1				2.2		7.1	127.1	86					
1H-6, 60-75	8.10										6.6	117.6	88					1.0
2H-1, 135-150	10.15				561.4		28.55		2.2		5.6	96.4	89		3.15			
2H-2, 135-150	11.65								2.5		7.4	113.5	90					1.9
2H-3, 135-150	13.15				562.4				2.6		9.1	106.7	90		3.25			2.1
2H-5, 135-150	16.15				561.9		28.68		2.3		12.2	93.9	91					
3H-2, 135-150	21.15	7.10	3.29															
3H-5, 135-150	25.65								2.4		6.6	94.8	94					
4H-2, 135-150	30.65	7.56	2.89						2.2		8.7	75.3	94					0.2
4H-5, 135-150	35.15				589.0	*	28.14		2.3		7.3	74.9	90					0.9

Table T2 (continued).

Core, section, interval (cm)	Depth (mbsf)	pH	Alk (mM)	SAL	Cl^- (mM)		SO_4^{2-} (mM)	H_4SiO_4 (µM)	HPO_4^{2-} (µM)	NH_4^+ (µM)	Fe (µM)	Mn (µM)	Sr (µM)	ΣH_2S (mM)	DIC (mM)	VFA (µm)		NO_3^- (µM)
																Acetate	Formate	
5H-2, 135-150	40.15	7.50	3.40						2.5		6.2	77.4	95			BDL	<0.2	0.9
5H-5, 135-150	44.65				595.0	*	27.95		2.7		6.5	73.9	94			BDL	<0.2	3.0
6H-2, 135-150	49.65	7.45	2.98					774	2.7		5.1	57.8	96			BDL	0.4	
6H-5, 135-150	54.15				575.7	*	27.91	808	2.5		7.1	55.3	96					0.2
7H-2, 135-150	59.15	7.61	2.77						2.6		7.0	48.7	96			BDL	<0.2	0.3
7H-5, 135-150	63.65							776	2.3		4.7	38.2	100					0.3
8H-2, 135-150	68.65	7.47	2.72						2.6		6.3	29.2	98					1.2
8H-5, 135-150	73.15				535.4	*	27.19	796	1.6		5.3				3.27	BDL	0.5	
9H-2, 135-150	78.15	7.41	3.35						1.8		4.0	18.1	105					
9H-5, 135-150	82.65							835	1.6		6.3	13.3	107					
10H-2, 135-150	87.65	7.50	3.69						1.7		5.2	8.5	108					1.3
10H-5, 135-150	92.15				569.2	*	27.32	856	1.6		3.8	6.6	112		3.62			
11H-2, 135-150	97.15	7.33	3.35								2.4	4.2	116					
11H-5, 135-150	101.65							827	1.9		3.3	3.4	116					
12H-2, 135-150	106.65	7.33	3.90						1.8		0.8	3.0	117					0.9
12H-5, 135-150	111.15				566.1	*	27.35	953	1.9		2.1	2.6	122					
13H-2, 135-150	116.15	7.52	3.44						2.0		1.7	2.5	121		3.52			
13H-5, 135-150	120.65							941	1.8		2.3	2.2	125		3.55			
14H-2, 135-150	125.65	7.40	3.52						1.9		6.2	2.1	125					1.0
14H-5, 135-150	130.15				581.9	*	26.89	934	1.9		4.4	2.4	131		3.75			
15H-2, 135-150	135.15	7.49	3.57						1.9		3.0	2.6	133					
15H-5, 135-150	139.65							1004	1.6		2.3	2.4	135		3.68			
16H-2, 135-150	144.65	7.47	3.59						1.8		2.9	2.2	141		3.88			
16H-5, 135-150	149.15				552.7	*	27.27	996	1.9		1.3	2.1	139		3.71			
17H-3, 121-136	154.89	7.54	3.59						2.1		4.4	1.8	141		3.85			
17H-5, 135-150	157.89								2.0		3.3	1.9	140					
18H-2, 135-150	163.65	7.52	3.56					1052	1.9		2.1	2.0	147					0.9
18H-5, 135-150	168.15				611.2	*	27.01	1027	1.9		8.1	2.1	144		3.64			
19H-2, 135-150	173.15	7.45	3.56								5.4	2.4	150					
19H-5, 135-150	177.50							992			6.1	2.7	152					
20H-2, 135-150	182.65	7.51	3.89						1.6		10.6	3.1	157					0.1
20H-5, 135-150	187.15				578.6	*	26.63	1040			10.2	2.9	152		3.65			
21H-2, 135-150	192.15	7.40	3.51					969	1.3		9.5	1.9	157		3.90			
21H-5, 135-150	196.65							1034	1.2		16.6	2.7	161					
22H-2, 135-150	201.65	7.45	3.76					988	1.2		16.3	3.0	160		3.98			1.8
22H-5, 135-150	206.15				578.8	*	26.91	1056	1.3		6.4	3.2	166					
23H-2, 135-150	211.15	7.49	3.39					995	1.2		17.2	4.6	169		3.58			1.1
23H-5, 135-150	215.65							1041	1.3		11.2	5.4	164					
24H-2, 135-150	220.65	7.46	3.58		574.1	*	26.58	1040	0.9		19.4	6.4	169		3.63			0.6
24H-5, 135-150	225.15							1068	1.3		15.8	7.1	170					
25H-2, 135-150	230.15	7.36	3.38					1055	1.2		15.7	7.4	174					1.4
25H-5, 135-150	234.65							1060	1.1		13.5	7.3	178					
26H-2, 135-150	239.65	7.48	3.51					1024	1.2		18.0	7.1	174		3.63			0.2
26H-5, 135-150	244.15				569.6	*	26.95	1091	1.5		6.4	7.1	178		3.67			
27H-2, 135-150	249.15	7.50	3.39					1045	1.4		8.7	7.4	175					1.3
27H-5, 135-150	253.65							1108	1.6		1.3	7.0	186					
28H-2, 135-150	258.65	7.48	3.06		559.6	*	26.48	1037	1.3		14.5	6.8	173		3.48			0.0
28H-5, 135-150	263.15							1014	1.5		6.0	7.0	175		3.59			
29H-2, 135-150	268.15	7.48	3.43		571.8	*	27.08	954	1.5		4.2	6.1	175					

Table T2 (continued).

Core, section, interval (cm)	Depth (mbsf)	pH	Alk (mM)	SAL	Cl^- (mM)		SO_4^{2-} (mM)	H_4SiO_4 (µM)	HPO_4^{2-} (µM)	NH_4^+ (µM)	Fe (µM)	Mn (µM)	Sr (µM)	ΣH_2S (mM)	DIC (mM)	VFA (µm)		NO_3^- (µM)
																Acetate	Formate	
30H-2, 135-150	277.65				587.8	*	27.26	965	1.7		3.0	2.8	153		3.47			0.9
30H-5, 135-150	282.15							1032	1.5		0.7	3.6	158		3.15			
31H-2, 135-150	287.15				556.0	*	26.30	947	1.6						3.63			0.3
31H-5, 135-150	291.65	7.51	3.14		561.3	*	26.71	1091	1.8		0.1	2.1	152		3.25			

Notes: Alk = alkalinity, SAL = salinity, DIC = dissolved inorganic carbon, VFA = volatile fatty acids. Conc. = concentration. BDL = below detection limit. Standards for IW ICP-AES analyses are routinely made on the *JOIDES Resolution* by mixing known standards with filtered seawater (Murray et al., 2000). For Site 1225, however, standards were prepared differently because the bottle labeled "Site 1215 filtered seawater" contained "freshwater" (as tested by refractometer and taste). Consequently, the standards have a different matrix than the unknowns at Site 1225. Analyses of boron, strontium, and lithium therefore required an "offline" background correction. * = indicated Cl analyses were determined by ion chromatography. Other Cl analyses were determined by titration. This table is also available in **ASCII.**

Table T3. Methane concentrations in headspace, Holes 1225A and 1225C. (**See table notes.** Continued on next page.)

Core, section, interval (cm)	Depth (mbsf)	Methane (ppm in headspace) 20 min @ 60°C	6 hr @ 22°C	24 hr @ 22°C	CH_4 (μM)
201-1225A-					
1H-1, 145–150	1.45		1.82		0.04
1H-1, 145–150*	1.45	1.66			
1H-2, 145–150	2.95		1.89		0.05
2H-2, 145–150	7.25		1.84		0.05
2H-3, 145–150	8.75		1.66		0.01
2H-5, 145–150*	11.75	1.77			
3H-2, 145–150	16.75		1.77		0.03
3H-3, 145–150	18.25		1.77		0.03
3H-5, 145–150*	21.25	1.87			
4H-2, 145–150	26.25		1.74		0.02
4H-3, 145–150	27.75		2.00		0.07
4H-5, 145–150*	30.75	1.99			
5H-2, 145–150	35.75		1.84		0.04
5H-3, 145–150	37.25		1.76		0.03
5H-5, 145–150*	40.25	2.04			
6H-2, 145–150	45.25		1.95		0.07
6H-3, 145–150	46.75		2.84		0.24
6H-5, 145–150*	49.75	2.14			
7H-2, 145–150	54.75		2.14		0.10
7H-4, 0–5	56.30		1.98		0.07
7H-5, 145–150*	59.29	1.97			
8H-2, 145–150	64.25		2.13		0.10
8H-4, 0–5	65.80		2.02		0.08
8H-5, 145–150*	68.75	2.14			
9H-2, 145–150	73.75		2.14		0.10
9H-4, 0–5	75.30		1.82		0.04
9H-5, 145–150*	78.25	2.12			
10H-2, 145–150	83.25		1.96		0.08
10H-4, 0–5	84.80		1.89		0.06
10H-5, 145–150*	87.75	1.97			
11H-2, 145–150	92.75		2.21		0.12
11H-4, 0–5	94.30		2.07		0.09
11H-5, 145–150*	97.25	1.87			
12H-2, 145–150	102.25		1.93		0.06
12H-4, 0–5	103.80		2.09		0.09
12H-5, 145–150*	106.75	1.64			
13H-2, 145–150	111.75		2.11		0.10
13H-4, 0–5	113.30		2.20		0.11
13H-5, 145–150*	116.25	1.71			
14H-2, 145–150	121.25		2.06		0.09
14H-4, 0–5	122.80		2.02		0.09
14H-5, 145–150*	125.75	1.81			
15H-2, 145–150	130.75		1.90		0.06
15H-4, 0–5	132.30		1.90		0.06
15H-5, 145–150*	135.25	2.47			
16H-2, 145–150	140.25		2.34		0.15
16H-4, 0–5	141.80		2.20		0.12
16H-5, 145–150*	144.75	2.23			
17H-1, 145–150	148.25		2.29		0.13
17H-4, 0–5	150.49		2.25		0.12
17H-5, 145–150*	153.44	2.26			
18H-2, 145–150	159.25		2.15		0.12
18H-3, 145–150	160.75		2.26		0.14
18H-5, 145–150*	163.75	2.28			
19H-2, 145–150	168.75		2.28		0.13
19H-4, 0–5	170.30		2.27		0.13
19H-5, 145–150*	173.25	2.21			
20H-2, 145–150	178.25		2.42		0.16
20H-4, 0–5	179.80		2.14		0.10
20H-5, 145–150	182.75	2.07			
21H-2, 145–150	187.65		2.32		0.15
21H-4, 0–5	189.30		2.28		0.14
21H-5, 145–150	192.25	2.10			
22H-2, 145–150	197.25		2.21		0.12
22H-4, 0–5	198.80		2.30		0.15
22H-5, 145–150	201.75	2.01			
23H-2, 145–150	208.25		2.10		0.10
23H-4, 0–5	209.80		2.20		0.12
23H-5, 145–150	212.75	1.98			
24H-2, 145–150	217.75		2.01		0.08
24H-4, 145–150	220.75		2.13		0.11
24H-5, 145–150	222.25	2.00			
25H-2, 145–150	227.25		1.62		0.00
25H-4, 0–5	228.80		2.36		0.14
25H-5, 145–150	231.75	2.09			
26H-2, 145–150	236.75		2.27		0.13
26H-4, 0–5	238.30		1.67		0.01
26H-5, 145–150	241.25	2.04			
27H-2, 145–150	246.25		1.97		0.07
27H-4, 0–5	247.80		2.11		0.09
27H-5, 145–150	250.75	2.10			
30H-2, 145–150	267.04		2.24		0.11
30H-4, 0–5	268.59		1.99		0.07
30H-5, 145–150	270.09	1.95			
31H-2, 145–150	276.65		1.98		0.07
31H-4, 0–5	278.20		1.78		0.04
31H-5, 145–150	281.15	1.97			
32H-2, 0–5	284.57		1.80		0.04
32H-2, 145–150	286.02		1.70		0.02
32H-3, 145–150	287.52		1.63		0.01
32H-5, 145–150	290.52	1.79			
33H-2, 145–150	295.65		1.58		0.00
33H-4, 0–5	297.20		1.76		0.03
33H-5, 145–150	300.15	1.69			
34H-2, 145–150	306.65		1.61		0.00
34H-4, 0–5	308.20		1.57		0.00
34H-5, 145–150	311.15	1.77			
35X-2, 145–150	316.15		1.66		0.01
35X-3, 145–150	317.65	1.60			
201-1225C-					
1H-2, 145–150	2.95			1.70	0.02
1H-5, 145–150	7.45	1.73			
2H-3, 0–5	11.80			1.68	0.01
2H-4, 0–5	13.30			1.78	0.03
2H-5, 130–135	16.10	1.78			
3H-3, 0–5	21.30			1.86	0.05
3H-4, 0–5	22.80			1.87	0.05
3H-5, 130–135	25.60	1.98			
4H-2, 0–5	29.30			1.87	0.05
4H-4, 0–5	32.30			1.97	0.07
4H-5, 130–135	35.10	1.86			
5H-2, 0–5	38.80			1.84	0.04
5H-4, 0–5	41.80			1.99	0.06
5H-5, 130–135	44.60	1.72			
6H-2, 0–5	48.30			2.24	0.12
6H-4, 0–5	51.30			2.04	0.07
6H-5, 130–135	54.10	1.95			
7H-2, 0–5	57.80			2.05	0.08
7H-4, 0–5	60.80			2.26	0.12
7H-5, 130–135	63.60	1.84			
8H-2, 0–5	67.30			2.00	0.08
8H-4, 0–5	70.30			2.13	0.10
8H-5, 130–135	73.10	1.95			
9H-2, 0–5	76.80			2.14	0.10
9H-4, 0–5	79.80			2.18	0.11
9H-5, 130–135	82.60	1.92			
10H-2, 0–5	86.30			2.20	0.12
10H-4, 0–5	89.30			2.10	0.10
10H-5, 130–135	92.10	1.66			
11H-2, 0–5	95.80			2.44	0.15
11H-3, 0–5	97.30			2.37	0.14
11H-5, 130–135	101.60	1.88			

Table T3 (continued).

Core, section, interval (cm)	Depth (mbsf)	Methane (ppm in headspace) 20 min @ 60°C	6 hr @ 22°C	24 hr @ 22°C	CH_4 (µM)
12H-2, 0–5	105.30			2.35	0.15
12H-4, 0–5	108.30			2.26	0.11
12H-5, 130–135	111.10	2.16			
13H-2, 0–5	114.80			2.25	0.12
13H-3, 145–150	117.75			2.35	0.15
13H-5, 130–135	120.60	1.96			
14H-2, 0–5	124.30			2.13	0.11
14H-4, 0–5	127.30			2.40	0.16
14H-5, 130–135	130.10	2.09			
15H-2, 0–5	133.80			2.28	0.12
15H-4, 0–5	136.80			2.19	0.11
15H-5, 130–135	139.60	2.00			
16H-2, 0–5	143.30			2.34	0.14
16H-4, 0–5	146.30			2.33	0.13
16H-5, 130–135	149.10	2.29			
17H-4, 0–5	155.04			2.51	0.18
17H-5, 130–135	157.84	1.99			
18H-4, 0–5	165.30			2.54	0.19
18H-5, 130–135	168.10	2.09			
19H-2, 0–5	171.80			2.68	0.22
19H-5, 130–135	177.45	2.11			
20H-2, 0–5	181.30			2.43	0.16
20H-5, 130–135	187.10	2.22			
21H-4, 0–5	193.80			2.29	0.15
22H-4, 0–5	203.30			2.20	0.14
23H-4, 0–5	212.80			2.56	0.19
24H-4, 0–5	222.30			2.85	0.24
25H-4, 0–5	231.80			2.63	0.19
26H-4, 0–5	241.30			2.37	0.16
27H-4, 0–5	250.80			2.48	0.16
28H-5, 0–5	261.80			2.19	0.12
29H-3, 0–5	268.30			2.05	0.08
30H-4, 0–5	279.30			2.09	0.11
31H-5, 0–5	290.30			1.86	0.06

Notes: * = samples with variable sediment volumes (not determined) from ~3 to 6 mL. This table is also available in **ASCII.**

Table T4. Calculated interstitial water hydrogen in incubated samples, Site 1225.

Core, section, interval (cm)	Depth (mbsf)	H_2 (nM)	Incubation temperature (°C)
2H-3, 15–21	7.45	1.02	4
4H-3, 15–21	26.45	1.64	4
6H-3, 15–21	45.45	4.69	4
8H-3, 15–21	64.45	2.06	4
10H-3, 15–21	83.45	2.39	4
12H-3, 15–21	102.45	3.09	4
14H-3, 15–21	121.45	3.17	4
16H-3, 12–21	140.45	1.26	4
18H-3, 12–21	159.45	1.29	4
20H-3, 12–21	178.45	1.52	4
22H-3, 12–21	197.45	1.90	4
24H-3, 12–21	217.95	2.19	4
26H-3, 60–66	237.40	1.70	4
30H-2, 60–66	266.19	1.89	4
32H-3, 60–66	286.67	1.14	4
35X-5, 70–76	319.90	1.35	4

Note: This table is also available in **ASCII.**

Table T5. Calcium carbonate and organic carbon concentrations, Holes 1225A and 1225C.

Core, section	Depth (mbsf)	$CaCO_3$ (%)	C_{org}
201-1225A-			
2H-3, 15–21	7.15	78.0	0.00
4H-3, 15–21	26.15	81.0	0.15
6H-3, 15–21	42.15	83.0	0.00
8H-3, 15–21	61.15	70.0	0.07
10H-3, 15–21	83.15	82.0	0.14
12H-3, 15–21	102.15	72.0	0.23
14H-3, 15–21	121.21	75.0	0.13
16H-3, 15–21	143.15	75.0	0.14
18H-3, 15–21	159.15	81.0	0.00
20H-3, 15–21	178.15	57.0	0.11
22H-3, 15–21	197.00	77.0	0.19
24H-3, 15–21	217.15	61.0	0.23
26H-3, 60–66	237.60	64.0	0.14
30H-2, 60–66	266.60	42.0	0.42
32H-3, 60–66	286.60	84.0	0.53
34H-3, 60–66	306.60	70.0	0.01
35X-3, 70–76	319.60	76.0	0.00
201-1225C-			
1H-1, 67–67	0.61	85.1	0.39
1H-3, 80–86	3.80	79.0	0.18
1H-6, 75–81	8.50	76.9	0.00
2H-4, 50–51	13.80	73.0	0.00
3H-4, 50–51	23.30	84.1	0.00
4H-3, 50–51	31.30	68.2	0.00
5H-3, 50–51	40.80	77.1	0.25
6H-3, 50–51	50.30	81.5	0.06
7H-3, 50–51	59.80	64.8	0.00
8H-3, 50–51	69.30	82.5	0.07
9H-3, 50–51	78.80	70.9	0.05
10H-3, 50–51	88.30	76.6	0.02
11H-3, 50–51	97.80	74.4	0.07
12H-3, 50–51	107.30	82.6	0.14
13H-3, 50–51	116.80	78.7	0.12
14H-3, 50–51	126.30	81.7	0.00
15H-3, 50–51	135.80	80.1	0.00
16H-3, 50–51	145.30	70.3	0.17
17H-4, 53–54	155.57	71.8	0.00
18H-3, 50–51	164.30	73.5	0.07
19H-3, 50–51	173.80	69.5	0.85
20H-3, 50–51	183.30	67.3	0.02
21H-3, 50–51	192.80	75.5	0.06
22H-3, 50–51	202.30	80.7	0.00
23H-3, 50–51	211.80	70.5	0.13
24H-3, 50–51	221.30	72.0	0.16
25H-3, 50–51	230.30	61.6	0.23
26H-3, 50–51	240.30	76.8	0.07
27H-3, 50–51	249.80	57.5	0.01
28H-3, 50–51	259.30	78.0	0.20
29H-3, 50–51	268.80	25.8	0.27
30H-3, 50–51	278.30	64.5	0.33
31H-3, 50–51	287.80	76.7	0.19
33H-3, 10–11	298.89	79.6	0.15

Note: This table is also available in **ASCII.**

Table T6. Potential contamination of slurries obtained using fluorescent microspheres (0.5 µm diameter) as prokaryotic cell mimics, deployed at amounts of 4×10^{12} microspheres per core, Holes 1225A and 1225C.

Core, section, interval (cm)	Sample type	Microspheres/ 50 fov	Microspheres/ mL of sediment	Mean	Potential contamination (nL/mL of sediment)	Delivery confirmed
201-1225A-						
2H-3, 33–45	Slurry	48	8,555			
	Vial	37	42,456	25,505	0.128	Yes
12H-3, 33–45	Slurry	12	2,139			
	Vial	6	5,503	3,821	0.019	Yes
22H-3, 33–45	Slurry	0	0			
	Vial	0	0	0	0	Yes
34H-3, 78–90	Slurry	0	0			
	Vial	0	0	0	0	No
201-1225C-						
1H-1, 44–61	Slurry	0	0			
	Vial	0	0	0	0	Yes

Notes: Vial = secondary check using vial samples collected for total bacterial counts. fov = a field of view under the microscope approximating an area of 9000 μm^2.

Table T7. Media inoculated with sample material from different depths, Holes 1225A and 1225C.

Core:	1225A-2H	1225A-6H	1225A-22H	1225A-22H	1225A-34H	1225C-1H
Depth (mbsf):	8	46	103	198	307	1
Medium:						
Sed	12°C: MPN		12°C: MPN	12°C: MPN, RT: EN	12°C: MPN, RT: EN	12°C: MPN, RT: EN
Mono	12°C: MPN		12°C: MPN	12°C: MPN, RT: EN	12°C: MPN, RT: EN	12°C: MPN, RT: EN
Poly	12°C: MPN		12°C: MPN	12°C: MPN	12°C: MPN, RT: EN	12°C: MPN, RT: EN
Aro	12°C: MPN		12°C: MPN	12°C: MPN, RT: EN	12°C: MPN, RT: EN	12°C: MPN, RT: EN
B-sed	12°C: MPN		12°C: MPN	12°C: MPN	12°C: MPN, RT: EN	12°C: MPN
B-poly	12°C: MPN		12°C: MPN	12°C: MPN	12°C: MPN, RT: EN	12°C: MPN
Rad	12°C: MPN		12°C: MPN	12°C: MPN	12°C: MPN, RT: EN	12°C: MPN
Grad	12°C: EN		12°C: EN	12°C: EN	12°C: EN	12°C: EN
FERM-Glyc: 8.0	60°C: MPN	60°C: EN	60°C: EN	60°C: MPN	60°C: MPN	60°C: MPN
FERM-Glyc: 8.8	60°C: EN	60°C: EN	60°C: EN	60°C: EN	60°C: EN	60°C: EN
FERM-Xyl: 8.0	60°C: MPN	60°C: EN	60°C: EN	60°C: MPN	60°C: MPN	60°C: MPN
FERM-Xyl: 8.8	60°C: EN	60°C: EN	60°C: EN	60°C: EN	60°C: EN	60°C: EN
SRB: 8.0	60°C: MPN	60°C: EN	60°C: EN	60°C: MPN	60°C: MPN	60°C: MPN
SRB: 8.6	60°C: EN	60°C: EN	60°C: EN	60°C: EN	60°C: EN	60°C: EN
SRB benz: 8.0	60°C: EN	60°C: EN	60°C: EN	60°C: EN	60°C: EN	60°C: EN
H_2/HCO_3^-/FeIII: 7.9	60°C: MPN	60°C: EN	60°C: EN	60°C: MPN	60°C: MPN	60°C: MPN
H_2/HCO_3^-/FeIII: 8.5	60°C: EN	60°C: EN	60°C: EN	60°C: EN	60°C: EN	60°C: EN
H_2/HCO_3^-/MnIV: 7.8	60°C: EN			60°C: EN	60°C: EN	60°C: EN
H_2/HCO_3^-: 7.8	60°C: MPN	60°C: EN	60°C: EN	60°C: MPN	60°C: MPN	60°C: MPN
H_2/HCO_3^-: 8.8	60°C: EN	60°C: EN	60°C: EN	60°C: EN	60°C: EN	60°C: EN
C-18-lipo: 7.8	60°C: MPN	60°C: EN	60°C: EN	60°C: MPN	60°C: MPN	60°C: MPN
C-18-lipo: 9.0	60°C: EN	60°C: EN	60°C: EN	60°C: EN	60°C: EN	60°C: EN
Chlor: 7.8	60°C: EN			60°C: EN	60°C: EN	60°C: EN
201-1*					RT: 50°C, 80°C: EN	
201-2					RT: 50°C, 80°C: EN	
201-3*					RT: 50°C, 80°C: EN	
201-4					RT: 50°C, 80°C: EN	
201-5					RT: 50°C, 80°C: EN	
201-6					RT: 50°C, 80°C: EN	
201-7					RT: 50°C, 80°C: EN	
201-8*					RT: 50°C, 80°C: EN	
201-9					RT: 50°C, 80°C: EN	
201-10					RT: 50°C, 80°C: EN	
201-11*					RT: 50°C, 80°C: EN	
Fe(III)red†					10°C: MPN	10°C: MPN
Mn(IV)red†					10°C: MPN	10°C: MPN
AmOx					10°C: MPN	10°C: EN
NiOx					10°C: MPN	10°C: EN
Methylo					10°C: EN	

Notes: MPN = most probable number, EN = enrichment. * = these media were also inoculated from the slurry prepared from Core 201-1225A-35H-CC (320 mbsf). Incubation was done as given for 307 mbsf. † = Eight additional samples were taken on the catwalk for 10°C: MPN assays from Hole 1225C from the following depths: 5, 10, 25, 50, 100, 150, 200, and 250 mbsf. Enrichment assays were qualitative (EN) or quantitative (MPN) and incubated at the temperature given and/or at room temperature (RT). Media are defined in Table **T9,** p. 90, in the "Explanatory Notes" chapter (see also **"Microbiology,"** p. 14, and Tables **T4,** p. 84, **T5,** p. 85, and **T7,** p. 88, all in the "Explanatory Notes" chapter).

Table T8. Downhole temperature measurement summary, Hole 1225A.

Depth (mbsf)	Tool	Measurement location	Thermal conductivity (W/[m·K])	Temperature (°C)
0.0	Adara	B Core 1225A-1H	0.88	1.34
61.3	Adara	B Core 1225A-7H	0.81	2.78
80.3	Adara	B Core 1225A-9H	0.92	3.26
127.8	Adara	B Core 1225A-14H	0.98	3.89
203.8	DVTP	B Core 1225A-22H	0.98	5.30
303.7	DVTP	T Core 1225A-34H	1.10	6.18
320.0	—	—	0.89*	6.97†

Notes: B = bottom of core, T = top of core. DVTP = Davis-Villinger Temperature Probe. — = not applicable. * = average thermal conductivity. † = projected temperature at base of hole. The last line shows the temperature extrapolated to basement using the linear fit in Figure **F31,** p. 70, and the mean thermal conductivity computed from data plotted in Figure **F29A,** p. 68.

Table T9. Detail of logging operations, Hole 1225A.

Date (Feb 2002)	UTC (GMT – 7 hr)	Tool depth (mbsf)	Remarks
10	1930		Last core on deck
10	1930–2030		Hole swept with 20 bbl of sepiolite mud
10	2030–2200		Wiper trip up to 80 mbsf, back down to 291 mbsf
10	2200–2300		Hole displaced with 130 bbl of sepiolite mud
10	2300–2400		Set back top drive; bottom of pipe put at 80 mbsf
11	0030		Start logging rig-up
11	0300		Start going downward with triple combination tool string: TAP/DIT-E/ HLDT/APS/HNGS/SGT
11	0442	0	Stop 5 min at mudline for temperature calibration
11	0454	80	Tool string in open hole
11	0510	323	Tool at TD; start logging upward at 900 ft/hr
11	0604	80	Tool back into pipe; speed up to 1500 ft/hr to log mudline
11	0617	–22	End of pass 1; standing 5 min and start going back downward
11	0641	323	Tool at TD; start logging upward pass 2 at 900 ft/hr
11	0715	175	End of pass 2; speed up tool to 6000 ft/hr
11	0925	0	Tool back on rig floor
11	1045		Finish rig-down

Notes: UTC = Universal Time Coordinated. TD = total depth. TAP = LDEO Temperature/Acceleration/Pressure tool, DIT-E = Dual Induction Tool, HLDT = Hostile Environment Litho-Density Tool, APS = Accelerator Porosity Sonde, HNGS = Hostile Environment Gamma Ray Sonde, SGT = Scintillation Gamma Ray Tool.